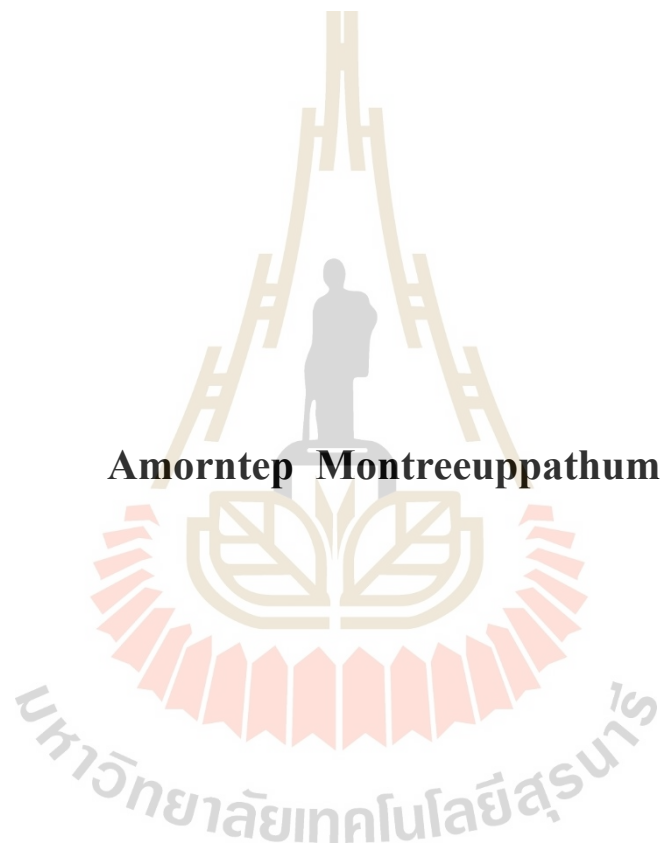


**STRUCTURE AND ELECTROCHEMICAL  
PROPERTIES OF MANGANESE LITHIUM BORATE  
GLASS**



**A Thesis Submitted in Partial Fulfillment of the Requirements for the  
Degree of Master of Science in Physics  
Suranaree University of Technology  
Academic Year 2020**

# โครงสร้างและสมบัติไฟฟ้าเคมีของแก้วแมงกานีสลิเทียมบอเรต



วิทยานิพนธ์นี้เป็นส่วนหนึ่งของการศึกษาตามหลักสูตรปริญญาวิทยาศาสตรมหาบัณฑิต  
สาขาวิชาฟิสิกส์  
มหาวิทยาลัยเทคโนโลยีสุรนารี  
ปีการศึกษา 2563

**STRUCTURE AND ELECTROCHEMICAL PROPERTIES OF  
MANGANESE LITHIUM BORATE GLASS**

Suranaree University of Technology has approved this thesis submitted in partial fulfillment of the requirements for a Master's Degree.

Thesis Examining Committee

*Rattikorn Yimnirun*

(Prof. Dr. Rattikorn Yimnirun)

Chairperson

*Prayoon Songsiriritthigul*

(Assoc. Prof. Dr. Prayoon Songsiriritthigul)

Member (Thesis Advisor)

*Saroj Rujirawat*

(Assoc. Prof. Dr. Saroj Rujirawat)

Member

*Pinit K.*

(Dr. Pinit Kidkhunthod)

Member

*Chatchai Jothityangkoon*

(Assoc. Prof. Dr. Chatchai Jothityangkoon)

Vice Rector for Academic Affairs  
and Quality Assurance

*Santi Maensiri*

(Prof. Dr. Santi Maensiri)

Dean of Institute of Science

อมรเทพ มนตรีอุปถัมภ์ : โครงสร้างและสมบัติไฟฟ้าเคมีของแก้วแมงกานีสลิเทียมบอเรต  
(STRUCTURE AND ELECTROCHEMICAL PROPERTIES OF MANGANESE  
LITHIUM BORATE GLASS). อาจารย์ที่ปรึกษา : รองศาสตราจารย์ ดร.ประยูร  
สงสิริฤทธิกุล, 96 หน้า.

แก้วแมงกานีสลิเทียมบอเรต/ แบตเตอรี่ชนิดลิเทียมไอออน

วิทยานิพนธ์ฉบับนี้เป็นรายงานการศึกษาการแก้วแมงกานีสลิเทียมบอเรตที่ถูกสังเคราะห์ด้วยเทคนิคการลดอุณหภูมิลงอย่างฉับพลัน การตรวจสอบโครงสร้างและองค์ประกอบเฟสของแก้วในระบบ  $0.2\text{MnO}_2-0.8(\text{Li}_2\text{O}-x\text{B}_2\text{O}_3)$  โดยที่  $x$  เท่ากับ 1, 2, 3 และ 4 โมล อาศัยเทคนิค การดูดกลืนรังสีเอกซ์ (X-ray absorption spectroscopy หรือ XAS) และการเลี้ยวเบนของรังสีเอกซ์ (X-ray diffraction หรือ XRD) พบว่ารูปแบบการเลี้ยวเบนของรังสีเอกซ์ของแก้วทุกตัวอย่างมีลักษณะฐานกว้าง ซึ่งเป็นลักษณะของโครงสร้างแบบอสัณฐานของแก้ว จากสเปกตรัมการดูดกลืนรังสีเอกซ์บ่งบอกถึงสถานะการเกิดออกซิเดชันแบบผสมของ  $\text{Mn}^{2+}$  และ  $\text{Mn}^{3+}$  ซึ่งสอดคล้องกับผลลัพธ์ที่ได้จากการศึกษาเลขออกซิเดชันด้วยเทคนิคการดูดกลืนรังสีอัลตราไวโอเล็ต (UV-Visible spectroscopy หรือ UV-Vis) และจากการตรวจสอบสมบัติโดยอาศัยเทคนิค Extended X-ray absorption fine structure หรือ EXAFS พบว่า ระยะเฉลี่ยของพันธะอะตอมแมงกานีสกับออกซิเจนมีค่าระหว่าง 2.03 - 2.07 Å นอกจากนี้ยังอาศัยเทคนิคอิเล็กตรอนแบบส่องกราด (Scanning electron microscopy หรือ SEM) และเทคนิคการวัดการกระจายพลังงานของรังสีเอกซ์ (Energy dispersive X-ray spectroscopy หรือ EDS) เพื่อทำการตรวจสอบองค์ประกอบของธาตุที่มีอยู่ในตัวอย่างแก้ว ยิ่งไปกว่านั้นผู้วิจัยได้ทำการศึกษาสมบัติทางแม่เหล็ก และสมบัติทางไฟฟ้าเคมีของแก้ว โดยพบว่าแก้วทุกตัวอย่างแสดงพฤติกรรมทางแม่เหล็กแบบพาราแมกเนติก และมีค่าการเก็บประจุไฟฟ้าเคมีสูงสุด เท่ากับ 196 ฟารัดต่อกรัม จึงถือได้ว่าแก้วตัวอย่างที่เตรียมนี้มีแนวโน้มที่จะสามารถนำไปใช้เป็นขั้วอิเล็กโทดของแบตเตอรี่ชนิดลิเทียมไอออนในอนาคตได้

สาขาวิชาฟิสิกส์  
ปีการศึกษา 2563

ลายมือชื่อนักศึกษา อมรเทพ มนตรีอุปถัมภ์  
ลายมือชื่ออาจารย์ที่ปรึกษา ประยูร สงสิริฤทธิกุล

AMORNTEP MONTREEUPPATHUM : STRUCTURE AND  
ELECTROCHEMICAL PROPERTIES OF MANGANESE LITHIUM  
BORATE GLASS. THESIS ADVISOR : ASSOC.PROF. PRAYOON  
SONGSIRIRITTHIGUL, Ph.D. 96 PP.

MANGANESE LITHIUM BORATE GLASS/ LITHIUM ION BATTERY

This thesis presents the study on the synthesis and characterization on manganese lithium borate glass by melt-quenched technique. The structure and phase component of the glass,  $0.2\text{MnO}_2\text{-}0.8(\text{Li}_2\text{O-xB}_2\text{O}_3)$  with  $x = 1, 2, 3$  and  $4$  moles were characterized by X-ray absorption spectroscopy (XAS) and X-ray diffraction (XRD). The pattern of X-ray diffraction of prepared glass exhibits a large peak with no appear sharp peak which is the nature of amorphous phase. The oxidation state of manganese content in each sample that obtained by XAS which present the mixing of  $\text{Mn}^{2+}$  and  $\text{Mn}^{3+}$  corresponding to the Mn oxidation state results measured by UV-visible spectroscopy technique (UV-VIS). The Extended x-ray absorption fine structure (EXAFS) was used to observation the bonding distance of Mn-O, the average bonding distance are between  $2.03\text{-}2.07 \text{ \AA}$ . Moreover, scanning electron microscopy (SEM) and energy dispersive x-ray spectroscopy (EDS) depict the subsistence of element in each sample. The electrochemical and magnetization properties of samples have been also considered, the highest specific capacitance have been observed at  $196 \text{ F.g}^{-1}$ .

School of Physics

Academic Year 2020

Student's Signature



Advisor's Signature



## **ACKNOWLEDGEMENTS**

First of all, I would like to express the deepest appreciation to my advisor Assoc. Prof. Dr. Prayoon Songsiriritthigul for his patience, motivation, inspiration, advice, experience supervision, and guidance since the early stage of this research as well as giving me outstanding throughout the work.

I would like to thank Prof. Dr. Rattikorn Yimnirun and Assoc. Prof. Dr. Saroj Rujirawat for his valuable advice throughout this work, Dr. Pinit Kidkhunthod for his advice on XAS analysis and opportunities to gain experiences at Beamline 5.2: SUT-NANOTEC-SLRI XAS beamline. I also would like to thank all the members of group.

I would like to acknowledge the Synchrotron Light Research Institute (SLRI) (public organization), Thailand for the scholarship and this work has been partially supported by the Research Network NANOTEC program of the National Nanotechnology Center, NSTDA, Ministry of Higher Education, Science, Research and Innovation, Thailand.

Finally, I would like to express appreciation to my family for their great support and encouragement to me throughout my studies.

Amorntep Montreeuppathum

# CONTENTS

	<b>Page</b>
ABSTRACT IN THAI.....	I
ABSTRACT IN ENGLISH .....	II
ACKNOWLEDGEMENTS.....	III
CONTENTS.....	IV
LIST OF TABLES .....	VI
LIST OF FIGURES .....	VII
LIST OF BBREVIATIONS.....	XI
<b>CHAPTER</b>	
<b>I INTRODUCTION.....</b>	<b>1</b>
<b>II THEORY/ LITERATURE REVIEWS.....</b>	<b>4</b>
2.1 Definition of glass.....	4
2.2 Borate-based glass .....	7
2.3 Lithium borate glasses electrode materials.....	8
2.3.1 Electrochemical property .....	8
2.3.2 Structural property .....	13
<b>III MATERIALS AND METHODS.....</b>	<b>19</b>
3.1 Glass preparation .....	19
3.2 Characterization techniques.....	21
3.2.1 X-ray diffraction spectroscopy .....	21

## CONTENT (Continued)

	<b>Page</b>
3.2.2 X-ray absorption spectroscopy .....	23
3.2.3 Vibration sample magnetometer .....	33
3.2.4 UV-Visible spectrometer .....	35
3.2.5 Scanning electron microscopy .....	37
3.2.6 Energy dispersive X-ray spectroscopy.....	39
3.2.7 Electrochemical measurement .....	40
<b>IV RESULTS AND DISCUSSION</b> .....	<b>42</b>
4.1 Glass preparation .....	42
4.2 X-ray diffraction result .....	45
4.3 Scanning electron microscopy result .....	45
4.4 X-ray absorption spectroscopy result .....	49
4.5 UV-Vis spectrophotometer result .....	53
4.6 Vibration sample magnetometer result .....	57
4.7 Cyclic voltammetry result.....	58
<b>V CONCLUSION</b> .....	<b>62</b>
REFERENCES .....	64
APPENDIX.....	70
CURRICULUM VITAE.....	96

## LIST OF TABLE

Table	Page
2.1 Computed properties of the $\text{LiMnBO}_3$ polymorphs. ....	13
3.1 The technical information of SUT-NANOTEC-SLRI beamline.....	30
4.1 The percentage content of the glasses sample with difference composition.....	49
4.2 EXAFS fitting parameter of $0.2\text{MnO}_2-0.8(1\text{Li}_2\text{O}-x\text{B}_2\text{O}_3)$ where $x = 1, 2, 3$ and $4$ (mol%) glass samples. ....	50

## LIST OF FIGURES

<b>Figure</b>	<b>Page</b>
2.1 Different objective of use of glass (middle column) and their correspond product (right column). (Adapted from Karmakar et al., 2017). ....	4
2.2 The relationships of different types of glasses. (Adapted from Karmakar et al., 2017) .....	5
2.3 Atomic structural representation of (a) $A_2O_3$ crystal (b) $A_2O_3$ glass. (Varshneya et al., 1994).....	6
2.4 The first ten charge/discharge curves of the $V_2O_5$ - $LiBO_2$ glass within a potential window of 1.5-4.0 V at 50 mA/g rate. (Afyon et al., 2014).....	9
2.5 The rate capability of the $V_2O_5$ - $LiBO_2$ glass within 1.5-4.0 V at 50, 100, 200 and 400 mA/g rates (at room temperature). (Afyon et al., 2014) .....	10
2.6 Electrochemical measurements for $LiMnBO_3$ (II) cathode material. a Charge - discharge studies. b Cycle life. Insert figure AC impedance spectra of $LiMnBO_3$ (II). (Ragupathi et al., 2017).....	10
2.7 Cyclic voltammograms of (a) $0.2MnO_2-0.8(Li_2O-2B_2O_3)$ , (b) $0.25MnO_2-0.75(Li_2O-2B_2O_3)$ , (c) $0.3MnO_2-0.7(Li_2O-2B_2O_3)$ glass electrodes s at different scan rates. (Khajornrit et al., 2018). ....	11
2.8 Room temperature magnetization hysteresis loop of $0.5V_2O_5-0.5(Li_2O-xB_2O_3)$ glass samples: (a) $x=1$ , (b) $x=2$ , (c) $x=3$ . (Laorodphan et al., 2018) .....	12

## LIST OF FIGURES (Continued)

<b>Figure</b>	<b>Page</b>
2.9 Schematic diagrams of the (a) hexagonal and (b) monoclinic LiMnBO <sub>3</sub> structure.....	13
2.10 Schematic Crystal structures of LiMnBO <sub>3</sub> : a) skew [001] view of the hexagonal phase, b) skew [100] view of the monoclinic phase. ....	14
2.11 View of the crystal structure of Li <sub>7</sub> Mn(BO <sub>3</sub> ) <sub>3</sub> along [001] corresponding to the direction of columns of linked MnO <sub>4</sub> tetrahedra pairs (pink) interconnected by BO <sub>3</sub> <sup>3+</sup> ions (B green, O red, Li black). (Afyon et al., 2014). ....	15
2.12 Columns of pairs of MnO <sub>4</sub> tetrahedra (pink) interconnected by BO <sub>3</sub> <sup>3+</sup> ions extending along the crystallographic c-axis showing one translational unit (B green, O red). (Afyon et al., 2014). ....	16
2.13 XPS profiles of glass samples: (a) 0.2MnO <sub>2</sub> -0.8(Li <sub>2</sub> O-2B <sub>2</sub> O <sub>3</sub> ), (b) 0.25MnO <sub>2</sub> -0.75(Li <sub>2</sub> O-2B <sub>2</sub> O <sub>3</sub> ), (c) 0.3MnO <sub>2</sub> -0.7(Li <sub>2</sub> O-2B <sub>2</sub> O <sub>3</sub> ). (Khajornrit et al., 2018). ....	17
2.14 XPS spectra of LiMnBO <sub>3</sub> (III) materials. (a) Li 1s, (b) O 1s, (c) B 1s, and (d) Mn 2p. (Andersson M et al., 2002). ....	18
3.1 Show the raw materials lithium carbonate (Li <sub>2</sub> CO <sub>3</sub> ) and boric acid (H <sub>3</sub> BO <sub>3</sub> ) ...	20
3.2 Show the raw materials manganese dioxide (MnO <sub>2</sub> ). ....	21
3.3 Schematic diagrams of typical x-ray diffraction.. ....	22

## LIST OF FIGURES (Continued)

<b>Figure</b>	<b>Page</b>
3.4 The Rigaku-smartlab X-ray diffractometer.....	23
3.5 Schematic of incident and transmitted X-ray beam..	24
3.6 The energy absorption edge depends on the electron energy level ..	25
3.7 Theoretical and algorithm for XANES and EXAFS spectra.....	26
3.8 The XANES spectrum of manganese <i>k</i> -edge.....	27
3.9 The EXAFS fitting result (a) fourier transform, (b) k-space.....	28
3.10 Shown setup of beamline 5.2 SUT-NANOTEC-SLRI, Thailand .....	29
3.11 Synchrotron experimental hall at the Light Research Institute .....	32
3.12 Schematic diagrams of vibration sample magnetometer.....	34
3.13 Schematic diagrams of typical uv-visible spectrometer.....	36
3.14 Schematic diagrams of typical scanning electron microscopy.....	39
3.15 Schematic representation of the types of X-ray spectrum emitted upon bombardment of fast electron.....	40
3.16 Show Metrohm autolab equipment at beamline 2, SLRI .....	41
4.1 The prepared lithium borate glass by melt-quench technique.....	43
4.2 The quenching process on glasses preparation .....	43
4.3 The prepared manganese lithium borate glass by melt-quench technique.....	44
4.4 X-ray diffraction of $0.2\text{MnO}_2\text{-}0.8(1\text{Li}_2\text{O-xB}_2\text{O}_3)$ where $x = 1, 2, 3$ and 4 (mol%) glass samples.....	45
4.5 EDS mapping of $0.2\text{MnO}_2\text{-}0.8(1\text{Li}_2\text{O-}1\text{B}_2\text{O}_3)$ samples. ....	46

## LIST OF FIGURES (Continued)

Figure	Page
4.6 SEM image of $0.2\text{MnO}_2\text{-}0.8(1\text{Li}_2\text{O-}1\text{B}_2\text{O}_3)$ samples, (a) samples, (b) boron distribution, (c) manganese distribution and (d) oxygen distribution. ....	48
4.7 XANES spectra of Mn <i>k</i> -edge of $0.2\text{MnO}_2\text{-}0.8(1\text{Li}_2\text{O-}x\text{B}_2\text{O}_3)$ where $x = 1, 2, 3, 4$ (mol%) glass samples and standard samples. ....	50
4.8 Fourier transform plot at Mn <i>k</i> -edge from experiment (dot line) and fitting (solid line) of $0.2\text{MnO}_2\text{-}0.8(1\text{Li}_2\text{O-}x\text{B}_2\text{O}_3)$ where $x = 1, 2, 3,$ and $4$ (mol%) glass samples . ....	52
4.9 Optical absorbance spectra of $0.2\text{MnO}_2\text{-}0.8(1\text{Li}_2\text{O-}x\text{B}_2\text{O}_3)$ glasses samples: where $x = 1, 2, 3$ and $4$ (mol%). ....	54
4.10 Plot of $(\alpha h\nu)^{1/2}$ as function of photon energy ( $h\nu$ ) of $0.2\text{MnO}_2\text{-}0.8(1\text{Li}_2\text{O-}x\text{B}_2\text{O}_3)$ glass samples: where (a) $x = 1,$ (b) $x = 2,$ (c) $x = 3,$ and (d) $x = 4$ (mol%). ....	56
4.11 Magnetization hysteresis loop of $0.2\text{MnO}_2\text{-}0.8(1\text{Li}_2\text{O-}x\text{B}_2\text{O}_3)$ where $x = 1, 2, 3, 4$ (mol%) samples measured at room temperature. ....	58
4.12 Cycle voltammograms of (a) $0.2\text{MnO}_2\text{-}0.8(1\text{Li}_2\text{O-}1\text{B}_2\text{O}_3),$ (b) $0.2\text{MnO}_2\text{-}0.8(1\text{Li}_2\text{O-}2\text{B}_2\text{O}_3),$ (c) $0.2\text{MnO}_2\text{-}0.8(1\text{Li}_2\text{O-}3\text{B}_2\text{O}_3)$ and (d) $0.2\text{MnO}_2\text{-}0.8(1\text{Li}_2\text{O-}4\text{B}_2\text{O}_3)$ glasses electrode at different scan rate (d) plot of specific capacitance versus scan rate. ....	62

## LIST OF ABBREVIATIONS

Å	Angstrom
°C	Degree Celsius
eV	Electron volte
hr	hour
F	Farad
g	gram
XPS	X-ray photoelectron Spectroscopy
XAS	X-ray absorption spectroscopy
XRD	X-ray diffraction spectroscopy
SEM	Scanning electron microscopy
EDS	Energy dispersive spectroscopy
UV-Vis	UV-Visible spectrometer
CV	Cyclic voltammetry
VSM	Vibration sample magnetometer
SLRI	Synchrotron Light Research Institute

# CHAPTER I

## INTRODUCTION

Glasses and glass-ceramics are considered as advanced functional materials exhibiting interesting properties suitable for many applications (Karmakar et al., 2017). Because of their applications in many areas such as solid-state batteries, optical detectors, optical fibers, and other fields, glasses and glass-ceramics have attracted great attention and gained popularity in recent years. Glasses and crystalline materials exhibit totally different arrangements of their atoms. In some applications, glasses have a number of advantages over crystal products. More importantly, glasses could be fabricated in any size and shape. It is well known that borate glasses are the important fundamental glass formers because they exhibit relative high field strength, small cation size, low heat of fusion and trivalent nature of boron. Among borate glasses, lithium borate glasses have gained significant attention of many researchers because they exhibit rather good stability at high voltage in addition to their isotropic ion conductivity. Thus, lithium borate glasses are considered as potential materials for fabricating thin film electrolytes of electrical storage devices, i.e. batteries and capacitors (Ramteke et al., 2014; Pye et al., 1978; Berkemeier et al., 2007; Rao et al., 1996).

The development of supercapacitor and battery electrodes is crucial for the advances in energy storage technology. Electrode material plays an crucial role in

improving the performance of supercapacitors. In addition, electrolyte and many other factors influence the precise capacitance of any supercapacitor material. Many different types of electrode materials have been explored. It has been demonstrated that carbon-based materials exhibit a higher capacitance than pseudo capacitor metal oxide-based materials when it comes to electrode potential materials (Lokhande et al., 2011; Zhao et al., 2013). Manganese oxide compound materials such as  $Mn_2O_4$ ,  $MnO_2$  and  $MnO$  were chosen as supercapacitor electrode materials because they are environmentally friendly, cheap, have a variety of oxidation states. Moreover, by using these materials a high level of specific capacitance for 1400 F/g and  $1370 F.g^{-1}$  could be obtained (Qi et al., 2016; Toupin et al., 2004). Li and Mn elements have piqued interest as potential cathode materials for rechargeable Li-ion batteries, owing to their high energy density of  $1000 Wh.kg^{-1}$  and a low price when compared to  $LiCoO_2$  (Ozo-emenana et al., 2016; Yu et al., 2013). Lithium-borate glasses composite materials have recently attracted a lot of interest in the field of energy storage (Afyon et al., 2014). It is known that high-capacity metal oxide electrode materials with crystalline structure are possible. On the other hand, crystalline electrode materials have some limitations, including electrode swelling and ion penetration through the crystalline lattice. To get avoid such limitations, great efforts have been spent for trying to replace crystalline electrode materials with amorphous glasses. With glasses, huge possibilities to alter material properties, primarily, by modifying bonding angles. For example, changes in the angle linking network-forming polyhedral bonding, such as the Si-O-Si bond angle (which may vary from  $125^\circ$  to  $165^\circ$ ) and the P-O-P bond angle (which can range from  $123^\circ$  to  $180^\circ$ ) in phosphate glass, are connected to the flexibility of the glass structure. The bond angle in the boroxol ring in the borate structure will drastically alter in the case of borate

glass. Both of these materials have an exceptional ability to shape glass (Stoch, 1999). It was shown that the vanadium lithium borate-base glasses ( $V_2O_5$ -LiBO<sub>2</sub>) exhibit a high specific capacity of roughly 400 mAh.g<sup>-1</sup>, according to the prior studies and maintain a high capacity in the 300 mAh.g<sup>-1</sup> for 100 cycles.  $V_2O_5$ -LiBO<sub>2</sub> glasses are being touted as potential cathode materials for Li-ion rechargeable batteries (Afyon et al., 2014).

As above-mentioned, manganese lithium borate glasses are potential candidate for advanced electrode materials, thus, this thesis work focuses on synthesis and characterizations of these materials. An electrical furnace with possibility of melt-quench process was used for preparing manganese lithium borate glass systems. In addition to the X-ray diffraction (XRD) technique, X-ray absorption spectroscopy (XAS) is employed to investigate the materials. XRD provides the information of long-range orders and phase formation. The information of local structures of the materials is obtained from XAS analyses. Furthermore, the electrical properties the materials were also studied by using cyclic voltammetry (CV).

## CHAPTER II

### LITERATURE REVIEW

#### 2.1 Definition of glass

Glass is a product of human civilization that dates back thousands of years. Glass piques people's curiosity because of its unique features, including as optical transparency, structural rigidity, and durability. All these properties make glass becoming for advanced technological uses such as laser glass, optical fibers, bio-glass, armor glass, solar glass, etc. Some examples of the many objectives and their corresponding products showing various uses of glass are shown in Figure 2.1.

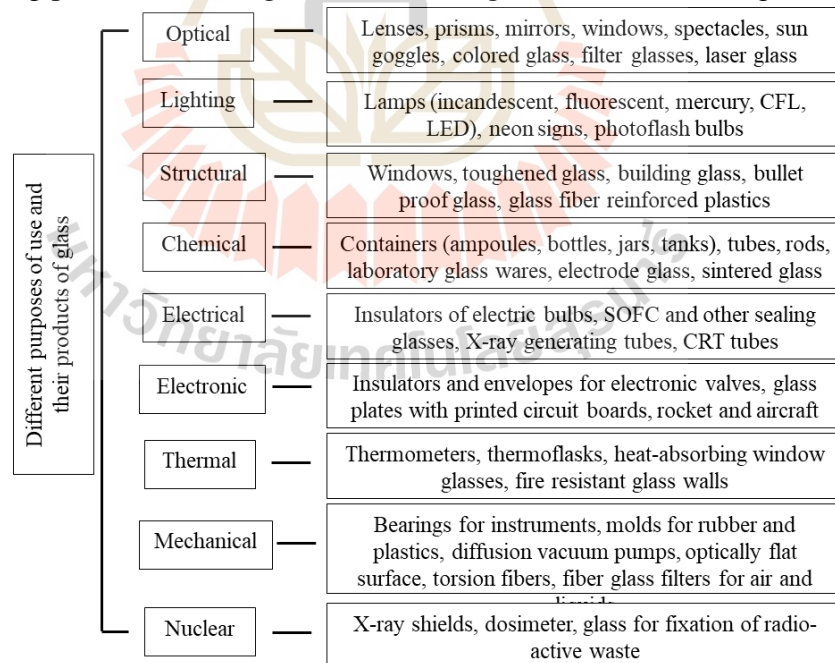


**Figure 2.1** Different objectives of use of glass (middle column) and their correspond products (right column) (Adapted from Karmakar et al., 2017)

It is critical to understand the connections between various kinds of glasses. As shown in Figure 2.2. As shown in this image, glass may be classified into two types based on its chemical composition: inorganic and organic glasses. Natural (obsidian or pechsteins) and synthetic (manmade or artificial) inorganic glasses are classified according to their origin. Natural glasses were discovered in volcanic rocks, while synthetic glasses were created by melting raw materials and using manufacturing expertise. Again, synthetic glasses may be classified into two types: standard and specialized. The glasses that we find around us and use on a daily basis (e.g., windows, tumblers, bottles, lights, eyeglasses, and mirrors) are generally referred to as common glass.

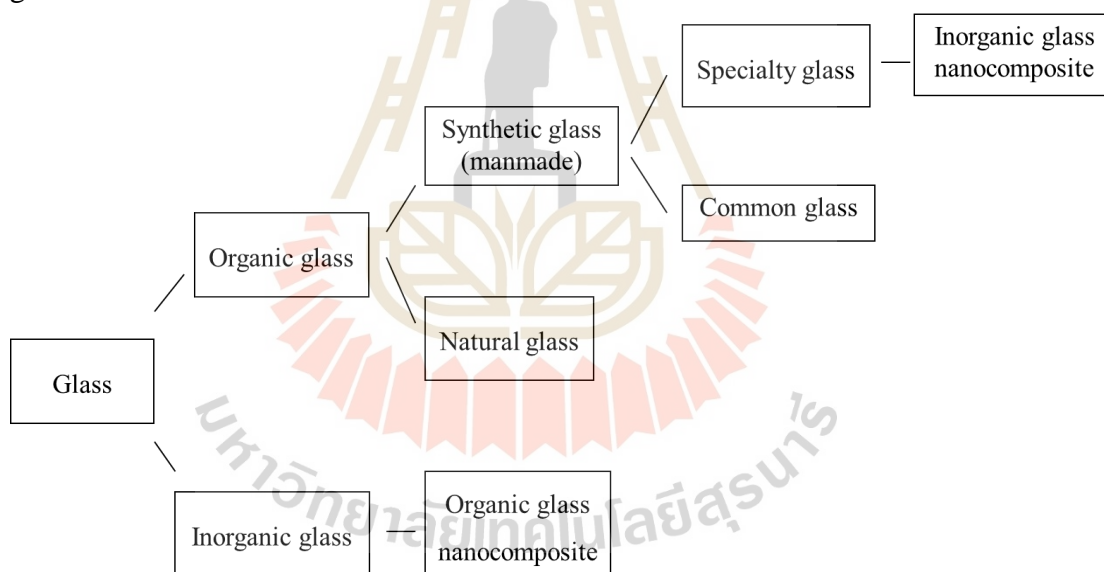


**Figure 2.2** The relationships of different types of glasses (Adapted from Karmakar, 2017).

The coordination number is used in both Goldschmidt's radius ratio criteria and Zachariasen's random network theory. Bond type is used in Smekal's mixed bonding rule and Stanworth's electronegativity rule; bond strength is used in Sun's single bond strength criteria; field strength is used in Dietzel's field strength criterion; and

topological constraint is used in Phillips' topological constraint. Rawson talks about a few of them, which are mainly of historical significance today. We'll focus on Zachariasen's hypothesis as well as the last three points.

Since the mechanical properties of glasses are identical to those of the corresponding crystals, Zachariasen concluded in a classic paper that the atomic forces in each would be of the same order. The diffuse nature of the X-ray diffraction spectra for glasses revealed that the unit cell of glass is indefinitely large. As a result, glass will be made up of a three-dimensional random network. Glass will have a higher intrinsic energy than crystal as a direct effect of the randomness. Zachariasen reasoned that the gap in internal energy between the two crystals would be negligible. Otherwise, the motivating force for crystallization will be necessary. He also indicated that this slight energy gap necessitated an inclusive and scalable structure.

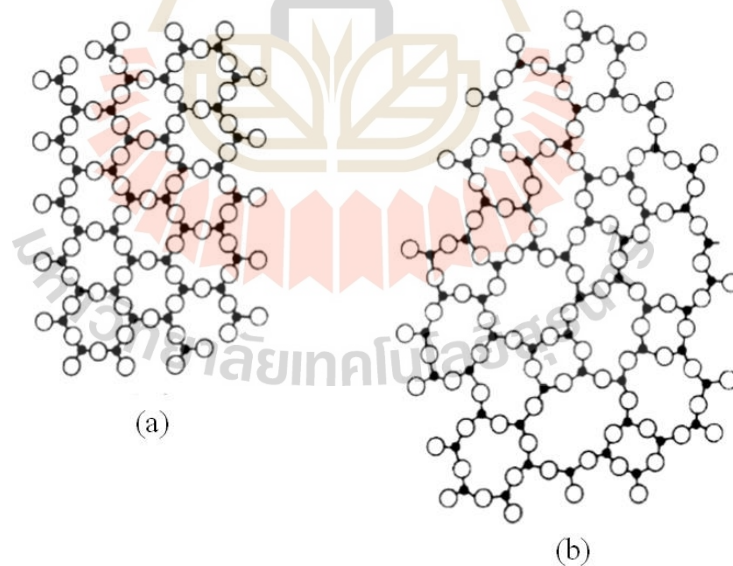


**Figure 2.3** Atomic structural representation of (a) A<sub>2</sub>O<sub>3</sub> crystal (b) A<sub>2</sub>O<sub>3</sub> glass.

The cation polyhedra in ionic crystals typically share corners. This is especially valid for cations with a limited radius but a lot of charge. Sharing corners, according to Zachariasen, is a primary condition for achieving a transparent and random system. As

a result, if the hypothetical compound  $AO_3$  will crystallize in two dimensions, the atomic structures in the crystal and the glass could resemble those in Figure 2.3. The crystalline and glassy types are all made up of  $AO_3$  triangles connected at the edges, with the glassy shape having disturbance introduced by variations in the A-O-A angles (also known as bond angles) and minor changes in the A-O bond duration. It should also be remembered that the triangles or O-A-O angles do not need much deformation.

## 2.2 Borate-based glass

Borate glasses are also gaining popularity due to their unusual properties. Borate glasses have a significant advantage over silica glasses in terms of melting and softening temperatures. Pure  $B_2O_3$  has a glass transition temperature ( $T_g$ ) of  $\sim 260^\circ\text{C}$  and a melting temperature ( $T_m$ ) of  $\sim 450^\circ\text{C}$ , which are significantly lower than  $T_g$  corresponding temperatures of  $\sim 1100^\circ\text{C}$  and  $T_m \sim 1728^\circ\text{C}$  for  $SiO_2$ . Borates, in their pure form, are ineffectual because of their chemical and practical resistance to water and their high preference for other compounds. Thus, it is used in conjunction with other oxides such as  $Al_2O_3$  or  $SiO_2$  at higher processing temperatures, which improves chemical stability at the expense of machining ease of expansion. Due to the lower melting point of borosilicate glass compositions for such applications can have less functional utility than those for other purposes. for processes like heat treating and vacuum subcritical applications are beneficial because they lower the risk of damaging the instruments, lasting effects that critical instruments will have at higher temperatures.

## 2.3 Lithium borate glasses electrode materials

### 2.3.1 Electrochemical property

Vanadium lithium borate glasses for cathode materials in rechargeable lithium-ion batteries have been researched by S. Afyon. As a cathode material for rechargeable LIBs, a glassy material from the  $\text{Li}_2\text{O}-\text{B}_2\text{O}_3-\text{V}_2\text{O}_5$  glass method, which will be referred to as  $\text{V}_2\text{O}_5\text{-LiBO}_2$  glass in the following document, has been published. At  $900^\circ\text{C}$  Celsius, a combination of 80%  $\text{V}_2\text{O}_5$  and 20%  $\text{LiBO}_2$  is melted. The glass content is created after quenching to room temperature. The cell is discharged with a capacity of 327 mAh/g, and again charged with a capacity of 308 mAh/g in the next step. In a standard  $\text{V}_2\text{O}_5\text{-LiBO}_2$  glass electrode fabrication, the active material (70 wt%) is (20 wt%). The galvanostatic cells made from such electrodes were measured by discharging to 1.5 V and then charging to 4.0 V at a rate of 50 mA/g. Figure 2.4 depicts the first ten galvanostatic charge/discharge curves of the  $\text{V}_2\text{O}_5\text{-LiBO}_2$  glass.

The rate capability of the  $\text{V}_2\text{O}_5\text{-LiBO}_2$  glass is shown in Figure 2.5. between 1.5 and 4.0 V. At rates of 50, 100, and 200 mA/g, the capacities of 293, 236 and 180 mAh/g are delivered, respectively. When the rate is raised to 400 mA/g on the 35th cycle, the discharge capacity decreases to 125 mAh/g, and then recovers to 260 mAh/g on the 45th cycle when the rate is 50 mA/g (Afyon et al., 2014).

Charging and discharging experiments of synthesized  $\text{LiMnBO}_3$  (II) at a voltage range of 1.5 - 4.5 V are shown in figure 2.6. The voltage range is 1.5 - 4.5 V (a). The initial discharge capacity is determined to be  $310 \text{ mAh.g}^{-1}$ , suggesting that

more than one Li atom may be intercalated and de-intercalated per formula unit (f.u) of  $\text{LiMnBO}_3$  (II) (Ragupathi et al., 2017).

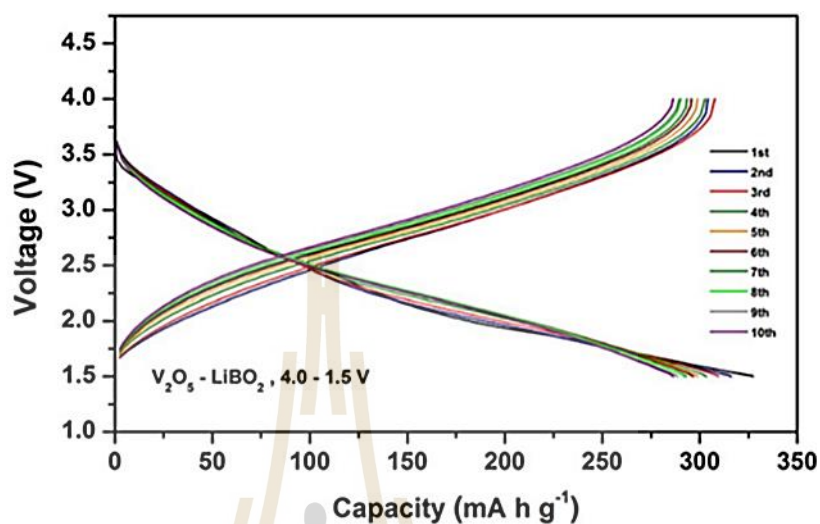


**Figure 2.4** The first ten charge/discharge curves of the  $\text{V}_2\text{O}_5$ - $\text{LiBO}_2$  glass within a potential window of 1.5 - 4.0 V at 50 mA/g rate (Afyon et al., 2014).

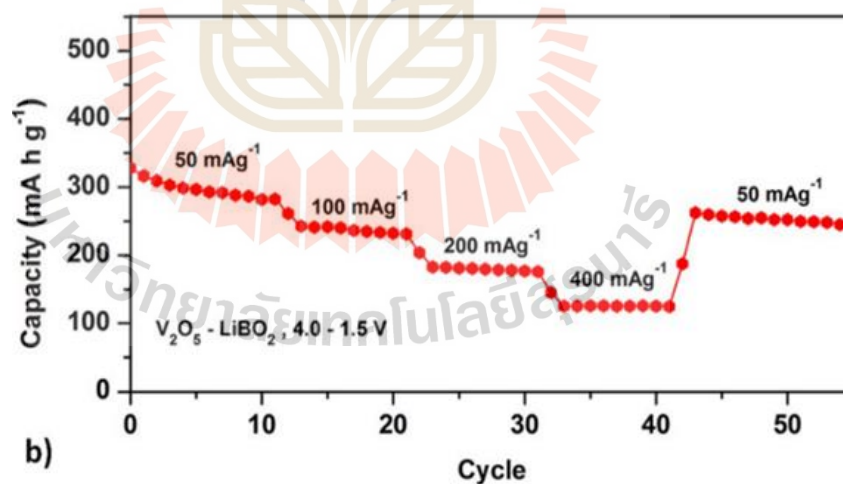


**Figure 2.5** The rate capability of the  $\text{V}_2\text{O}_5$ - $\text{LiBO}_2$  glass within 1.5 - 4.0 V at 50, 100, 200 and 400 mA/g rates at room temperature (Afyon et al., 2014).

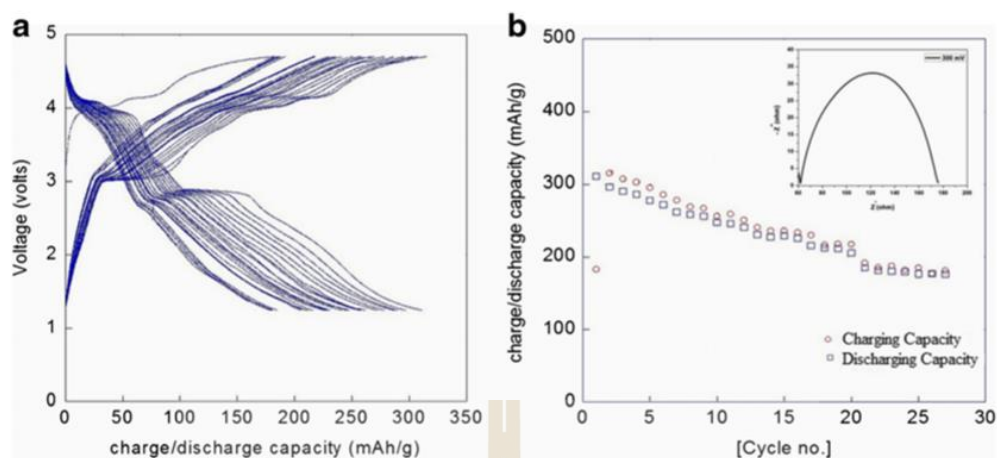


**Figure 2.6** Electrochemical measurements for  $\text{LiMnBO}_3$  (II) cathode material. a Charge– discharge studies. b Cycle life. Insert figure AC impedance spectra of  $\text{LiMnBO}_3$  (II).

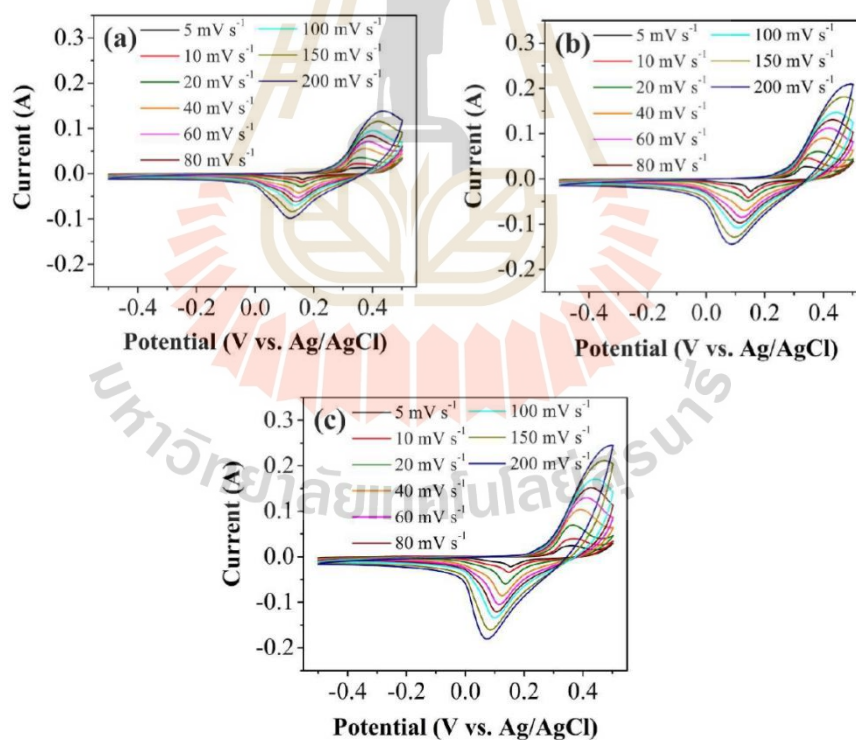


**Figure 2.7** Cyclic voltammograms of (a)  $0.2\text{MnO}_2-0.8(\text{Li}_2\text{O}-2\text{B}_2\text{O}_3)$ , (b)  $0.25\text{MnO}_2-0.75(\text{Li}_2\text{O}-2\text{B}_2\text{O}_3)$ , (c)  $0.3\text{MnO}_2-0.7(\text{Li}_2\text{O}-2\text{B}_2\text{O}_3)$  glass electrodes at different scan rates (Khajornrit et al., 2018).

The CV curves (Figure 2.7) for the  $0.20\text{MnO}_2\text{-}0.80(\text{Li}_2\text{O-}2\text{B}_2\text{O}_3)$ ,  $0.25\text{MnO}_2\text{-}0.75(\text{Li}_2\text{O-}2\text{B}_2\text{O}_3)$ , and  $0.30\text{MnO}_2\text{-}0.70(\text{Li}_2\text{O-}2\text{B}_2\text{O}_3)$  glass samples at different scan rates from  $5\text{ mVs}^{-1}$  to  $200\text{ mVs}^{-1}$  in  $6\text{ M KOH}$  electrolyte. The area of CV curve with different scan rate ( $5, 10, 15$  and  $20\text{ mVs}^{-1}$  in  $2\text{ M KOH}$  electrolyte) were used to calculate the specific capacitance (Khajornrit et al., 2018).

The estimated specific capacitances of the  $x\text{MnO}_2\text{-}(1-x)(\text{Li}_2\text{O-}2\text{B}_2\text{O}_3)$  glass sample are increased with increasing Mn content for  $x = 0.2, 0.25,$  and  $0.3$  samples, respectively, based on the area of the CV curve at a scan rate of  $200\text{-}5\text{ mVs}^{-1}$ . Interestingly, the specific capacitance of the  $x = 0.25$  and  $x = 0.3$  samples is about 2 times greater than the specific capacitance of the  $x = 0.2$  sample (Khajornrit et al., 2018).

The borate-based glasses have been produced and described using the VSM method, according to Laorodphan et al. The M-H loops of the glass samples at room temperature are shown in Figure 2.8. The magnetization of the  $0.5\text{V}_2\text{O}_5\text{-}0.5(\text{Li}_2\text{O-}x\text{B}_2\text{O}_3)$  samples with  $x=1.0$  and  $2.0$  varied linearly with the applied field, indicating that they were paramagnetic. Increased  $\text{B}_2\text{O}_3$  concentration results in a decrease in magnetization (Laorodphan et al., 2016).

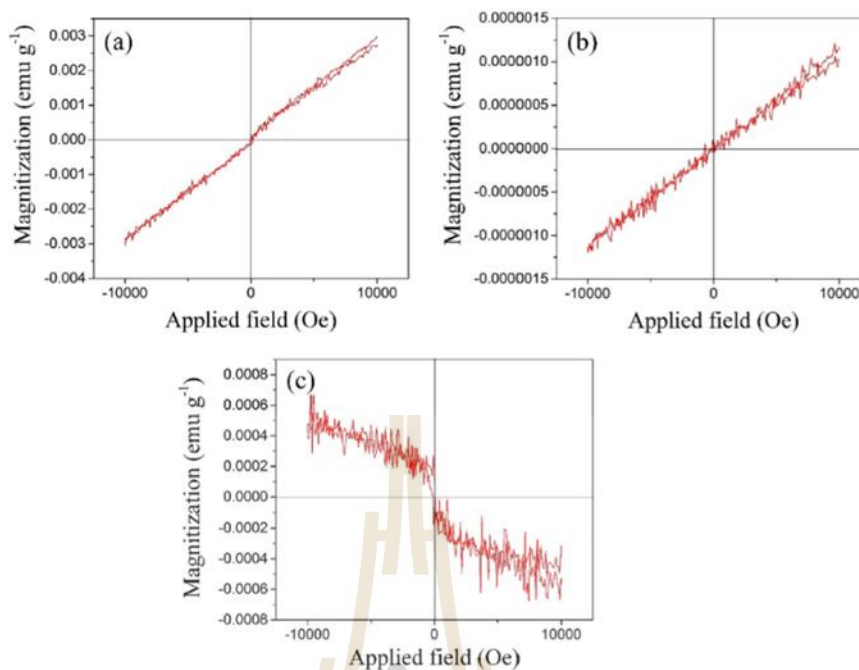


**Figure 2.8** Room temperature magnetization hysteresis loop of  $0.5\text{V}_2\text{O}_5\text{-}0.5(\text{Li}_2\text{O-xB}_2\text{O}_3)$  glass samples: (a)  $x=1$ , (b)  $x=2$ , (c)  $x=3$ . (Laorodphan et al., 2018)

### 2.3.2 Structural property

The atomic and molecular structures of the  $\text{LiMnBO}_2$  polymorphs in crystals are shown in Figure 2.9. Mn triangle constructs with planar hexagons on the edges (Legagneur et al., 2001). When monoclinic trimeric (having a single chiral centre) trigonal di-pyramidal structure is stated, each of the Li and Mn sites is seen as having one of the two an upper and lower than the other (Bondareva et al., 1978).

After conducting ab initio computations and calculating the monoclinic and monidoclinic  $\text{LiBO}_3$  voltage and energy density with regard to both a charge state transition and thermodynamic charge and discharge, we have gained an understanding

of the charge and discharge stability of both with respect to the difference in length that shown in Table 2.1.

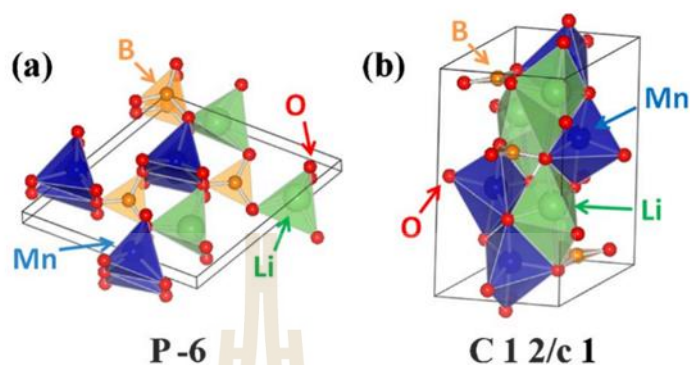


**Figure 2.9** Schematic diagrams of the (a) hexagonal and (b) monoclinic  $\text{LiMnBO}_3$  structure

**Table 2.1** Computed properties of the  $\text{LiMnBO}_3$  polymorphs.

Phase	Average voltage(V)	Theoretical Grav. Energy Density (Wh/L)	Theoretical Energy Density (Wh/L)	Vol. Density	Theoretical Capacity (mAh/g)
Hexagonal	4.11	912	2922		222
Monoclinic	3.70	822	2635		222

The hexagonal phase is the computationally expected ground state for  $\text{LiMnBO}_3$ , but the energy gap between it and the monoclinic phase of 5 meV per atom is near to the numerical precision limit for this process and small enough to be readily resolved by entropic results (Kim et al., 2011).

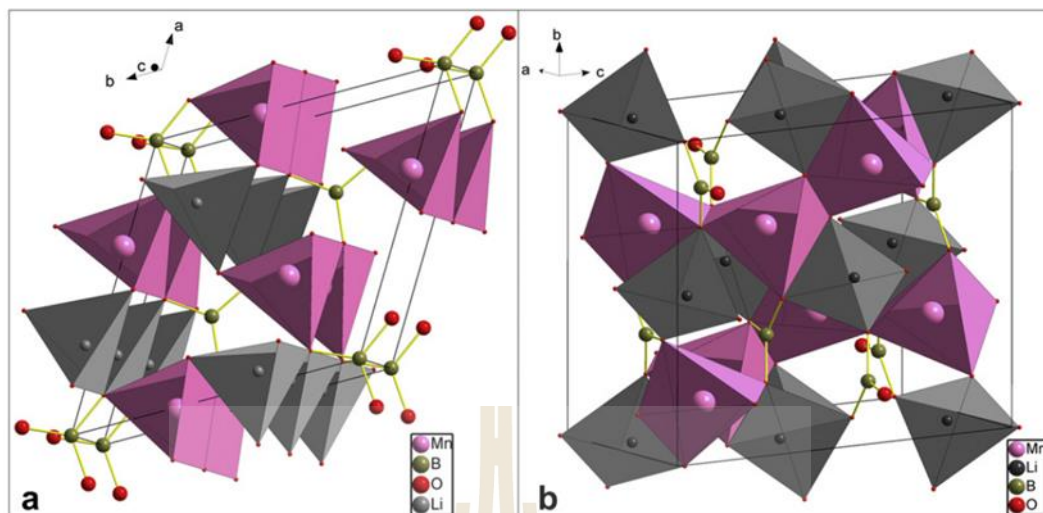


**Figure 2.10** Crystal structures of  $\text{LiMnBO}_3$ : a) skew [001] view of the hexagonal phase, b) skew [100] view of the monoclinic phase.

The crystal structures of the two  $\text{LiMnBO}_3$  modifications are seen in Figure 2.10. The hexagonal phase's arrangement is made up of  $\text{MnO}_5$  square pyramids that are linked by sharing their equatorial edges (Legagneur et al., 2001).  $\text{MnO}_5$  polyhedral chains extend along the  $c$ -axis and are linked together by planar  $\text{BO}_3$  groups. Li atoms are in tetrahedral coordination, and the  $\text{LiO}_4$  tetrahedra shape chains along the  $c$ -axis that are parallel to those of the square pyramids.  $\text{MnO}_5$  has a trigonal bipyramidal geometry in the monoclinic process (Figure 2.10b), which forms polyhedral chains by edge sharing along the direction (Bondareva et al., 1978). The preferred diffusion direction of Li ions in both phases has a one-dimensional character parallel to the  $c$ -axis, according to previous theoretical work (Kim et al., 2011).

Afyon et al. discovered a lithium-rich compound,  $\text{Li}_7\text{Mn}(\text{BO}_3)_3$ , that has a first discharge capacity of  $280 \text{ mAhg}^{-1}$  with an exchange rate of 3 Li per unit and a first discharge capacity of  $280 \text{ mAhg}^{-1}$  with an exchange rate of 3 Li per unit. The

thermalization of  $\text{Li}_2\text{O}$ ,  $\text{MnO}$  and  $\text{B}_2\text{O}_3$  in precise stoichiometric quantities resulted in the formation of the novel Li-rich compound  $\text{Li}_7\text{Mn}(\text{BO}_3)_3$ , which has been discovered. There are six separate  $\text{BO}_3^{3+}$  ions in the crystal structure of  $\text{Li}_7\text{Mn}(\text{BO}_3)_3$  (Figure 2.11), and only one of them is entirely connected to  $\text{Li}^+$  ions. These ions are crystallographically distinct ( $(\text{B-O}) = 1.31 - 1.43 \text{ \AA}$ ). In a tetrahedral manner, all additional borate units are linked to two  $\text{Mn}^{2+}$  ions ( $(\text{Mn-O}) = 2.01 - 2.08 \text{ \AA}$ ) and ten  $\text{Li}^+$  ions ( $(\text{Li-O}) = 1.87 - 2.21 \text{ \AA}$ ) in a tetrahedral fashion (Afyon et al., 2013).

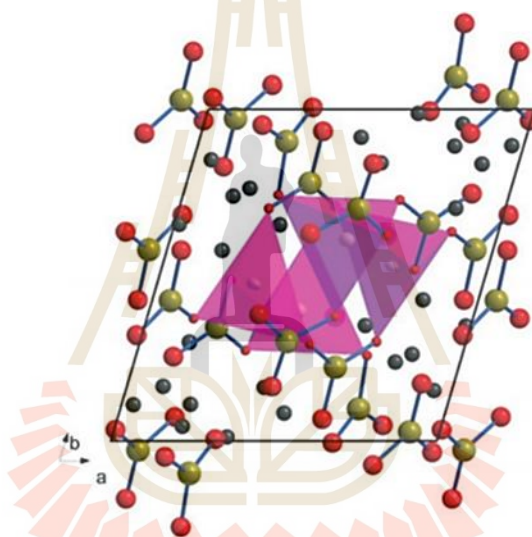


**Figure 2.11** View of the crystal structure of  $\text{Li}_7\text{Mn}(\text{BO}_3)_3$  along  $[001]$  corresponding to the direction of columns of linked  $\text{MnO}_4$  tetrahedra pairs (pink) interconnected by  $\text{BO}_3^{3+}$  ions (B green, O red, Li black). (Afyon et al., 2014)

The  $\text{MnO}_4$ -tetrahedra are arranged in columns that extend down the crystallographic  $c$ -axis (Figure 2.12), and the sole Li atoms are found in the first coordination spheres of the tetrahedra. Several  $\text{BO}_3^{3+}$  units join two tetrahedra together in pairs, while another unit connects the tetrahedra pairs together in the columns.  $\text{BO}_3^{3+}$

groups at the ends of the  $\text{MnO}_4$ -tetrahedra provide the fourth oxygen atoms required for formation (Afyon et al., 2014).

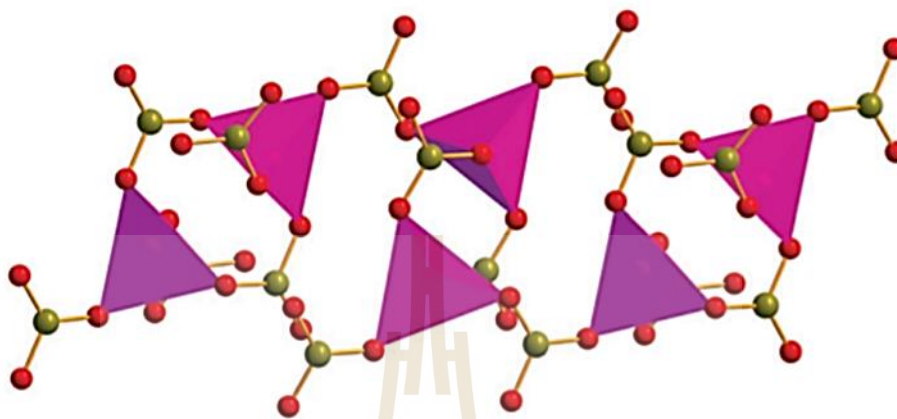


**Figure 2.12** Columns of pairs of  $\text{MnO}_4$  tetrahedra (pink) interconnected by  $\text{BO}_3^{3+}$  ions extending along the crystallographic c-axis showing one translational unit (B green, O red) (S. Afyon et al., 2013).

In comparison to other  $\text{Mn}^{2+}$  oxide compounds, Manganese's tetrahedral coordination at such a low oxidation state is unique to our knowledge. Typically,  $\text{MO}_6$  octahedra or  $\text{MO}_5$  ( $M = \text{Fe}, \text{Mn}, \text{and Co in LiMBO}_3$ ) polyhedral of trigonal bipyramidal or square-pyramidal geometry have been discovered most often. This tetrahedral coordination may aid in the stabilization of the borate manganate framework when it reaches higher oxidation states  $\text{Mn}^{n+}$  with  $n > 4$  (Afyon et al., 2013).

The manganese lithium borate glasses have been studied to application for cathode materials. Figure 2.13 shown the XPS result that confirmed the mixing of oxidation state of  $\text{Mn}^{2+}$  and  $\text{Mn}^{3+}$  in all glasses samples. The binding energy values of the glasses of  $\text{Mn}^{2+}$  and  $\text{Mn}^{3+}$  are  $\sim 641$  and  $\sim 643$  eV in the  $\text{Mn } 2p_{3/2}$  peak and  $\sim 653$  eV and  $\sim 655$  eV in the  $\text{Mn } 2p_{1/2}$  peak. The calculated  $\text{Mn } 2p_{3/2}$  of  $\text{Mn}^{2+}$  ( $\sim 641$  eV)/ $\text{Mn}^{3+}$

(~643 eV) ratio of 0.2MnO<sub>2</sub>-0.8(LB), 0.25MnO<sub>2</sub>-0.75(LB) and 0.3MnO<sub>2</sub>-0.7(LB) samples are 42.14/24.87%, 54.27/12.23%, 56.4/8.34%, respectively (Khajornrit et al., 2018).

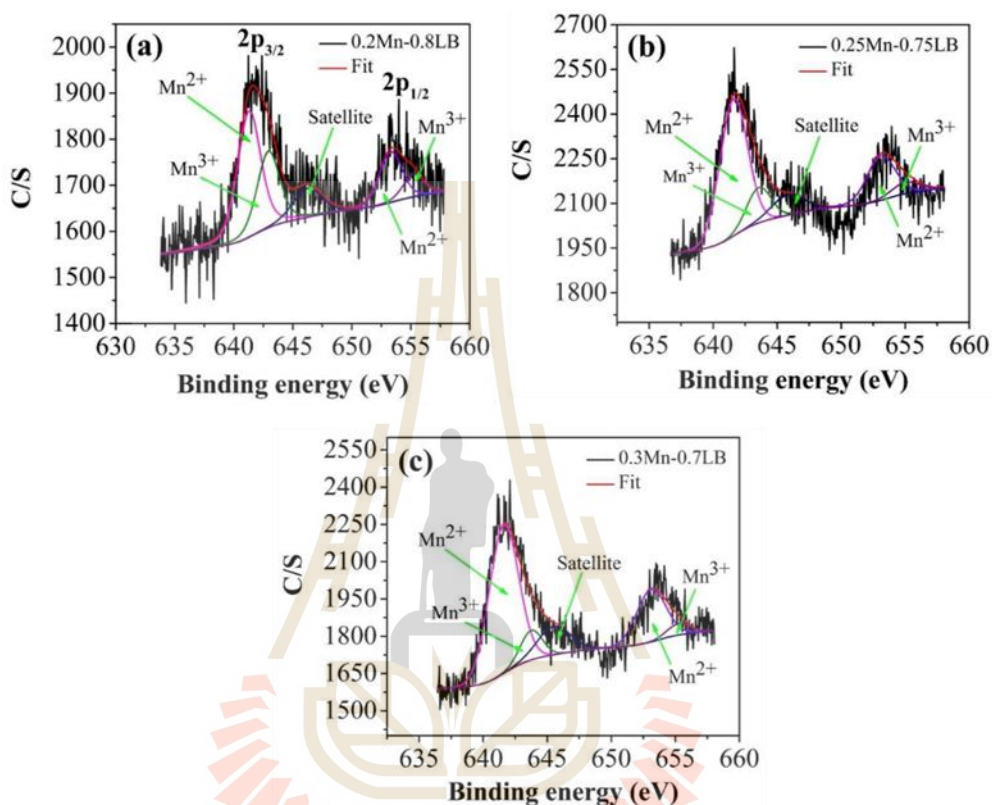


**Figure 2.13** XPS profiles of glass samples: (a) 0.2MnO<sub>2</sub>-0.8(Li<sub>2</sub>O-2B<sub>2</sub>O<sub>3</sub>), (b) 0.25MnO<sub>2</sub>-0.75(Li<sub>2</sub>O-2B<sub>2</sub>O<sub>3</sub>), and (c) 0.30MnO<sub>2</sub>-0.70(Li<sub>2</sub>O-2B<sub>2</sub>O<sub>3</sub>) (Khajornrit et al., 2018).

Specifically, LiMnBO<sub>3</sub> was the subject of Dr. Ragupathi's research. For analyzing the LiMnBO<sub>3</sub> (II), the spectrum is seen as being a combination of a Li, Mn, and O spectrum in Figure 2.14. It can be shown that Figure 2.14(a), which was found to be in similar studies to be exactly at 55.14 eV of binding energy (confirmed in the studies) (Andersson et al., 2002). The binding energies (Figure 2.14(b)) of carbonyl

oxygen and M bonding O pairs, respectively, lead to peaks in the oxygen range at 532.02 and 529.88 eV. The  $B^{1+}$  oxidation state of boron is shown by the B 1s peak in Figure 2.14(c), which is 191.24 eV. Mn (2p) spectra are seen in Figure 2.14(d), with binding energies of 642.47 and 653.97 eV corresponding to Mn ( $2p_{3/2}$ ) and Mn ( $2p_{1/2}$ ) energy levels, respectively.

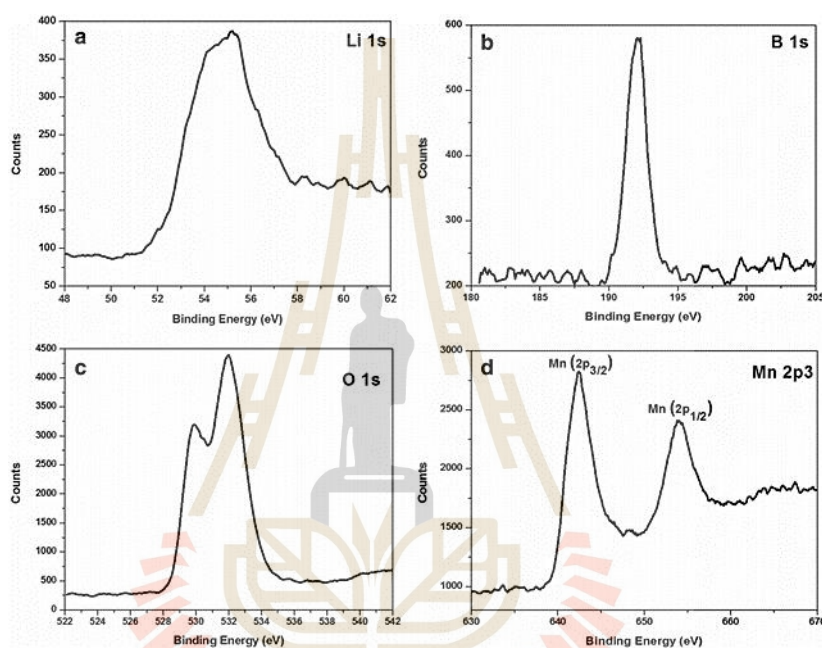


**Figure 2.14** XPS spectra of LiMnBO<sub>3</sub> (III) materials (a) Li 1s, (b) O 1s, (c) B 1s, and (d) Mn 2p (Andersson et al., 2002).

## CHAPTER III

### MATERIALS AND METHODE

#### 3.1 Glass preparation

The preparation of glasses samples was classified into two parts in this study, the lithium borate ( $\text{Li}_2\text{O}-x\text{B}_2\text{O}_3$ ) when  $x = 1, 2, 3,$  and  $4$  were firstly syntheses by melt quench method. The electric furnace was used for this research, the stoichiometric composition of raw materials is  $\text{Li}_2\text{CO}_3$ , 99.5% and  $\text{H}_3\text{BO}_3$ , 99.8% as shown in figure 3.1. The mixed were weight and mixed after that mixed were melted at  $1200^\circ\text{C}$  in platinum crucible and soaking for 2 hours. Then, the melted were quick quenched between stainless steel plate. The prepared lithium borate glasses were gridding and mixing with manganese dioxide ( $\text{MnO}_2$ , 99.0% as shown in figure 3.2) in agate mortar. The mixed powders were melted at  $1200^\circ\text{C}$  in rate  $10^\circ\text{C}/\text{minute}$  and soaking for 2 hours, after that the melted was quenched between stainless steel plate at room temperature. Finally, the glasses completely prepared and showed in brown color.



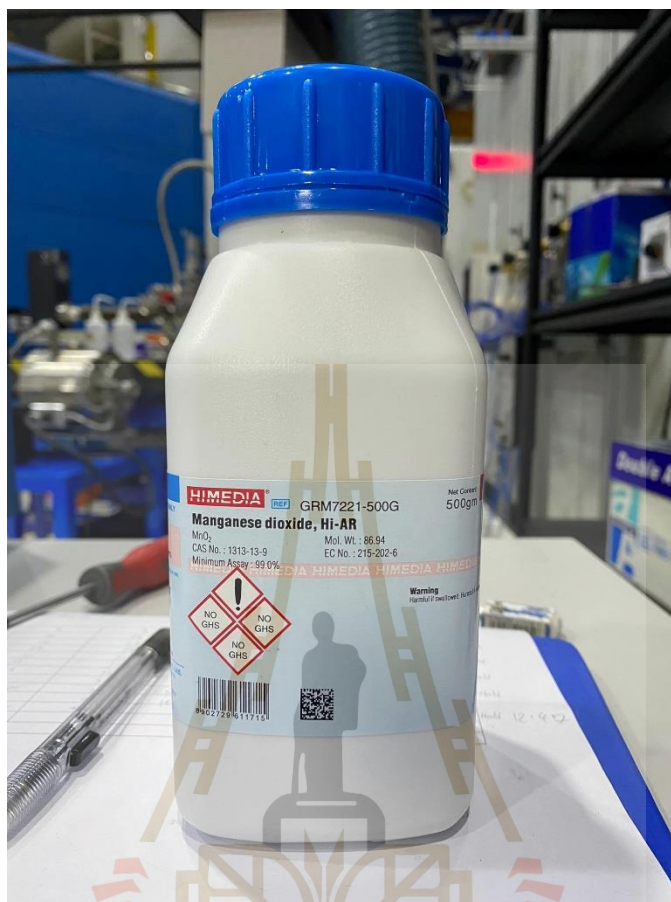


**Figure 3.2** Show the raw materials manganese dioxide (MnO<sub>2</sub>).

## 3.2 Characterization techniques

### 3.2.1 X-ray diffraction (XRD)

The X-ray diffraction analysis (XRD) technique is an important tool for analyzing material properties. It is an instrument that uses the X-ray diffraction method to analyze material properties. It can be used to determine both the compounds present in the sample and the crystal structure of the sample. The size of the unit cell in each sample's crystal is different, resulting in an uneven X-ray diffraction pattern. With the X-ray diffraction pattern, it was possible to find the relationships between different

substances. The procedure is based on the principles of diffraction and X-ray interference. When two or more waves pass through the same medium, interference becomes a combined wave, which is a combination of two phenomena: coherent and interference. Assume the wavelength has a specific phase.

When the X-ray is irradiated on the crystal surface, which is made up of rows of atoms. The atomic density of each layer of the crystal structure would be extremely high. The atomic coating on the surface scatters some of the X-rays. Another portion of the X-ray passes through the second layer, where some of it is dispersed, and some of it passes through the third layer of atoms, as seen in Figure 3.3.

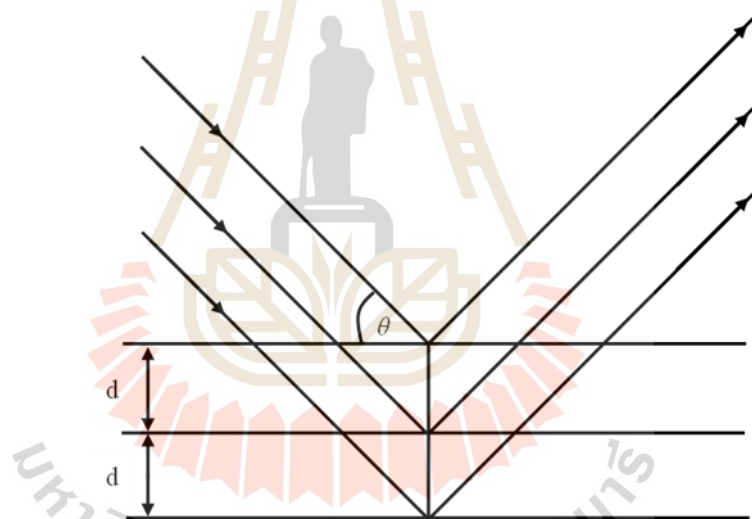


**Figure 3.3** Schematic diagrams of typical X-ray diffraction.

According to Bragg's Law, diffraction physics principles are used to explain the structure of a crystal when X-rays are incident at various angles of incidence, where the distance and wavelength change. The conditions are such that Bragg's Law equation is

$$n\lambda = 2d \sin \theta \quad (1)$$

where  $\theta$  is the scattering angle,  $n$  is a positive integer and  $\lambda$  is the

wavelength of the incident wave. Bragg's law relates the wavelength of electromagnetic radiation to the diffraction angle and the lattice spacing in a crystalline sample.

In this study, Rigaku-smartlab X-ray diffractometer specifications: max power 9 kW, X-ray generator Cu anode,  $K\alpha_1$ -1,544 Å, Detector 0D 1D 2D at Synchrotron light research institute (SLRI), Thailand (as seen in Figure 3.4) was used to characterize the nature of amorphous materials.



**Figure 3.4.** The Rigaku-smartlab X-ray diffractometer.

### 3.2.2 X-ray absorption spectroscopy (XAS)

X-ray Absorption Spectroscopy (XAS) is an important tool for studying atomic local structure and electronic states. X-ray absorption coefficient at the element's absorption edge. The oscillating electric field of electromagnetic radiation interacts with the electrons bound in an atom when X-rays of intensity  $I_0$  are incident on a sample, as shown in Figure 3.5. The radiation would either be dispersed or absorbed and excited by these electrons.

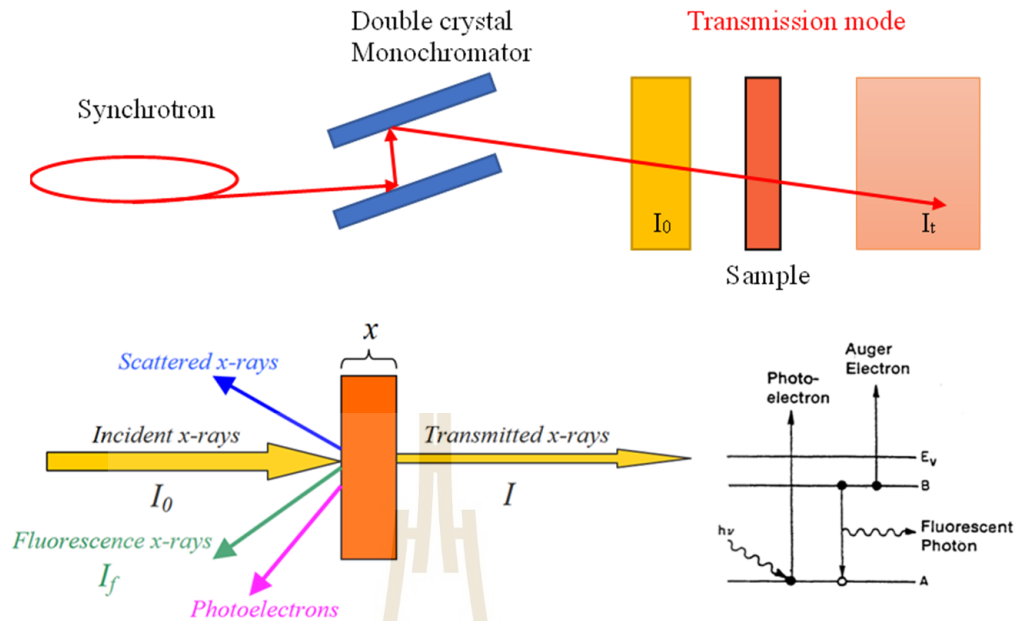


**Figure 3.5** Schematic of incident and transmitted X-ray beam.

The analysis of X-ray absorption of atoms in a sample using a synchrotron involves measuring the strength of incident X-rays and X-rays after passing through the sample. According to Beer Lambert's law, it is applied to the absorption coefficient as the equation (2).

$$I = I_0 e^{-\mu(E)x} \quad (2)$$

Where  $x$  is the thickness of the sample,  $I_0$  is the incident radiation intensity, and  $I$  is the radiation intensity that passes through the sample and  $\mu$  is transmission coefficient, which depends on the types of atoms. Since the absorption coefficient is dependent on the energy of the X-rays and independent of the thickness of the sample, the equation xx to find the X-ray absorption coefficient can be simplified by

$$\mu(E)x = \ln \frac{I_0}{I} \quad (3)$$

As the energy of the radiation increases, the absorption coefficient usually decreases. The graph of the relationship with energy has a sudden step edge called the absorption edge since there is a sufficient energy value that allows the sample to absorb a significant amount of radiation. As shown in Figure 3.6, the absorption edge has a variety of values that are dependent on the electron energy level.

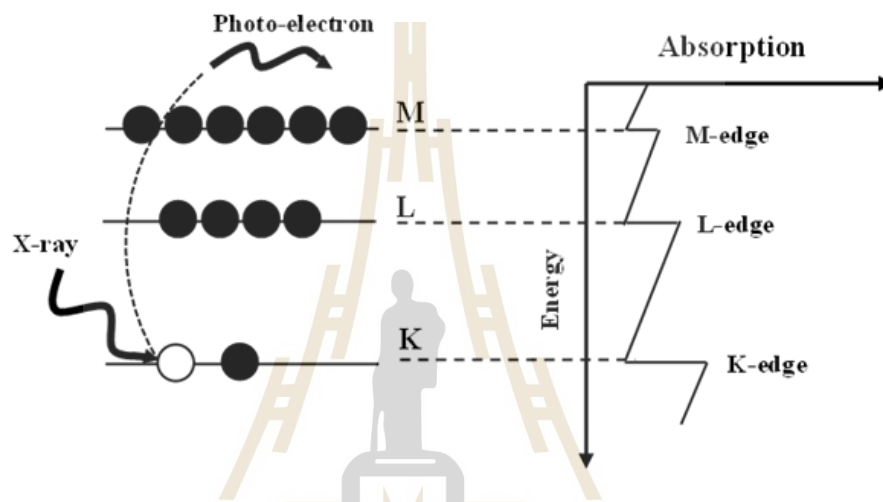


**Figure 3.6** The energy absorption edge depends on the electron energy level.

Absorption increases significantly at such energies, resulting in an absorption edge. When the incident photons have enough energy to excite the core electrons of the atoms that have been absorbed into a continuous state, each of these edges occurs. As a consequence, the electron binding energies in the absorbing elements' K, L, M, and other shells correspond to the absorbed radiation energies at these edges.

According to the mechanism of occurrence, the X-ray absorption spectrum is divided into two segments. The first section is known as X-ray absorption near-edge structure (XANES), which is a spectral range between 50 eV and the absorption edge. The extended X-ray absorption fine structure (EXAFS) is a part of the

spectra with energy between 50 and 1000 eV above the energy absorption edge shown in Figure 3.7.

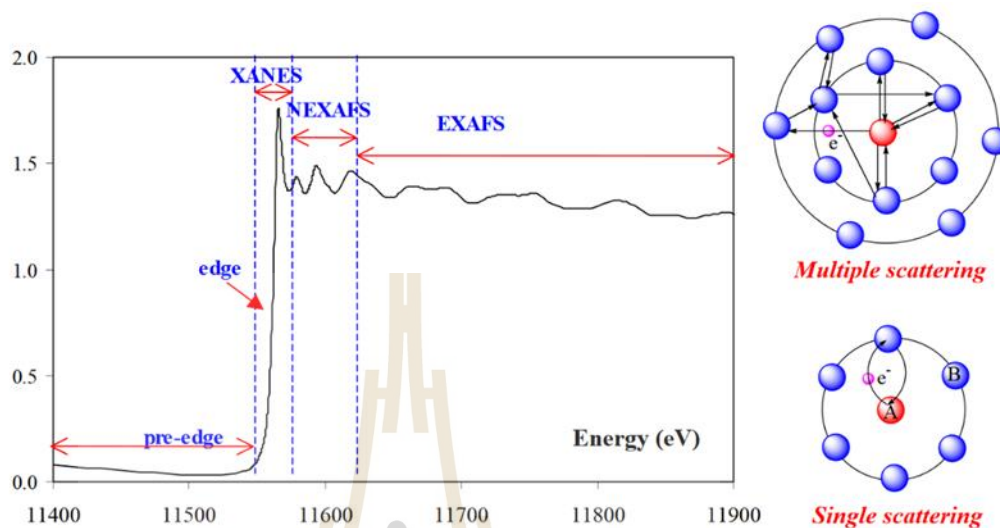


**Figure 3.7** Theoretical and algorithm for XANES and EXAFS spectra.

By comparing the sample spectra to the regular material spectra, the XANES spectra can be used to measure the oxidation state, phase, and structure of a sample. This is known as the fingerprint process, and it is based on four distinct XANES spectrum characteristics. The absorption edge is the first component of the XANES continuum. It is determined by the sample atom's oxidation state. As the oxidation state is changed from  $2^+$  to  $3^+$ , the absorption edge usually increases by 3 eV. As a result, XANES can be used to determine each oxide's oxidation state. Therefore, XANES can be used to determine each oxide's oxidation state. The pre-edge, or second element, is a small peak that appears before the absorption edge. If the atoms are in a less symmetrical structure, such as tetrahedral sites, the peak height is very high, and if the atoms are in a very symmetrical structure, the peak height is very low.

The spectral spire, also known as the white line, and the area after the spire, which is induced by multiple scattering, are two other distinct features of the

XANES spectrum. As a consequence, as shown in Figure 3.8, XANES can be used to distinguish the various oxide phases.

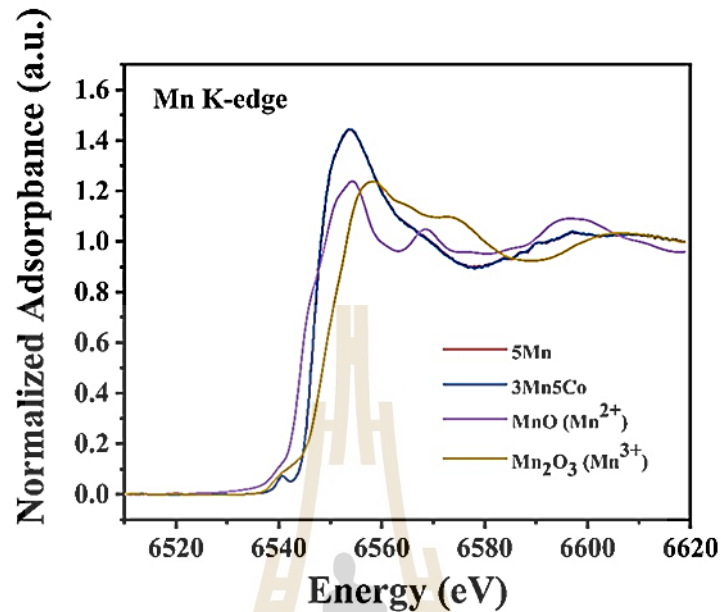


**Figure 3.8** The XANES spectrum of manganese k-edge.

Photoelectron scattering from the surrounding atoms creates a complementary and offset interference pattern in the EXAFS spectrum. By fitting the spectrum before and after the absorption edge, it can be used to determine the form and location of the absorbing atoms' surrounding atoms. Then, to normalize the spectrum, remove the history. The spectra behind the absorption edge are pulsed around an absorbance value of 1, and the pre-edge absorption is zero. The function  $\chi(E)$  is called the EXAFS function and is defined as

$$\chi(E) = \frac{\mu(E) - \mu_0(E)}{\Delta\mu_0(E)} \quad (4)$$

Where  $\mu(E)$  is the X-ray absorption coefficient while no other atoms are present, and  $\Delta\mu_0(E)$  is the height determined from the pre-absorption edge to the absorption's posterior edge, which is referred to as edge jump.

Since EXAFS signals are made up of several photon waves, the EXAFS mechanism is more likely to be based on wave number than on energy. As a result, the next process is to convert it to k-space, in which wave numbers are relative to energy.

$$k = \sqrt{\frac{2m(E-E_0)}{\hbar}} \quad (5)$$

Where  $E_0$  is the energy at the absorption edge, and  $m$  is the electron mass. When converting an EXAFS signal to k-space format, a wavenumber-dependent feature is used. Since the EXAFS signal is low and the region of  $k$  is large, it is usually weighted  $k^2$  or  $k^3$ , as shown in Figure 3.9(b). The final phase is the Fourier transform, as shown in Figure 3.9(a).

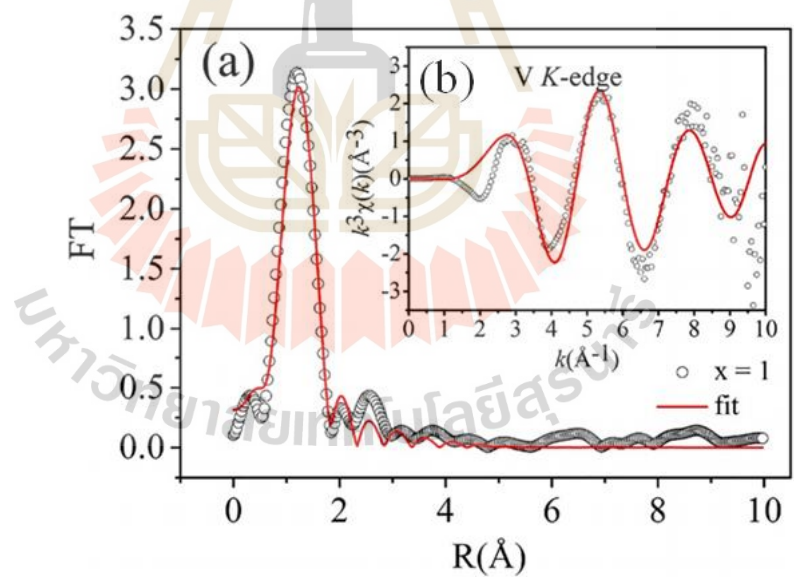


**Figure 3.9** The EXAFS fitting result (a) Fourier transform, and (b) k-space.

The theory behind analyzing the type and distance of neighboring atoms around absorbing atoms is that each neighbor atom has its own continuum, and  $z$  is the sum of all spectrums, which is written as: The EXAFS formula

$$\chi(k) = S_0^2 \sum_j \frac{N_j |f_j(k)|}{k |R_j^2|} e^{-2k^2 \sigma_j^2} \cdot e^{-2R_j/\lambda_j(k)} \cdot \sin[2kR_j + \phi_j(k)] \quad (6)$$

Where  $N_j$  is the number of surrounding atoms at a distance  $R_j$  from the absorbing atom evenly,  $|f_j(k)|$  is the atomic scattering amplitude,  $S_0^2$  is the amplitude reduction term,  $\phi_j(k)$  is the phase function.  $\sigma_j^2$  is the standard deviation of the  $R_j$  phase and  $\lambda_j(k)$  is the average distance of the moving electrons before they collide with other atoms.

Since EXAFS is a sine wave of several frequencies, each frequency corresponds to an atom in the absorption atom's area. As a result, as seen in the equation, the fourier transform may be used to analyze the type and distance.

The beamline 5.2 X-ray absorption spectroscopy from synchrotron light research institute (Thailand) was applied for indication the oxidation state of addition element in glasses samples. The beamline 5.2: XAS is a flagship beamline at SLRI, Thailand. Which is constructed under the SUT-NANOTEC-SLRI joint research facility project. The setup of the present beamline 5.2 SUT-NANOTEC-SLRI was shown in Figure 3.10. The technical information of this beamline was shown in Table 3.1.



**Figure 3.10** Shown setup of beamline 5.2 SUT-NANOTEC-SLRI, Thailand.

**Table 3.1.** The technical information of SUT-NANOTEC-SLRI beamline.

X-ray source	Synchrotron: bending magnet
Energy range	1240 - 12100 eV
Beam size at the sample	13 mm (width) x 1 mm (height) for transmission mode 20 mm (width) x 1 mm (height) for fluorescence mode
Flux	$10^8 - 10^{10}$ photon/s/100 mA
Energy resolution	$2 \times 10^{-4}$ /light energy
Experiment setup	Transmission mode with ion chamber Fluorescence mode with 4-element silicon detector
Crystal type	KTP (001): 2d spacing ( $\Rightarrow$ ) = 10.955

	: energy range = 1250 - 4780 eV
	InSb (111): 2d spacing ( $\Rightarrow$ ) = 7.481
	: energy range = 1830 - 7000 eV
	Ge (220): 2d spacing ( $\Rightarrow$ ) = 7.481
	: energy range = 3440 – 12100 eV

The synchrotron-based is an advance technique for study advance materials which includes four importance part namely electron gun, linear accelerator, booster ring and storage ring. The synchrotron light was produced by accelerating electron up to near light speed. Then, using magnetic force field to enforce the light to curve for emit photon energy. The electron gun, linear accelerator, booster ring and storage ring was shown in Figure 3.11.

a)



b)



c)





**Figure 3.11** Synchrotron experimental hall at the Light Research Institute.

### 3.2.3 Vibrating sample magnetometer (VSM)

The vibration sample magnetometer (VSM) is a device that measures the magnetic properties of a material using Faraday's Law's magnetic induction theory. The magnetic properties of the sample are calculated by vibrating it in a region with a constant magnetic field. In VSM, a sample magnetized by a homogenous magnetic field is vibrated at a small and fixed amplitude with respect to stationary pick-up coils (Figure 3.12). The resulting field change  $\partial\mathbf{B}(t)$  at a point  $r$  inside the detection coils induces voltage and is given by

$$V(t) = \sum_n \int_A \frac{\partial\mathbf{B}(t)}{\partial t} \cdot d\mathbf{A} \quad (7)$$

where  $\mathbf{A}$  is the area vector of a single turn of the coil and the summing is done over  $n$  turns of the coils.  $\mathbf{B}(t)$  is given by the dipolar approximation, assuming small dimensions of the magnetized sample in comparison to its distance from the detection coils<sup>8</sup>

$$\mathbf{B}(\mathbf{r}) = \frac{\mu_0}{4\pi} \left( \frac{\mathbf{m}}{r^3} - \frac{3(\mathbf{m} \cdot \mathbf{r})\mathbf{r}}{r^5} \right) \quad (8)$$

and

$$\frac{\partial \mathbf{B}_i(t)}{\partial t} = \frac{\partial \mathbf{a}(t)}{\partial t} \cdot \nabla_r \{ \mathbf{B}(\mathbf{r}) \}_i \quad (9)$$

Where  $\mathbf{a}(t)$  being the position of the dipole and  $\{ \mathbf{B}(\mathbf{r}) \}_i$ ,  $i = 1, 2, 3$ , the  $i$ th component of  $\mathbf{B}$  at  $\mathbf{r}$  due to dipole  $\mathbf{m}$ .  $V(t)$  can be detected to a high resolution and accuracy by means of suitable associated electronics. For stationary pick-up coils and a uniform and stable external field, the only effect measured by the coils is that due to the motion of the sample. The voltage  $V(t)$  is thus a measure of the magnetic moment of the sample. In this experiment, the vibrating sample magnetometer (VersaLab™ - 3 Tesla, Cryogen-free, Quantum Design, Inc., USA) was used (Khon kaen university).



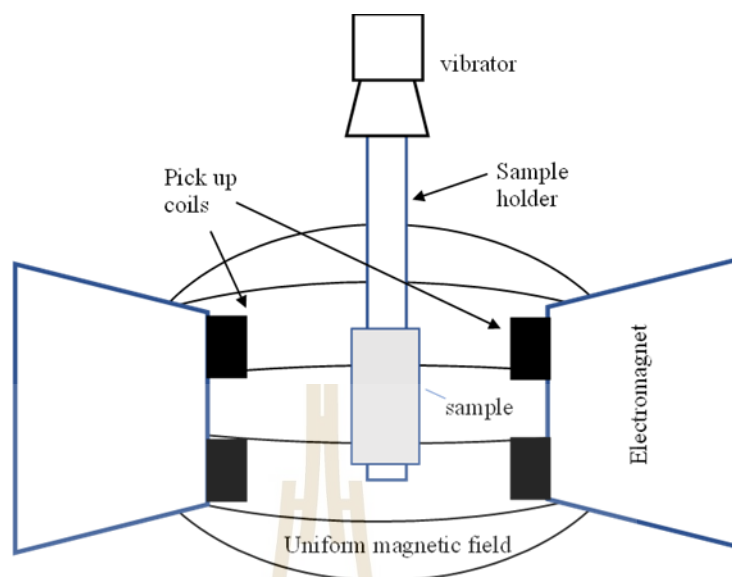


**Figure 3.12** Schematic diagrams of vibration sample magnetometer.

### 3.2.4 UV visible spectrometer (UV-vis)

UV / VIS Spectrophotometer It is an instrument used to measure the amount of light and intensity in the UV range and the white light that penetrates or is absorbed by the sample placed in the instrument. The wavelength is related to the amount and type of substance in the sample, mostly organic material. Complex compounds and inorganic compounds capable of absorbing light at these wavelengths.

When a sample molecule is irradiated with optimum UV or white light, the electrons inside the atom are absorbed and transform into a higher energy level. The amounts of light that passes through or is reflected from a sample is calculated toward light of various wavelengths from a source. According to Beer-Lambert's law, the absorbance of a substance is proportional to the number of molecules being absorbed, that shown in equation xx. Therefore, this technique can be used to determine the type and number of substances present in a sample.

$$A = \epsilon cl = \ln \frac{I_0}{I} \quad (10)$$

Where  $A$  is an absorbance,  $\epsilon$  is absorptivity,  $c$  is molar concentration of solute,  $l$  is pathlength,  $I_0$  is intensity of light incident upon sample cell and  $I$  is intensity of light leaving sample cell.

The Perkin Elmer Lambda 950 UV-Vis-NIR, double beam, double monochromator spectrophotometer was used in this study. The UV area is illuminated by a deuterium light, while the Vis/NIR region is illuminated by a tungsten lamp. An optical design is shown in Figure 3.13. It's important to note that reflectance includes both specular and diffuse elements. The characteristic reflectance measurements are installed in the reflecting sample holder, set to face the beam at an angle of  $8^\circ$  to our own line of sight (quasi-parallel).



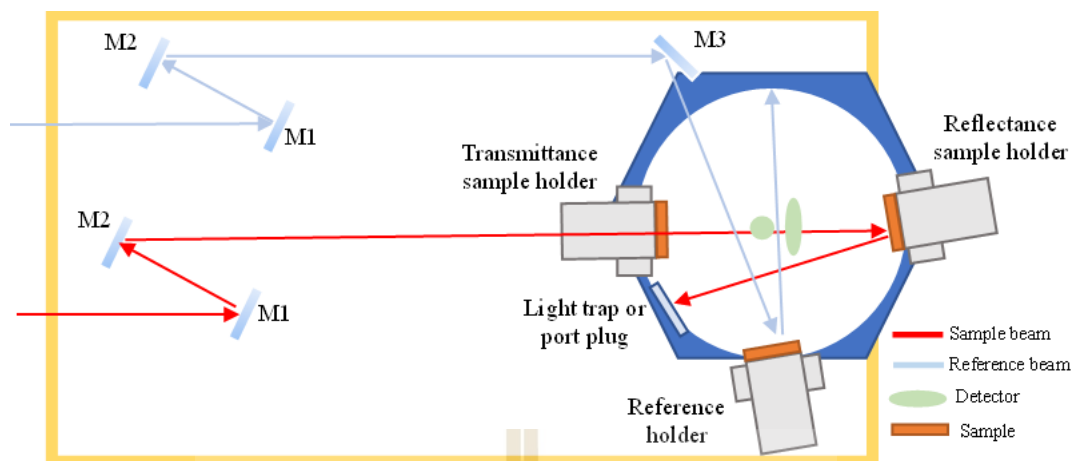


**Figure 3.13** Schematic diagrams of typical UV-visible spectrometer.

### 3.2.5 Scanning electron microscopy (SEM)

Scanning Electron Microscopy is a type of electron microscope that takes pictures of a target by scanning. The sample surface with a high-energy beam of electrons is emitted by the Electron gun when the electron hits the surface. It can release signals, can process and provide information about the surface of an object, surface elements and other properties.

The principle of SEM is shown in Figure 3.14. The topmost is the electron gun. The electrons from the source are accelerated downward along with the column, which is vacuumed. Accelerating potential in the range of 0-50 kV with direction of motion is controlled by an electromagnetic lens. In general, the electromagnetic lens has two or more sets. The number of electrons is regulated by the aperture.

The condenser lens, the first is electromagnetic lens, it is the most critical instrument for monitoring electron optics. Since it compressed the electrons down from the source through a smaller cross-sectional area electron beam. The second

set of electromagnetic lenses is the object lens. This is the final set of lenses that direct the electron beam on to sample's surface in combination with the scan coil. The sample's surface field, or the area hit by the electron beam, can generate several types of signals concurrently. A detector detects the signal, which is then converted into a picture shown on the monitor. An example of the resulting signal is Secondary Electrons. This signal provides information about the surface condition of the sample. This is the signal that is most used to create images. The image obtained from this type of signal is called Secondary Electron Image. For examples, Secondary Electrons (SE) are one kind of resulting signal. This signal indicates the state of the sample's surface. This is the most often used signal for picture generation. Secondary Electron Image (SEI) refers to the image generated by this type of signal. Moreover, Back Scattering Electrons (BSE) are signals that indicate the chemical structure of the sample surface. Along with these signals, there are those such as X-ray, electromagnetic waves, Auger electrons, and others that each have unique knowledge regarding the sample. In this experiment, scanning electron microscopy (FEI, QUANTA450) was used (at synchrotron light research institute, SLRI).



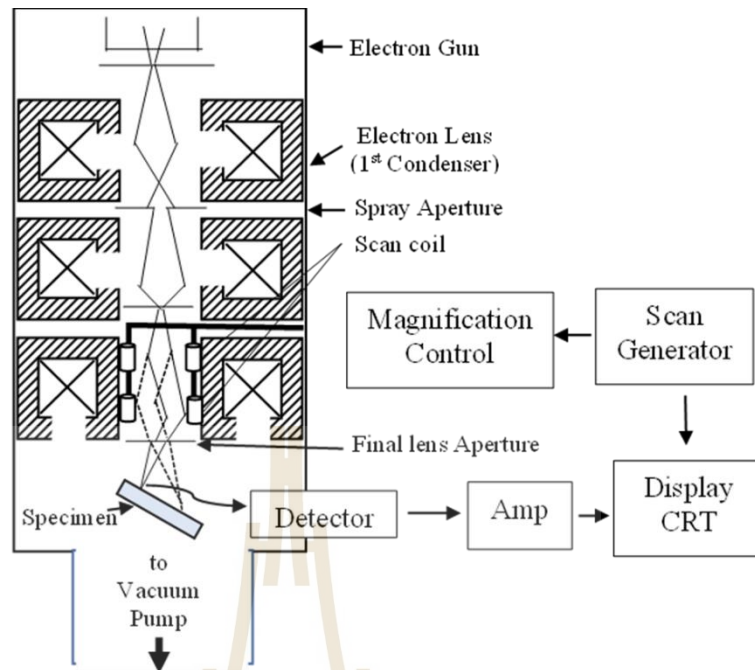


**Figure 3.14** Schematic diagrams of typical scanning electron microscopy.

### 3.2.6 Energy dispersive X-ray spectroscopy (EDS)

The determination of elemental composition of a sample using a scanning electron microscope involves energy dispersive X-ray spectroscopy. Elements with an atomic number greater than boron can be discovered with EDX at concentrations of at least 0.1 percent. EDX is used for a variety of purposes, including material identification and assessment, quality control monitoring, and contaminant detection. The initial beam of electron interacting with the nucleus of the sample atom produces an X-ray. The electron in the nucleus of an atom will be excited by a primary electron beam, generating an electron hole by ejecting it from the nucleus. An electron from higher energy shell of the atom will replace the electron hole and release the energy. The emitted X-ray consists of X-ray continuum and characteristic X-ray as shown in figure 3.15.

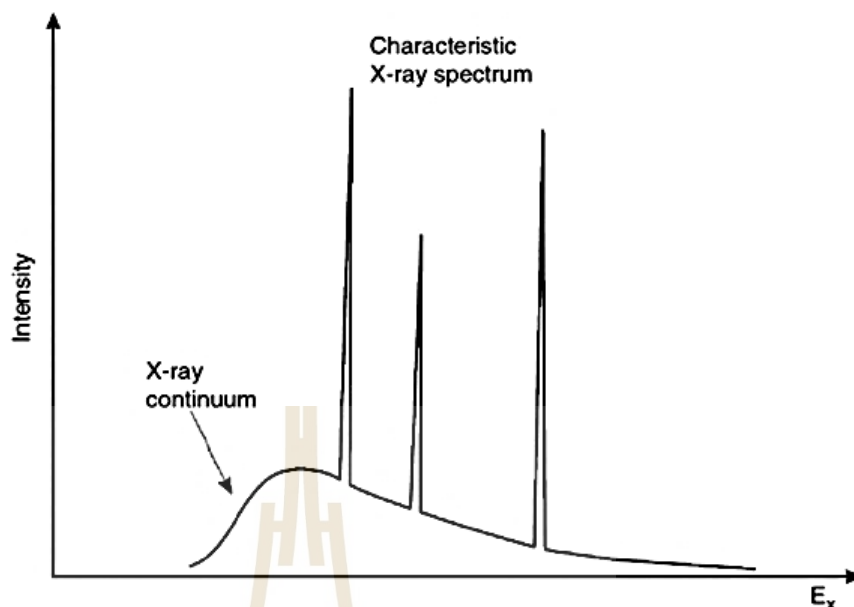


**Figure 3.15.** Schematic representation of the types of X-ray spectrum emitted upon bombardment of fast electron.

### 3.2.7 Electrochemical measurement

The electrochemical properties of all the glasses were studied in 6M KOH electrolyte by potentiostat/galvanostat (METROHM AUTOLAB, PGSTAT302N 30V/200mA) connected with a three-electrode configuration, which consist of platinum (Pt) wire, Ag/AgCl and the prepared glass samples as counter, reference and active electrode (as seen in Figure 3.16). Moreover, NOVA software is used to control the accessories and analyze the data. For the electrode preparations, the electrodes were prepared by mixing of the glass samples with polyvinylidene fluoride (PVDF) and carbon black in the ratio 80:10:10. The mixture were mixed with the N-methyl-2-pyrrolidinone. The slurry was then pasted on a nickel foam substrate (area  $\sim 1 \text{ cm}^2$ ). The cyclic voltammogram (CV) was tested in a voltage window between -1.2 V and 0.5 V. Additional, the specific capacitance can be calculated by using below equation.

$$C_{cv} = \frac{1}{vm\Delta V} \int IdV \quad (11)$$

Where  $v$  is the scan rate ( $\text{mV s}^{-1}$ ),  $m$  is the mass of active materials(g),  $\Delta V$  is the potential window(V) and  $I$  is the response current(A).

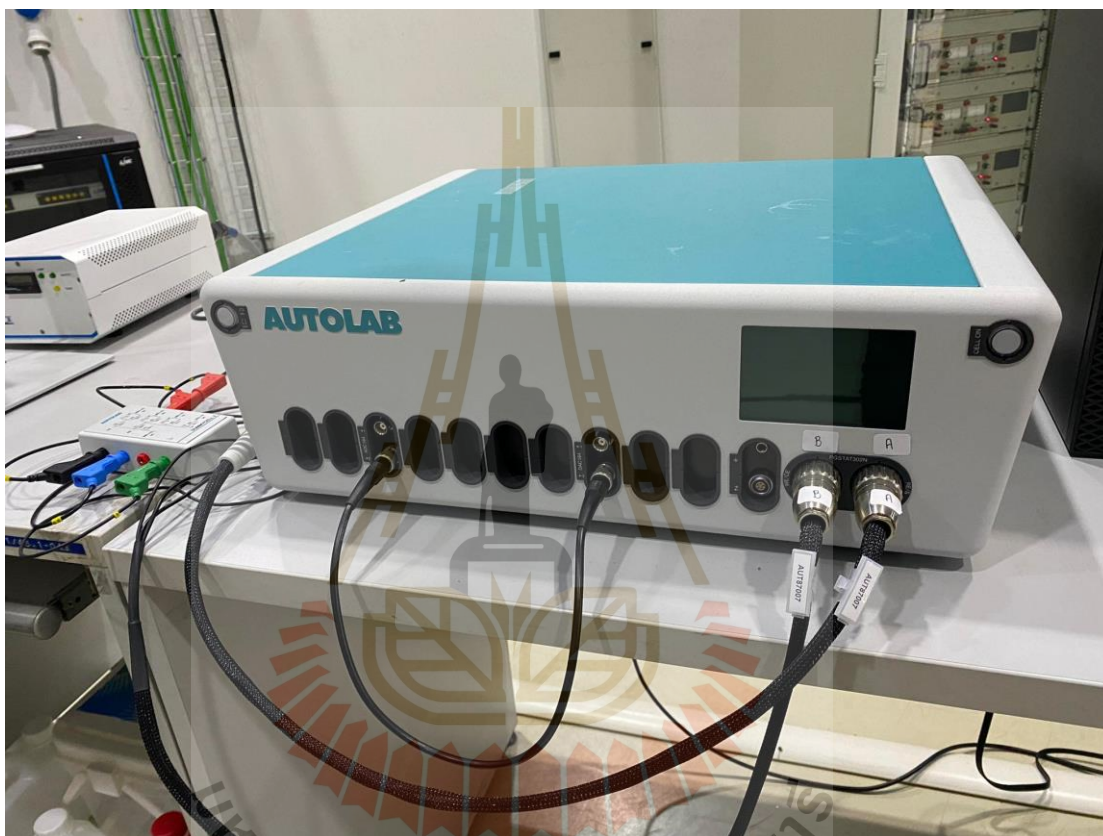


**Figure 3.16** Show Metrohm autolab equipment at beamline 2, SLRI.

## **CHAPTER IV**

### **RESULT AND DISCUSSION**

This chapter presents the experimental results and discussion, which is divided into two parts. The first section contains the results of the melt quench process used to prepare the glass samples. The second is the results from the characterizations of the glass samples using a variety of techniques, including XAS, SEM, UV-VIS, VSM, XPS, and XRD, as well as comparing various properties. It is noted that, in each set of the glass sample, only boron content was varied.

#### **4.1 Glass preparation**

The preparation of the glasses samples was divided into two stages; first, the lithium borate was prepared using the melt-quench process. This study used an electric furnace, and the stoichiometric composition of raw materials was determined by weight and mixing. The mixture was melted at 1200°C in a platinum crucible and soaked for 2 hours. The molten material was then quickly quenched between two stainless steel plates. The prepared lithium borate glass is shown in Figure 4.1.

The prepared lithium borate glasses were ground and mixed with manganese dioxide. The mixed powders were melted at 1200°C at a rate of 10°C/minute and soaked for 2 hours before being quenched at room temperature between stainless steel plates as shown in figure 4.2. Finally, the clear glasses were fully prepared and revealed a brown color as seen in Figure 4.3.



**Figure 4.1** The prepared lithium borate glass by melt-quench technique.



**Figure 4.2** The quenching process on glasses preparation.

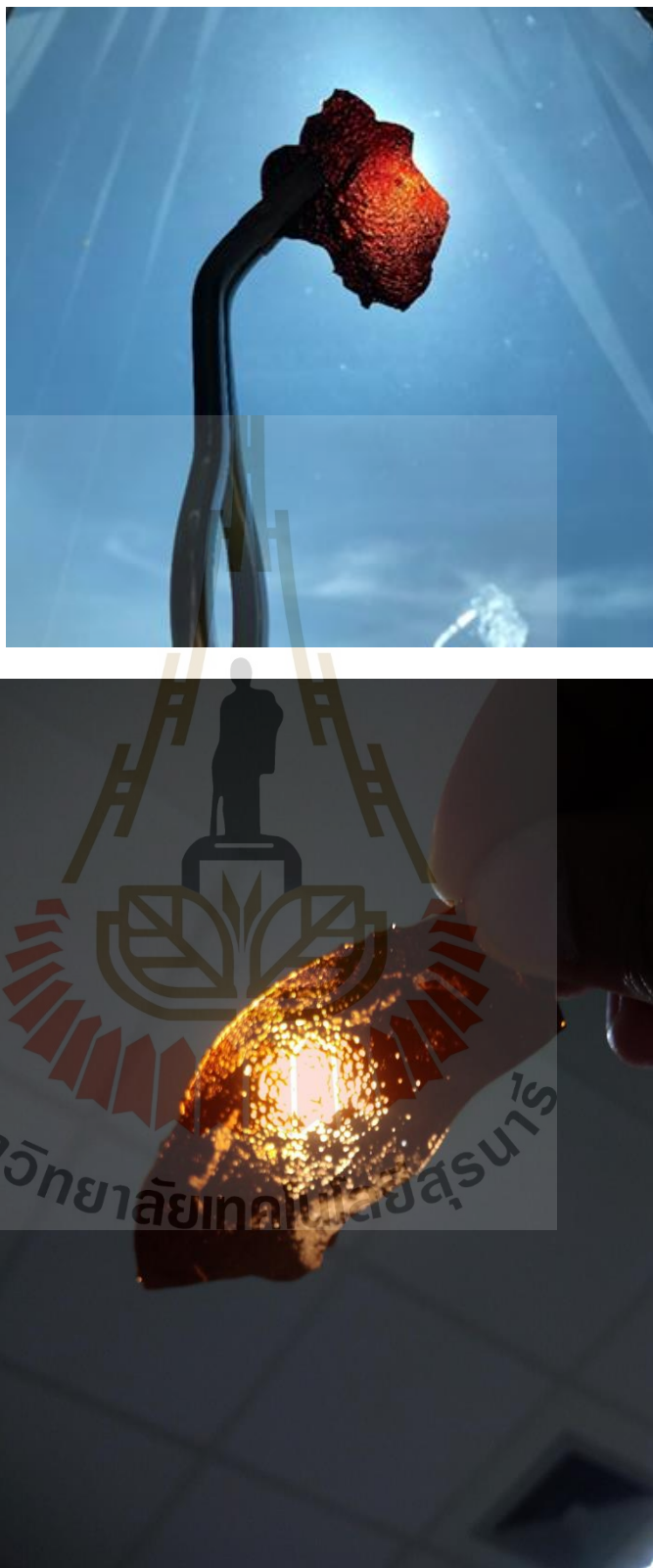


**Figure 4.3** The prepared manganese lithium borate glass by melt-quench technique.

## 4.2 X-ray diffraction spectroscopy results

The XRD technique is considered to verify each sample's amorphous process. The samples glasses powder was analyzed, and the diffract-grams were set to operate in a step of  $0.05^\circ$  over a two-theta range of  $10^\circ$  to  $90^\circ$ . As shown in Figure 4.4, the XRD patterns of all glass are wide with no definable sharp peak. The broad band peak indicates the samples amorphous process. Additionally, the rise in peak intensity confirms the increase in glassy condition with enhanced boron material.

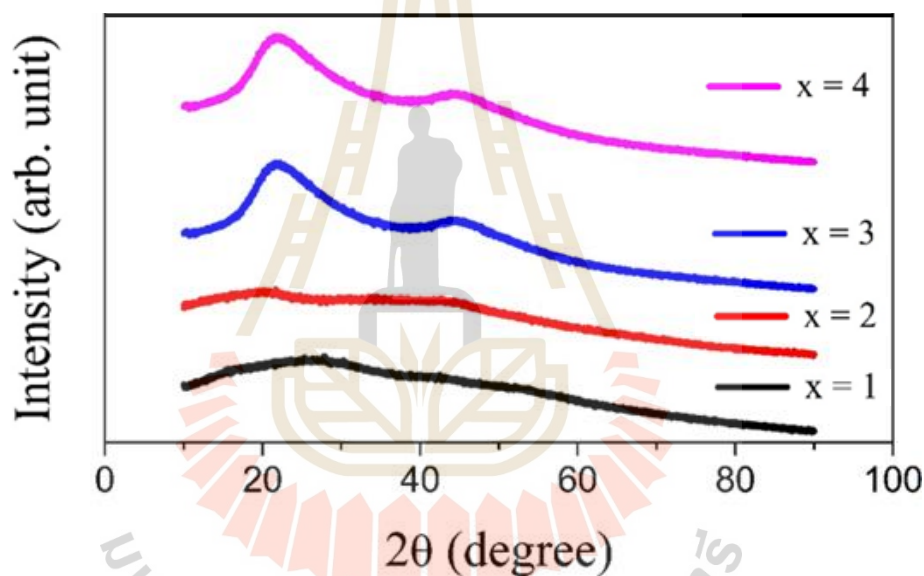
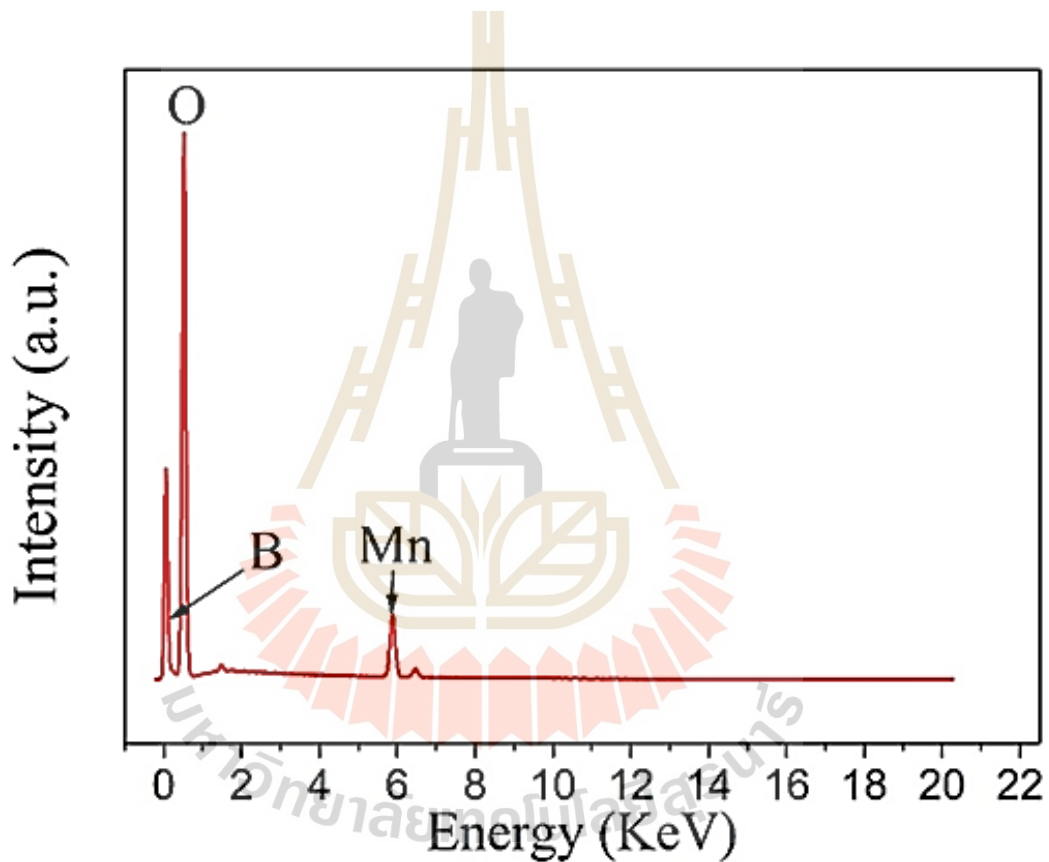


**Figure 4.4** X-ray diffraction of  $0.2\text{MnO}_2\text{-}0.8(1\text{Li}_2\text{O-xB}_2\text{O}_3)$  where  $x = 1, 2, 3$  and  $4$  (mol%) glass samples.

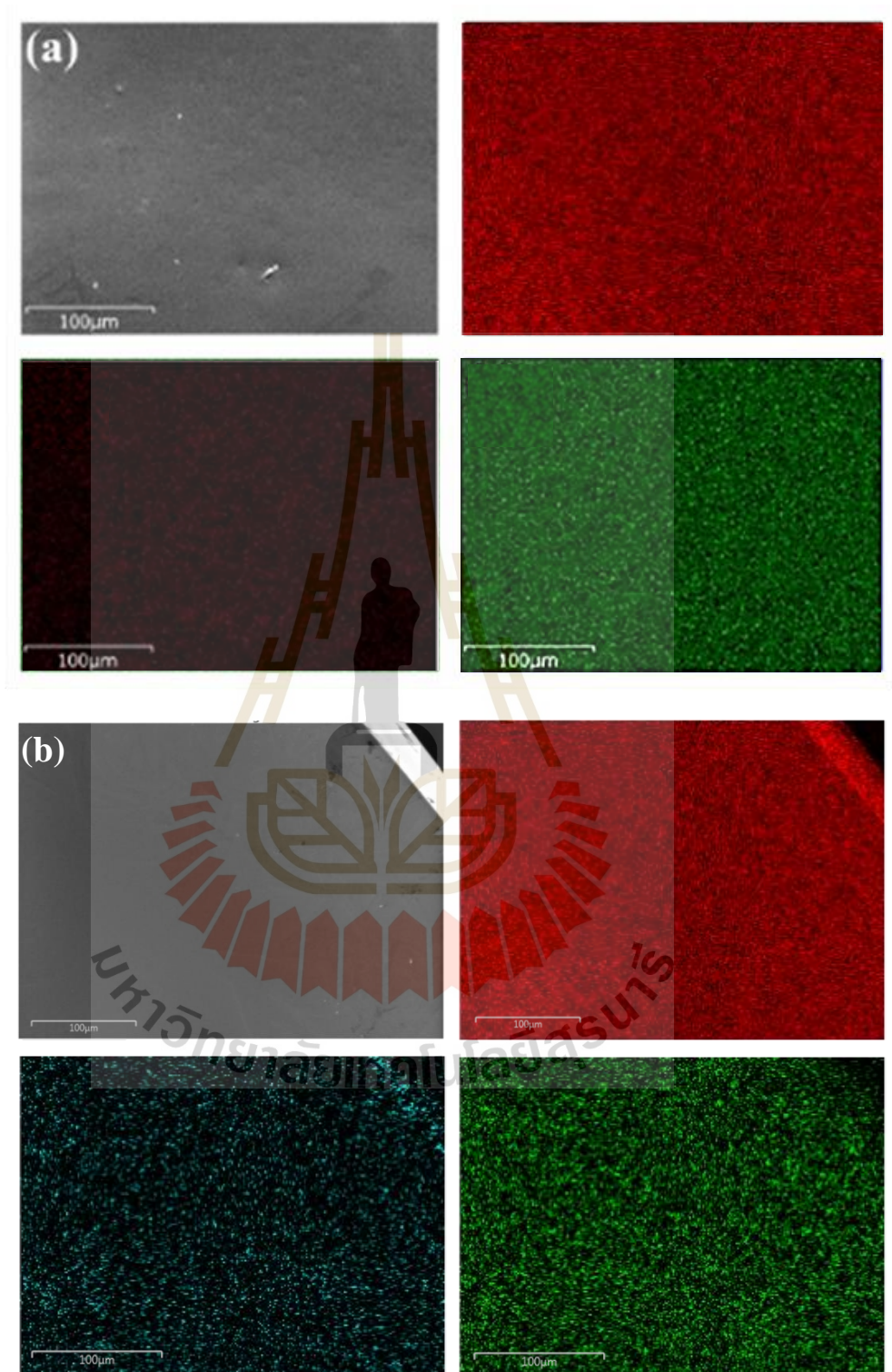
## 4.3 Scanning electron microscopy results

The SEM-EDS are used to determine the composition of the samples. In glasses samples, the EDS spectra identified manganese, boron, and oxygen concentrations. Elemental composition and elemental distribution are shown in Figure 4.5 and Table 4.1, respectively. Although no trace components of lithium were discovered, this

technique is incapable of detecting low-energy elements such as lithium. As can be seen in Figure 4.6, in regions selected in the research, color dots shown on the EDS maps are in accordance with the amounts of elements. As the boron level in the system grows, the amount of boron dot increases, further verifying the variance in the boron content in glass systems. Oxide-based glass samples have a high oxygen content, suggesting that shows the samples include oxides.



**Figure 4.5** EDS mapping of  $0.2\text{MnO}_2\text{-}0.8(1\text{Li}_2\text{O-}1\text{B}_2\text{O}_3)$  samples.



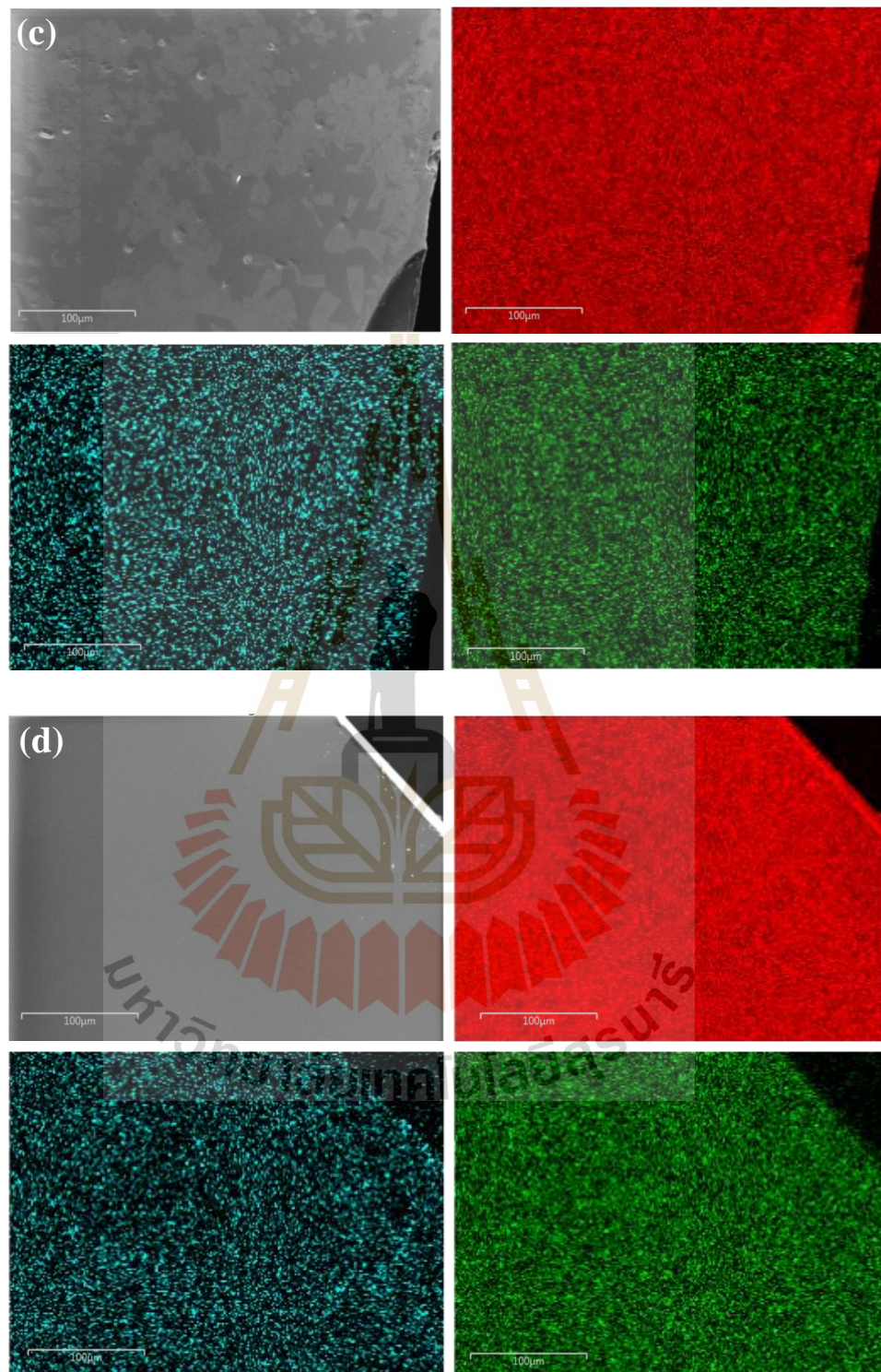


**Figure 4.6** SEM image of  $0.2\text{MnO}_2-0.8(1\text{Li}_2\text{O}-1\text{B}_2\text{O}_3)$  samples, (a) samples, (b) boron distribution, (c) manganese distribution and (d) oxygen distribution

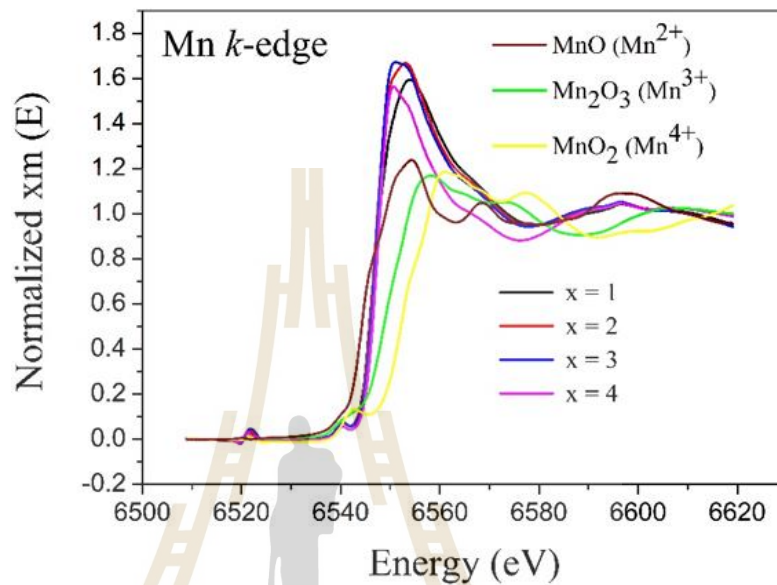
**Table 4.1** The percentage content of the glass sample with different compositions.

Samples	Element		
	Boron (%)	Manganese (%)	Oxygen (%)
0.2MnO <sub>2</sub> -0.8(1Li <sub>2</sub> O-1B <sub>2</sub> O <sub>3</sub> )	13.8	17.0	69.2
0.2MnO <sub>2</sub> -0.8(1Li <sub>2</sub> O- 2B <sub>2</sub> O <sub>3</sub> )	20.7	9.4	69.9
0.2MnO <sub>2</sub> -0.8(1Li <sub>2</sub> O- 3B <sub>2</sub> O <sub>3</sub> )	27.7	2.0	70.3
0.2MnO <sub>2</sub> -0.8(1Li <sub>2</sub> O- 4B <sub>2</sub> O <sub>3</sub> )	50.4	0.1	49.5

#### 4.4 X-ray absorption spectroscopy results

Normalized XANES spectra at the Mn *k*-edge of all samples are shown in Figure 4.7. The XANES spectra were compared with those of the standard samples i.e., MnO (Mn<sup>2+</sup>), Mn<sub>2</sub>O<sub>3</sub> (Mn<sup>3+</sup>) and MnO<sub>2</sub> (Mn<sup>+4</sup>). The adsorption edge at the Mn *k*-edge reported to be positioned between the adsorption edges of MnO and Mn<sub>2</sub>O<sub>3</sub> standards samples. This oxidation state of Mn<sup>2+</sup> and Mn<sup>3+</sup> in all glass samples is indicated. To better understand of the condition in which the Mn atom exists in glasses, EXAFS data is processed and fitted in the method shown in Figure 4.8 (a-d). The major peak at 1.70 Å (without phase shift adjustment, approximately 0.3 Å could be added) corresponds to the Mn-O bonding distance, and this peak was also used for fitting the first shell model. The bonding distance between Mn and O has been determined to be between 2.033 and 2.077 Å at Mn *k*-edge. The increase in boron content, or in other terms, the decrease in manganese concentration in the glass system, leads to an increase in the mean amount of oxygen atoms surrounding Mn ions. The important factors for

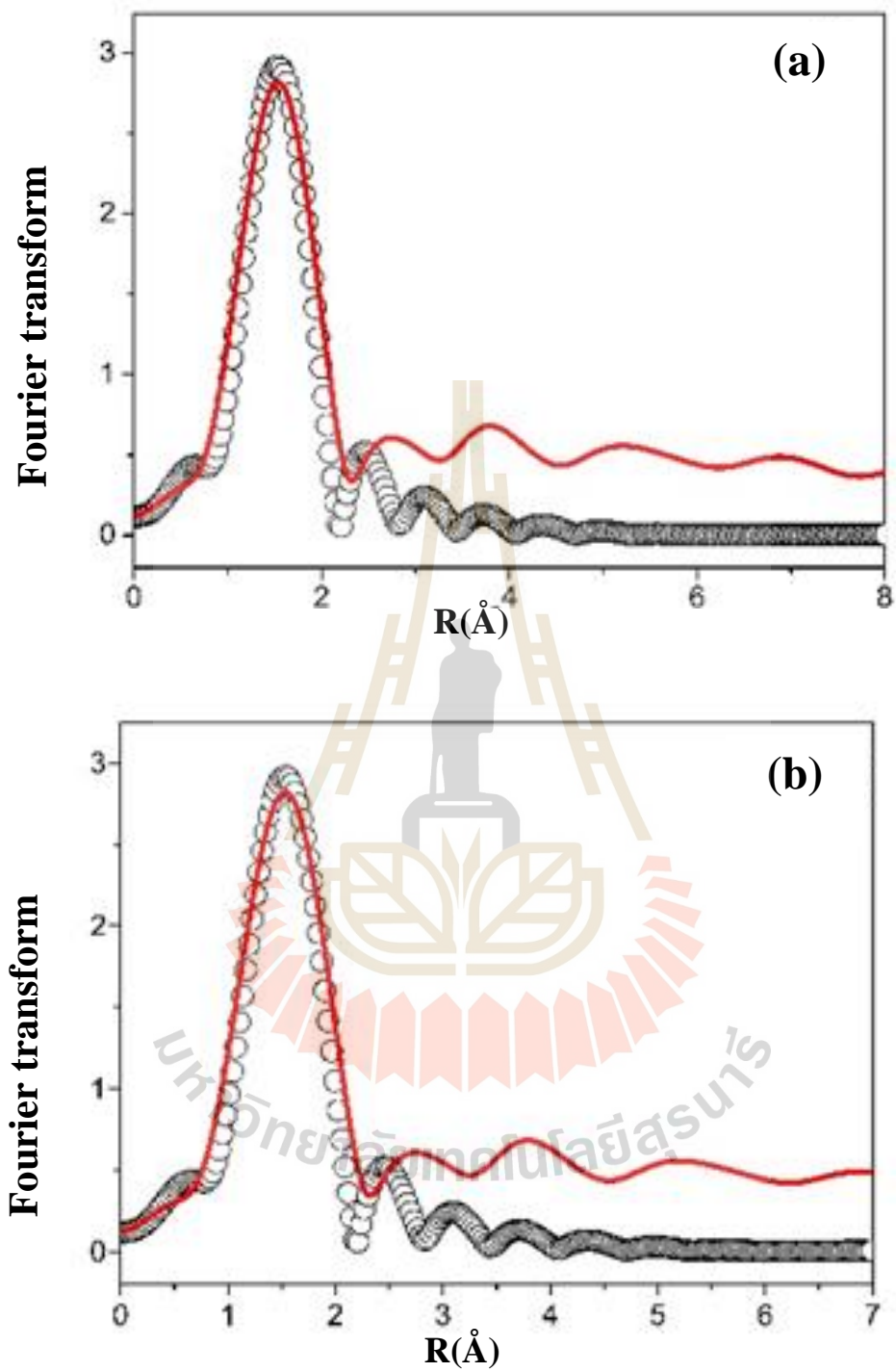
EXAFS fitting procedure are amplitude reduction ( $S_0^2$ ), model coordination number (N), Debye-Waller factors ( $\sigma^2$ ), edge energy ( $E_0$ ), Shift of bonding distance between atom ( $\Delta R$ ) and interatomic distances (R), as seen in Table 4.2



**Figure 4.7** XANES spectra of Mn *k*-edge of  $0.2\text{MnO}_2\text{-}0.8(1\text{Li}_2\text{O-}x\text{B}_2\text{O}_3)$  where  $x = 1, 2, 3,$  and  $4$  (mol%) glass samples and standard samples.

**Table 4.2.** EXAFS fitting parameter of  $0.2\text{MnO}_2\text{-}0.8(1\text{Li}_2\text{O-}x\text{B}_2\text{O}_3)$  where  $x = 1, 2, 3$  and  $4$  (mol%) glass samples.

Samples	Paths	$S_0^2$	N	$\sigma^2$	$E_0$	$\Delta R(\text{\AA})$	$R(\text{\AA})$
$0.20\text{Mn-}0.80(\text{Li}_2\text{O-}1\text{B}_2\text{O}_3)$	Mn-O	2.477	1	0.0078	-2.391	-0.0505	2.0495
$0.20\text{Mn-}0.80(\text{Li}_2\text{O-}2\text{B}_2\text{O}_3)$	Mn-O	2.782	1	0.0059	-5.318	-0.0589	2.0410
$0.20\text{Mn-}0.80(\text{Li}_2\text{O-}3\text{B}_2\text{O}_3)$	Mn-O	2.782	1	0.0079	-7.454	-0.0665	2.0335
$0.20\text{Mn-}0.80(\text{Li}_2\text{O-}4\text{B}_2\text{O}_3)$	Mn-O	3.057	1	0.0077	-6.168	-0.0227	2.0773



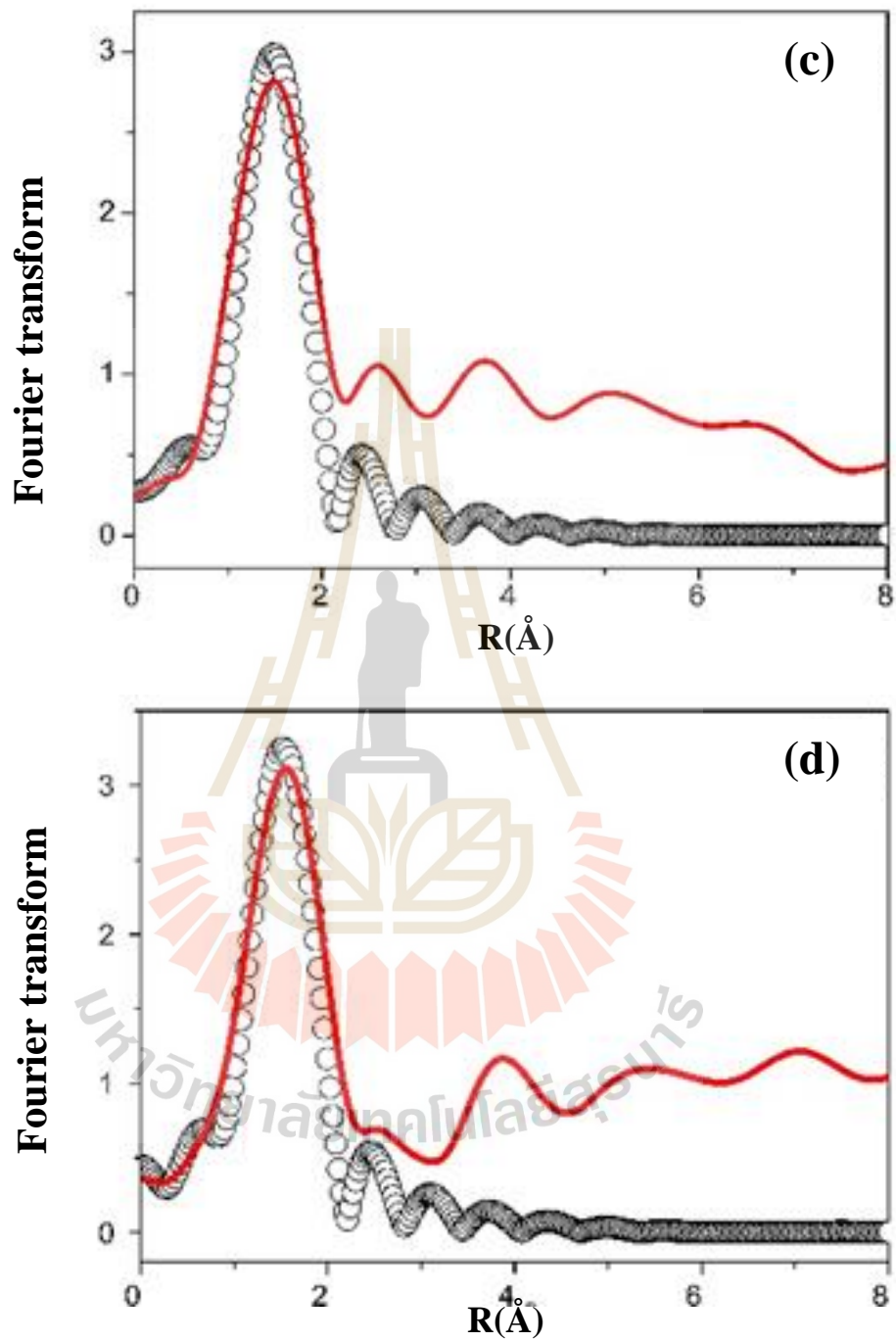


**Figure 4.8** Fourier transform plot at Mn  $k$ -edge from experiment (dot line) and fitting (solid line) of  $0.2\text{MnO}_2\text{-}0.8(1\text{Li}_2\text{O-xB}_2\text{O}_3)$  where  $x = 1, 2, 3,$  and  $4$  (mol%) glass samples.

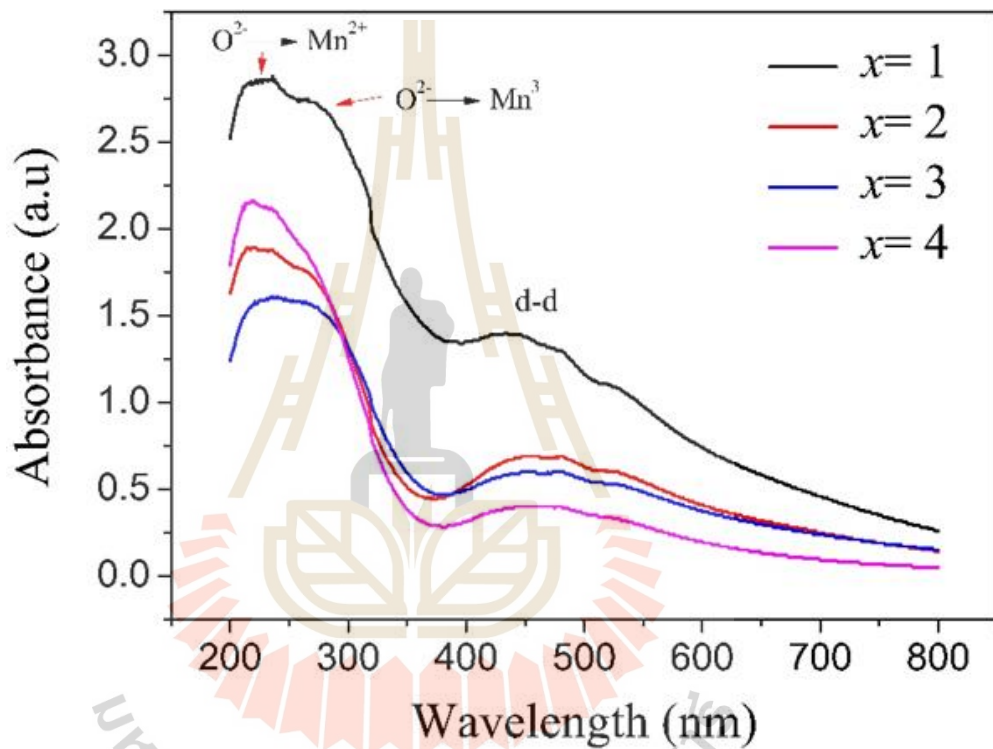
#### 4.5 UV-VIS spectrophotometer results

Optical absorption is determined by examining the spectra of glass samples at room temperature in the wavelength range 200-800 nm, as shown in Figure 4.9. The features of the spectra are characterized by comparable patterns. All the samples absorbed at the same rates, beginning between 200 and 280 nm and ending between 400 and 550 nm. According to the study on the charge transfer of  $\text{Mn}_3\text{O}_4$ , the  $\text{O}^{2-} \rightarrow \text{Mn}^{2+}$  and  $\text{O}^{2-} \rightarrow \text{Mn}^{3+}$  charge transfer transitions occur around 261 and 332 nm, respectively. (Bose et al., 2015; Raj et al., 2010; Macstre et al., 2001), d-d transition on octahedral  $\text{Mn}^{3+}$  type at 43 nm (Baldi et al., 1998; Valigi et al., 2015). Additionally, the energy band gap of each glass sample using equation (1) was calculated (Abdelghany et al., 2015).

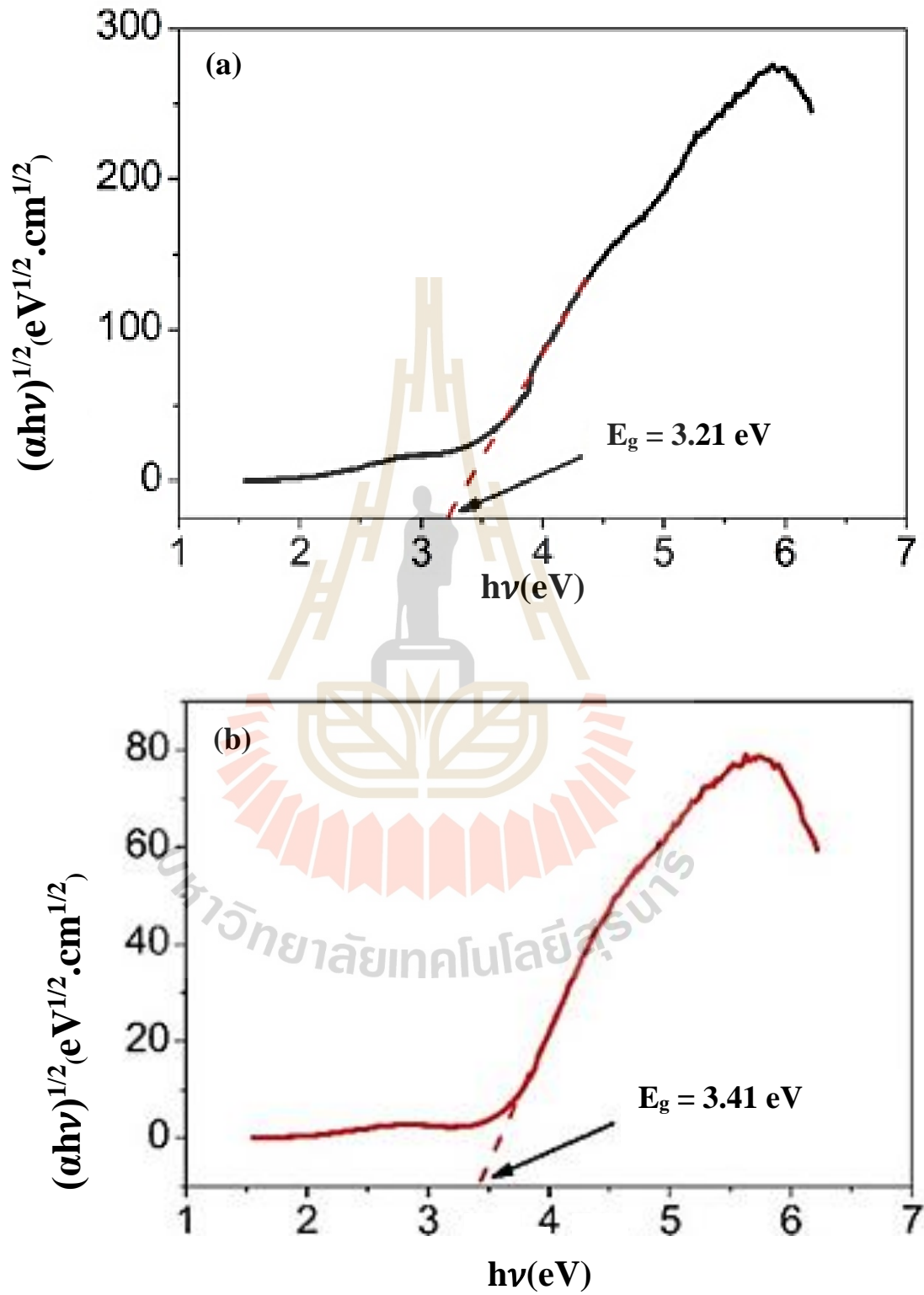
$$\alpha h\nu = A(h\nu - E_g)^2 \quad (12)$$

where  $\alpha$  is the absorption coefficient,  $h\nu$  is the incident photon energy,  $A$  is a constant and  $E_g$  is the optical band gap energy. The band gap was determined by extrapolating the linear portion of the Tauc plot of  $(\alpha h\nu)^2$  vs  $(h\nu)$  as shown in Figure 4.10 (a-d). For  $x = 1, 2, 3,$  and  $4$ , the energy band gap of all samples is 3.21, 3.41, 3.61, and 3.63 eV respectively. The energy gap differences are significantly increased with increased boron content in the glass samples. N. Laorodphan energy band gap experiments of vanadate-borate-based glasses found that the band gap decreased as the boron content increased, while the current analysis of manganate-borate-based glasses indicated that the band gap increased as the boron content increased. The influence of

manganese ions with combined manganese oxidation states of  $\text{Mn}^{2+}/\text{Mn}^{3+}$  could explain the differences in energy band gap trends (Laorodphan et al., 2016). The production of non-bridging oxygens can result in a change in the energy of the band gap. The structural change in the difference cite caused by cation occupancy is proportional to the change in band gap energy (Kaur et al., 2014).



**Figure 4.9.** Optical absorbance spectra of  $0.2\text{MnO}_2-0.8(1\text{Li}_2\text{O}-x\text{B}_2\text{O}_3)$  glasses samples: where  $x = 1, 2, 3$  and  $4$  (mol%).



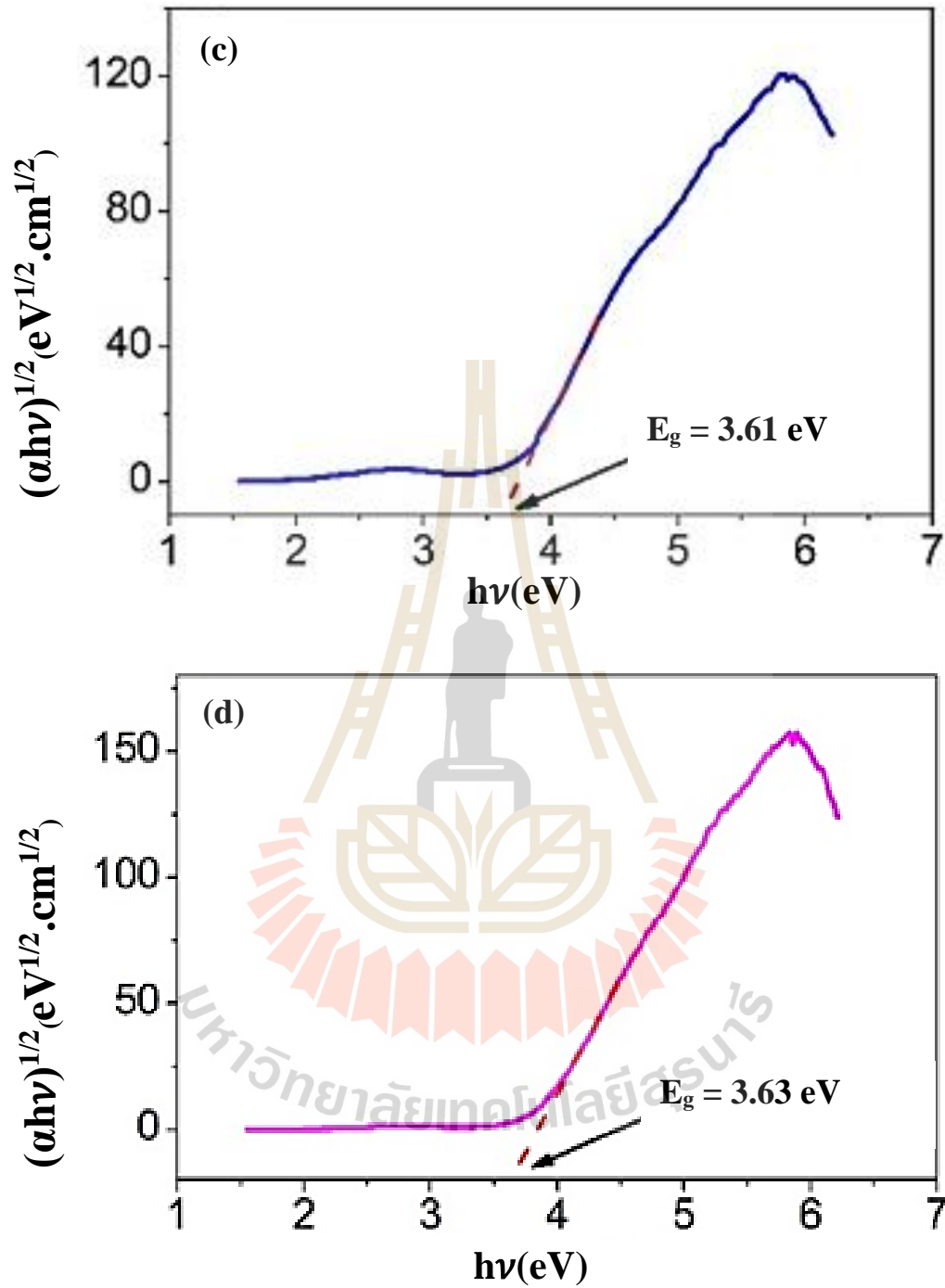


**Figure 4.10.** Plot of  $(\alpha h\nu)^{1/2}$  as function of photon energy ( $h\nu$ ) of  $0.2\text{MnO}_2\text{-}0.8(1\text{Li}_2\text{O-}x\text{B}_2\text{O}_3)$  glass samples: where (a)  $x = 1$ , (b)  $x = 2$ , (c)  $x = 3$  and (d)  $x = 4$  (mol%).

#### 4.6 Vibration sample magnetometer results

A representation of the magnetization characteristic of manganese- lithium borate glass samples is shown in Figure 4. 11. At room temperature, the glass samples exhibited paramagnetic activity, which is consistent with previous studies on Mn-doped glass ZnO (Phan et al., 2011). The maximum magnetism at 10,000 Oe is 0.256 emu/g for  $x = 1$  sample. Moreover, as the boron content in glasses samples increases, the magnetization decreases due to the diamagnetic behavior of borate- based glass. (Laorodphan et al., 2016). These effects are a consequence of the growing glassy phase, as shown by the XRD findings. The purpose of this investigation is to determine the impact of boron concentration on the magnetic characteristics of glasses. Because of the increase in boron concentration, a noticeable reduction in paramagnetic was detected, suggesting an increase in specific capacitance of the glasses that had been produced. The magnetism and electrochemical properties of these glasses suggest that they may be used as cathodes in energy storage applications, such as battery or supercapacitor cathodes.

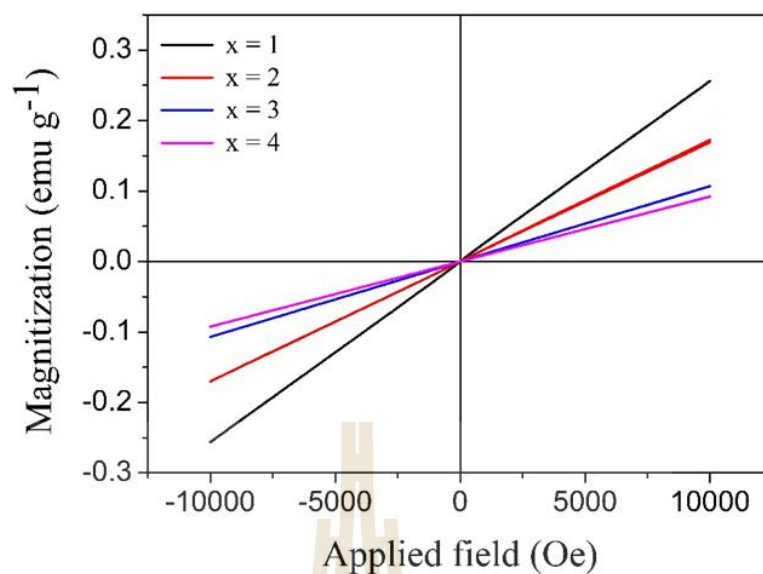


**Figure 4.11.** Magnetization hysteresis loop of  $0.2\text{MnO}_2\text{-}0.8(1\text{Li}_2\text{O-}x\text{B}_2\text{O}_3)$  where  $x = 1, 2, 3, 4$  (mol%) samples measured at room temperature

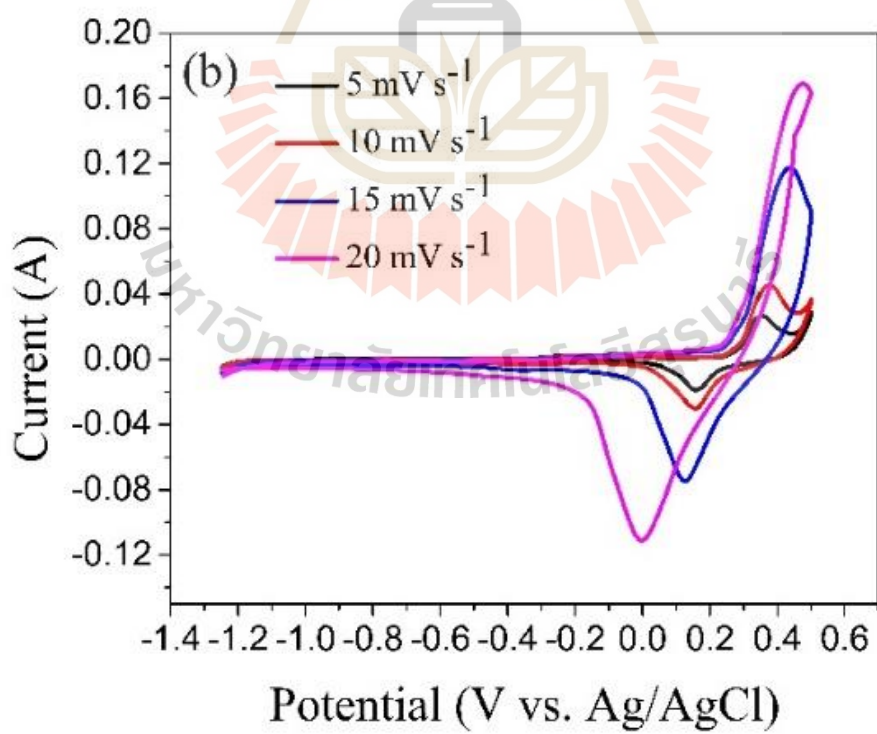
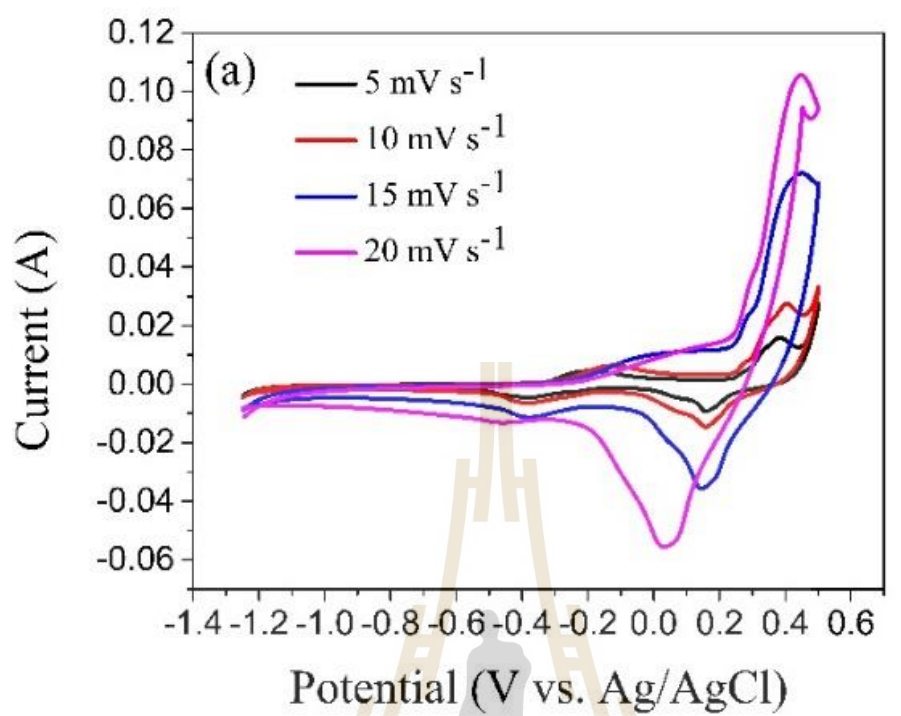
#### 4.7 Cyclic voltammetry results

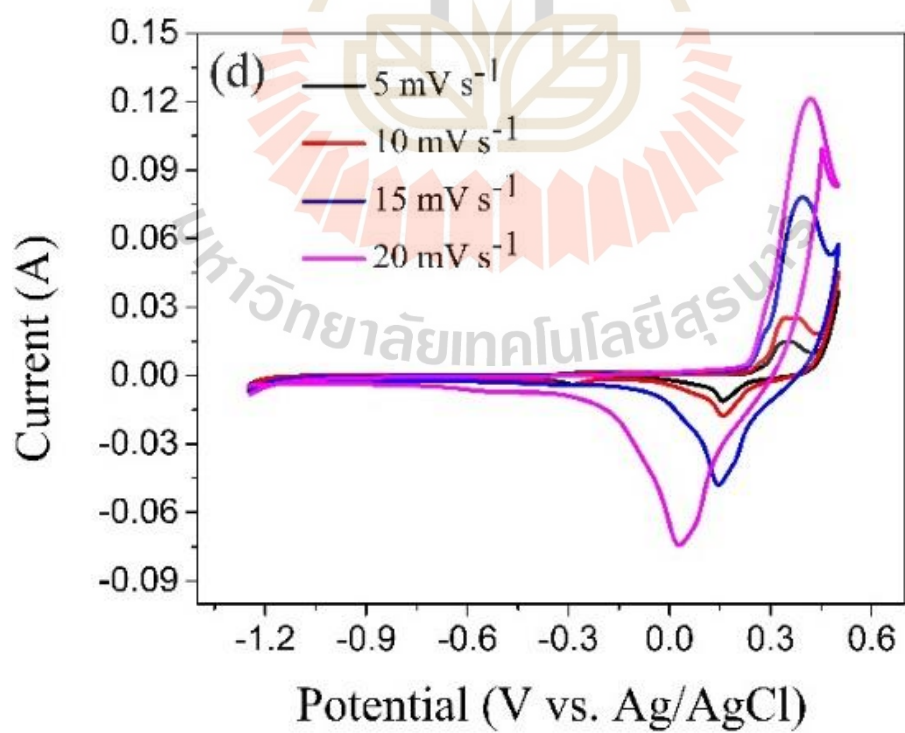
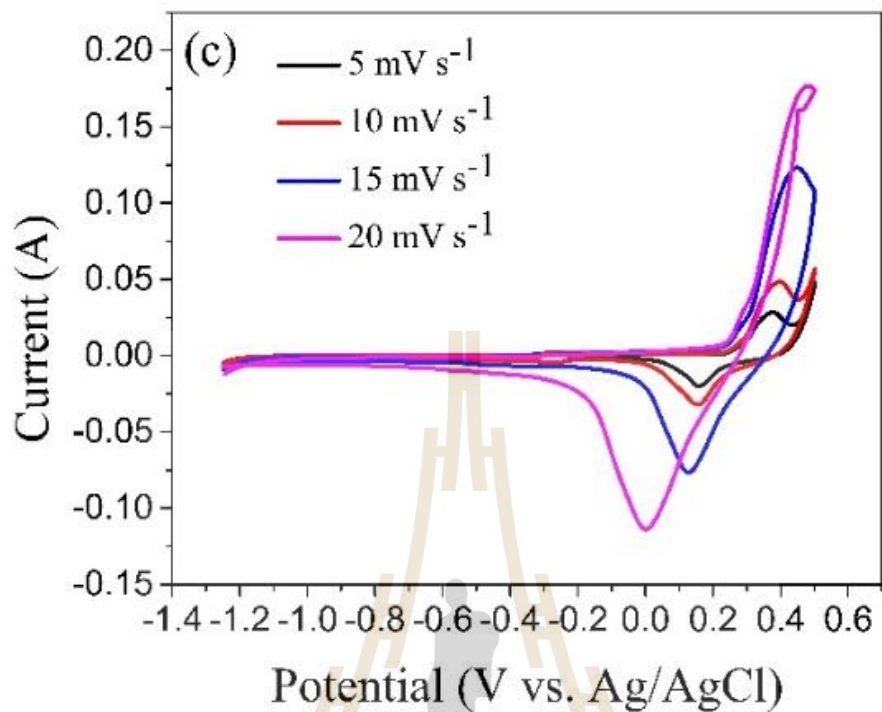
The CV curves of glass samples are shown in figure 4.12, in which the pseudo capacitive activity of charge and discharge peak were observed at potentials of 0.40-0.45 V and 0.02-0.18 V, respectively. That indicates the redox states which are electrochemically reversible during the reaction. The specific capacitance was calculated using the area of a CV curve with a variable scan rate. The following equation may be used to determine the relationship between specific capacitance and resistance:

$$C_{cv} = \frac{1}{vm\Delta V} \int IdV \quad (13)$$

where  $v$  is the scan rate ( $\text{mV s}^{-1}$ ),  $m$  is the mass of active materials(g),  $\Delta V$  is the potential window(V) and  $I$  is the response current(A) (Khanjonrit et al., 2018; Yan et al., 2012).

The area of the CV curve at different scan rates was used to determine the specific capacitance of the glass electrode materials, as shown in Figure 9 (e). The specific capacitance of  $0.2\text{MnO}_2\text{-}0.8(1\text{Li}_2\text{O-}x\text{B}_2\text{O}_3)$  increased from  $144 \text{ F g}^{-1}$  ( $x = 1$ ) to  $196 \text{ F/g}$  ( $x = 3$ ) and then decreased as boron content increased,  $121.54 \text{ Fg}^{-1}$ , ( $x = 4$ ) indicating that boron content has an impact on glass sample specific capacitance. Furthermore, the highest specific capacitance has been identified, which is significantly higher than the previous manganese lithium borate glass ( $187.05 \text{ Fg}^{-1}$ ) (Khanjonrit et al., 2018). However, when the scan rate increases, the specific capacitance values of the glass electrode decrease since the electrolyte ion may not have enough time to disperse deep through the pores of the materials (Mondal et al., 2016). This pattern can be seen in all structures. The higher redox reaction of Mn oxidation state has a high specific capacitance, as can be seen. However, because of the low scan rate, electrolyte ions may have enough time to reach the electrode surface pores, resulting in better ion transfer (Gupta et al., 2015).





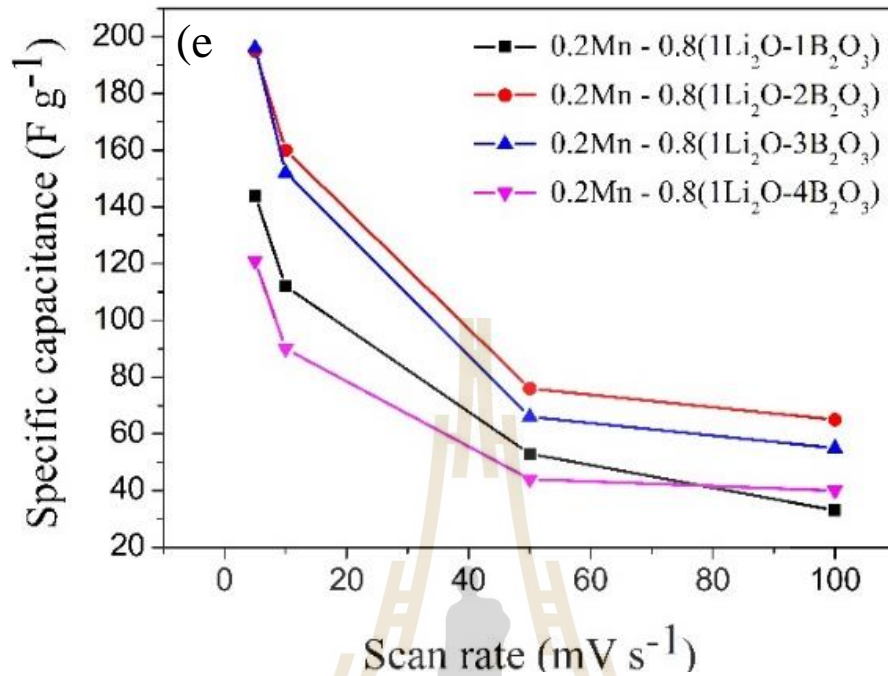


**Figure 4.12.** Cycle voltammograms of (a)  $0.2\text{MnO}_2\text{-}0.8(1\text{Li}_2\text{O-}1\text{B}_2\text{O}_3)$ , (b)  $0.2\text{MnO}_2\text{-}0.8(1\text{Li}_2\text{O-}2\text{B}_2\text{O}_3)$ , (c)  $0.2\text{MnO}_2\text{-}0.8(1\text{Li}_2\text{O-}3\text{B}_2\text{O}_3)$  and (d)  $0.2\text{MnO}_2\text{-}0.8(1\text{Li}_2\text{O-}4\text{B}_2\text{O}_3)$  glasses electrode at different scan rate (d) plot of specific capacitance versus scan rate.

## CHAPTER V

### CONCLUSION AND REMARKS

This thesis focused on the process of synthesizing manganese lithium borate glass and also on the structure characterized by using synchrotron based XAS. The process of glass synthesis was separated into two parts. First, the lithium borate glasses were successfully prepared with smoothly surface in transparency without color. After that, the manganese lithium borate glasses were successfully prepared with smoothly surface in transparency brown color (The  $0.2\text{Mn}-0.8(1\text{Li}_2\text{O}-1\text{B}_2\text{O}_3)$ ,  $0.2\text{Mn}-0.8(1\text{Li}_2\text{O}-2\text{B}_2\text{O}_3)$ ,  $0.2\text{Mn}-0.8(1\text{Li}_2\text{O}-3\text{B}_2\text{O}_3)$  and  $0.2\text{Mn}-0.8(1\text{Li}_2\text{O}-4\text{B}_2\text{O}_3)$ ) by using the typical melt-quench method.

The X-ray absorption spectroscopy (XAS) was used to study structure information and oxidation state of an interesting element. The SUT-NANOTECH-SLRI beamline was used to collect the data as mentioned previously. According to the XANES results, Mn in glass samples has a mixed oxidation state of  $\text{Mn}^{2+}$  and  $\text{Mn}^{3+}$ . The bonding distance in the range of 2.033-2.077 Å was determined by fitting the EXAFS spectra.

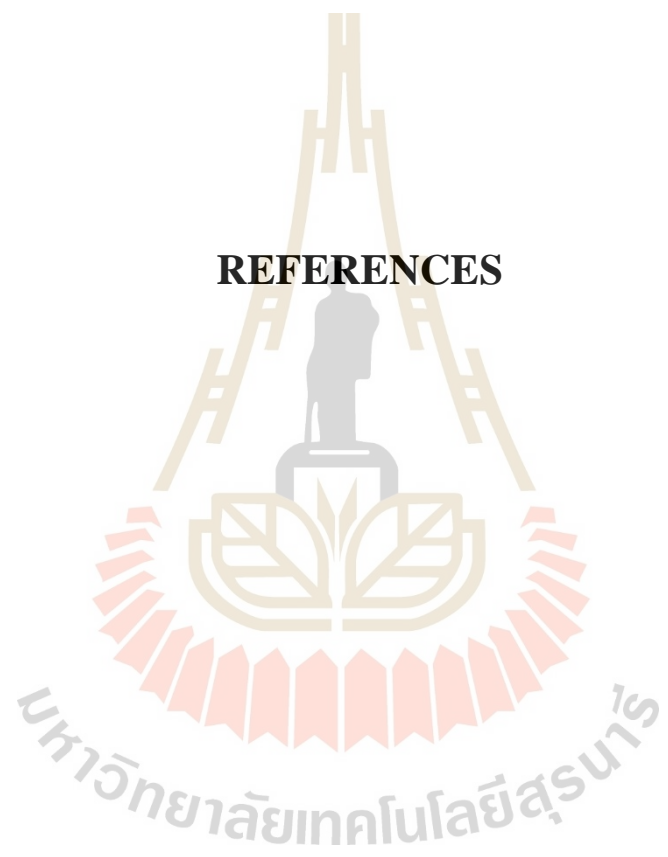
To the best of my knowledge, the oxidation state of an interesting element can be verified by the optical absorption properties. The glasses sample exhibit charge transfer of  $\text{Mn}^{2+}$  and  $\text{Mn}^{3+}$  occurring at 200- 280 nm and 400- 550 nm, respectively. The band gap energy can also be calculated and shown to increase in glass samples due to the increasing of boron content. The magnetic behavior of the glasses

sample was paramagnetic, with the  $0.2\text{MnO}_2\text{-}0.8(1\text{Li}_2\text{O-}1\text{B}_2\text{O}_3)$  sample having the maximum magnetism at 10,000 Oe of  $0.256\text{ emug}^{-1}$ . As a result, manganese lithium borate glass is a promising energy storage electrode material for applications such as supercapacitors and lithium batteries.

Furthermore, the mixing of oxidation state of  $\text{Mn}^{2+}$  and  $\text{Mn}^{3+}$  was interesting. More importantly, manganese oxide composed various oxidation states during the electrochemical cycling with the aqueous electrolyte system. The large capacitance ( $274\text{ F g}^{-1}$ ) exhibit when the higher of  $\text{Mn}^{2+}$  on  $\text{Mn}^{2+}/\text{Mn}^{3+}$  ratio. The large voltage window was around 2.0 V when combining with commercial activated carbon (the lithium fluorophosphate commercial coin cell battery exhibit around 1.8 V of voltage window) and high energy density. The cycle stability could keep about 92 % after 10,000 cycle tests. The process of controlling different  $\text{Mn}^{2+}/\text{Mn}^{3+}$  ratio as through over-reduction (OR).

For further investigations, the experimental to control the  $\text{Mn}^{2+}/\text{Mn}^{3+}$  ratio in lithium borate glasses shall be designed, and thus the effect of  $\text{Mn}^{2+}/\text{Mn}^{3+}$  ratio on the electrochemical properties shall be studied.

## REFERENCES



## REFERENCES

- Abdelghany, A., and Hammad, A. H. (2015). Impact of vanadium ions in barium borate glass. **Spectrochimica Acta Part A: Molecular and Biomolecular Spectroscopy**. 137.
- Afyon, S., Krumeich, F., Mensing, C., Borgschulte, A., and Nesper, R. (2014). New high capacity cathode materials for rechargeable Li-ion batteries: vanadate-borate glasses. **Scientific Reports**. 4.
- Andersson, M., Abraham, D. P., Haasch, R., MacLaren, S., Liu, J., and Amine, K. (2002). Surface characterization of electrodes from high power lithium-ion batteries. **Journal of the Electrochemical Society**. 149.
- Baldi, M., Milella, F., and Gallardo-Amore, J. M. (1998). A study of Mn-Ti oxide powders and their behavior in propane oxidation catalysis. **Journal of Materials Chemistry**. 8.
- Berkemeier, F., Shoar Abouzari, M., and Schmitz, G. (2017). Thickness dependent ion conductivity of lithium borate network glasses. **Applied Physics**. 90.
- Bose, V. C., and Biju, V. (2015). Optical, electrical and magnetic properties of nanostructured  $Mn_3O_4$  synthesized through a facile chemical route. **Physica E: Low-dimensional Systems and Nanostructures**. 66.

- Boyero, M. J., Fernandez, L. E., Gallardo-Amores, J. M., and Ruano, C. R. (2001). Influence of the synthesis parameters on the structural and textural properties of precipitated manganese oxide. **International Journal of Inorganic Materials**. 3.
- Gupta, R. K., Candler, J., Palchoudhury, S., Ramasamy, K., and Gupta, B. K. (2015). Flexible and High-Performance Supercapacitors Based on  $\text{NiCo}_2\text{O}_4$  for Wide Temperature Range Applications. **Scientific Reports**. 5.
- Karmakar, B. (2017). Functional glasses and glass-ceramics: processing, properties and applications, Butterworth-Heinemann.
- Kaur, M., Saini, M. S., Singh, D., and Mudahar, G. S. (2014). Synthesis and Characterization of Lithium Borate Glasses Containing Bismuth. **International Journal of Advanced Research in Physical Science**. 1.
- Khanjonrit, J., Wongpratrat, U., Kidkhunthod, P., Pinitsoontorn, S., and Maensiri, S. (2018). Effects of Co doping on magnetic and electrochemical properties of  $\text{BiFeO}_3$  nanoparticles. **Journal of Magnetism and Magnetic Materials**. 449.
- Kidkhunthod, P. (2017). Structural studies of advanced functional materials by synchrotron-based x-ray absorption spectroscopy: BL5.2 at SLRI, Thailand. **Advances in Natural Sciences: Nanoscience and Nanotechnology**. 8.
- Kim, J. C., Moore, C. J., Kang, B., Hautier, G., Jain, A., and Ceder, G. (2011). Synthesis and Electrochemical Properties of Monoclinic  $\text{LiMnBO}_3$  as a Li Intercalation Material. **Journal of The Electrochemical Society**. 158.
- Laorodphan, N., Pooddee, P., Kidkhunthod, P., Kunthadee, P., Tapala, W., and Puntharod, R. (2016). Boron and Pentavalent Vanadium Local Environments in Binary Vanadium Borate Glasses. **Journal of Non-Crystalline Solids**. 453.

- Legagneur, V., An, Y., Mosbah, A., Portal, R., La Salle, A. L., Verbaere, A., Guyomard, D., and Piffard, Y. (2001).  $\text{LiMBO}_3$  (M=Mn, Fe, Co): synthesis, crystal structure and lithium deinsertion/insertion properties. **Solid State Ionics**. 139.
- Lokhande, C., Dubal, D., and Loo, O. S. (2011). Metal oxide thin film-based supercapacitors. **Current Applied Physics**. 11.
- Mondal, R., Sahoo, S., and Rout, C. S. (2016). Mixed Nickel Cobalt Manganese Oxide Nanorods for Supercapacitor Application. **American Journal of Engineering and Applied science**. 9.
- Ozoemena, K. I., and Chen, S. (2016). Nanomaterials in Advanced Batteries and Supercapacitors, **Springer**.
- Phan, T. L., Zhang, P., Yang, D., Nghia, N., and Yu, S. (2011). Local structure and paramagnetic properties of  $\text{Zn}_{1-x}\text{Mn}_x\text{O}$ . **Journal of Applied Physics**. 110.
- Pye, L. D., Frechette, V. D., and Kreidl, N. J. (1978). Borate glasses: structure, properties and application, plenum press, New York.
- Qi, Z., Younis, A., Chu, D., and Li, S. (2016). Facile and template-free on e-pot synthesis  $\text{Mn}_3\text{O}_4$  nanostructures as electrochemical supercapacitors. **Nano-Micro Letters**. 8.
- Rao, V. M., Gopalakrishnan, R., Rao, V. V. R. N., Reddy, K. R., and Buddhudu, S. (1996). Physical investigation on lithium borate glasses for solid state battery applications. **Materials Science Forum**. 113.
- Raj, A. M. E., Vaictoria, S. G., Jothy, V. B., Ravidha, C., Wollschlager, J., Suen dorf, M., Neumann, M., Jayachandran, M., and Sanjeeviraja, C. (2010). XRD and XPS characterization of mixed valence  $\text{Mn}_3\text{O}_4$  hausmannite thin films prepared by chemical spray pyrolysis technique. **Applied Surface Science**. 256.

- Ragupathia, V., Srimathi, K., Puspamitra, P., Ganapathi, S., and Nagarajan, R. (2017). Spherical  $\text{LiZnBO}_3$ : Structural, optical and electrochemical properties. **Ionic**. 23.
- Ramteke, D. D., and Gedam, R. S. (2014). Study of  $\text{Li}_2\text{O-B}_2\text{O}_3\text{-Dy}_2\text{O}_3$  glasses by impedance Spectroscopy. **Solid state ionics**. 258.
- Stoch, S. (1999). Flexibility of Structure and Glass-Forming Ability: A Chemical Approach. **Glass Physics and Chemistry**. 27.
- Toupin, M., Brousse, T., and Belanger, D. (2014). Charge Storage Mechanism of  $\text{MnO}_2$  Electrode Used in Aqueous Electrochemical Capacitor. **Chem. Master**. 16.
- Valigi, M., and Cimino, A. (2015). The system  $\text{TiO}_2\text{MnO}_x$ : A structural, the thermogravimetric and magnetic study. **Journal of Solid State Chemistry**. 12.
- Yan, J., Liu, J., Fan, Z., Wei, T., and Zhang, L. (2012). High-performance supercapacitor electrodes based on highly corrugated graphene sheets. **Carbon**. 50.
- Yu, H., and Zhou, H. (2013). High-Energy Cathode Materials ( $\text{Li}_2\text{MnO}_3\text{-LiMO}_2$ ) for Lithium-Ion Batteries. **The Journal of Physical Chemistry Letters**. 4.
- Zhao, G., Zhang, N., and Sun, K. (2013). Porous  $\text{MoO}_3$  films with ultra-short relaxation time used for supercapacitors. **Materials Research Bulletin**. 48.

## APPENDIX

### Conference and presentation

**Amotntep Montreeuppathum**, Saroj Rujirawat, Rattikorn Yimnirun, Pinit Kidkhunthod. “Effect of borate glass network to electrochemical properties: Mn(II)-doped-lithium borate glasses” The ASIAN Conference on X-ray Absorption Spectroscopy 2019, Thailand.



Abstract submitted for the ASIAN Conference on X-ray Absorption Spectroscopy  
2019, Thailand

## **Effect of borate glass network to electrochemical properties: Mn(II)-doped-lithium borate glasses**

Amotntep Montreeuppathum<sup>1</sup>, Saroj Rujirawat<sup>1</sup>, Rattikorn Yimnirun<sup>2</sup> and Pinit Kidkhunthod<sup>3</sup>

<sup>1</sup> *School of Physics, Institute of Science, Suranaree University of Technology, Nakhon Ratchasima, 30000, Thailand*

<sup>2</sup> *School of Energy Science and Engineering, Vidyasirimedhi Institute of Science and Technology, Rayong, 21210, Thailand*

<sup>3</sup> *Synchrotron Light Research Institute (Public Organisation), Nakhon Ratchasima, 30000, Thailand*

*Email: [ballamorntep@gmail.com](mailto:ballamorntep@gmail.com)*

### **Abstract**

A development of manganese-lithium borate glasses for applications as supercapacitors was studied. The glasses were successfully prepared by melt quench technique and characterized by x-ray diffraction (XRD), scanning electron microscopy (SEM), and uv-visible spectroscopy (UV-VIS). The electrochemical property was studied by cyclic voltammetry and galvanostatic charge-discharge. Moreover, the advanced synchrotron-based x-ray absorption spectroscopy (XAS) was used to study a local structure and oxidation state of Mn content in the glasses. From the electrochemical properties of the electrode materials exhibited pseudo capacitive behavior with redox reaction of Mn<sup>2+</sup> and Mn<sup>3+</sup>. The highest specific capacitance is 197.5 F g<sup>-1</sup> for a cyclic voltammetry. The effect of Mn content can enhance the electrochemical performance.

## International publication

**Amornthep Montreeuppathum**, Pinit Kidkhunthod, Saroj Rujirawat, Rattikorn Yimmirun, Supree Pinitsoontorn, Santi Maensiri. “Effect of borate glass network to electrochemical properties: Manganese-doped lithium borate glasse”. **Radiation Physics and Chemistry**. Volume 170, May 2020, 108677.

Nattapol Laorodphan, Pinit Kidkhunthod, Jessada Khajonrit, **Amornthep Montreeuppathum**, Narong Chanlek, Supree Pinitsoontorn, Santi Maensiri. “Effect of B<sub>2</sub>O<sub>3</sub> content on structure-function of vanadium-lithium-borate glasses probed by synchrotron-based XAS and vibrating sample magnetometry technique”. **Journal of Non-Crystalline Solids**. Volume 497,1 October 2018, page 56-62.

Jessada Khajonrit, **Amornthep Montreeuppathum**, Pinit Kidkhunthod, Narong Chanlek, Yingyot Poo-arporn, Supree Pinitsoontorn, Santi Maensir. “New transparent materials for applications as supercapacitors: manganese-lithium-borate glasses”. **Journal of Alloys and Compounds**. Volume 763,30 September 2018, page 199-208.

## ARTICLE IN PRESS

Journal of Non-Crystalline Solids xxx (xxxx) xxx–xxx



Contents lists available at ScienceDirect

Journal of Non-Crystalline Solids

journal homepage: [www.elsevier.com/locate/jnoncrysol](http://www.elsevier.com/locate/jnoncrysol)

## Effect of B<sub>2</sub>O<sub>3</sub> content on structure-function of vanadium-lithium-borate glasses probed by synchrotron-based XAS and vibrating sample magnetometry technique

Nattapol Laorodphan<sup>a</sup>, Pinit Kidkhunthod<sup>b,\*</sup>, Jessada Khajonrit<sup>b</sup>, Amornthep Montreeuppathum<sup>b</sup>, Narong Chanlek<sup>b</sup>, Supree Pinitsoontorn<sup>c</sup>, Santi Maensiri<sup>d,e</sup>

<sup>a</sup> Department of Industrial Chemistry and Textile Technology, Faculty of Science, Maejo University, Chiang Mai 50290, Thailand

<sup>b</sup> Synchrotron Light Research Institute (Public Organisation), Nakhon Ratchasima 30000, Thailand

<sup>c</sup> Integrated Nanotechnology Research Center, Department of Physics, Faculty of Science, Khon Kaen University, Khon Kaen 40002, Thailand

<sup>d</sup> School of Physics, Institute of Science, Suranaree University of Technology, Nakhon Ratchasima 30000, Thailand

<sup>e</sup> NANOTEC-SUT Center of Excellence on Advanced Functional Nanomaterials, Suranaree University of Technology, Nakhon Ratchasima 30000, Thailand

## ARTICLE INFO

## Keywords:

Vanadium-lithium-borate glasses  
X-ray absorption spectroscopy  
X-ray photoelectron spectroscopy  
Vibrating sample magnetometry  
Paramagnetic behavior

## ABSTRACT

In this work, vanadium-lithium-borate glasses, 0.5V<sub>2</sub>O<sub>5</sub>–0.5(Li<sub>2</sub>O-xB<sub>2</sub>O<sub>3</sub>) with x = 1.0, 2.0 and 3.0, respectively, were prepared by conventional melt-quench technique. The glass samples were characterized by X-ray diffraction, scanning electron microscopy, X-ray absorption spectroscopy, X-ray photoelectron spectroscopy, UV-Visible Spectroscopy and vibrating sample magnetometry. X-ray absorption near-edge spectra at the V K-edge confirmed the presence of the mixing of V<sup>4+</sup> and V<sup>5+</sup> oxidation states and X-ray photoelectron spectroscopy were used to quantify and reveal the amount of V<sup>4+</sup> and V<sup>5+</sup> in the glass samples with approximately a ratio of 1:4 for V<sup>4+</sup>:V<sup>5+</sup>. The paramagnetic behavior were found for the glass samples with x = 1.0 and 2.0 due to the presence of V<sup>4+</sup>. However, an influence of B<sub>2</sub>O<sub>3</sub> content clearly affected to the glass sample with x = 3.0 resulting to a diamagnetic nature of this glass composition. The local structural information around V atoms in all glass samples were addressed using extended X-ray absorption fine structure technique with a mean oxygen coordinated network of 3.50(1). The notable properties of these glasses can be used and applied in the energy storage applications.

## 1. Introduction

Owing to the various oxidation states of vanadium [1,2], vanadium-based glasses are attractive as promising novel materials in many applications such as cathode in Li-ion batteries [3]. Vanadium based-electrodes have been synthesized by various methods with different starting materials e.g. glass formers [4–6]. For example, V<sub>2</sub>O<sub>5</sub>-P<sub>2</sub>O<sub>5</sub> glass cathodes reported by Sakurai et al. [4–6] demonstrated a drop of the capacity on the first charge (to 350 mAh/g) and cycling properties are not very remarkable for the large potential window.

Generally, one of good glass formers which has been broadly used in many glass-based materials is boron oxide (B<sub>2</sub>O<sub>3</sub>). Especially in borate-vanadate based glasses with binary, ternary and quaternary glass systems, there have been studied varieties both physical and electrical and electrochemical properties [7–13]. Recently, there has been a report on structure of binary vanadium borate glasses [13]. The V-structure was reported by XAS technique with a mean V oxidation state [13].

However, to the best of our knowledge, their deep information concerning the local structure information around vanadium ions which leads them to the notable properties have not been clearly studied and understood.

In this research work, the vanadium-lithium borate glass systems, V<sub>2</sub>O<sub>5</sub>-LiBO<sub>2</sub> have been introduced with both structural and physical such as scanning electron microscopy, X-ray photoelectron spectroscopy (XPS), UV-Vis and vibrational sample magnetometry. A very simply synthesis method using furnace melting has been used to synthesize these glasses. Furthermore, the synchrotron-based X-ray absorption spectroscopy (XAS) techniques including X-ray absorption near edge structure (XANES) and extended X-ray absorption fine structure (EXAFS) has been employed to these glasses in order to deeply address the existence of many vanadium oxidation states and local structural information around vanadium atoms in these such prepared glasses.

\* Corresponding author.

E-mail address: [pinit@slri.or.th](mailto:pinit@slri.or.th) (P. Kidkhunthod).

<https://doi.org/10.1016/j.jnoncrysol.2018.04.045>

Received 18 January 2018; Received in revised form 18 April 2018; Accepted 25 April 2018  
0022-3093/ © 2018 Elsevier B.V. All rights reserved.

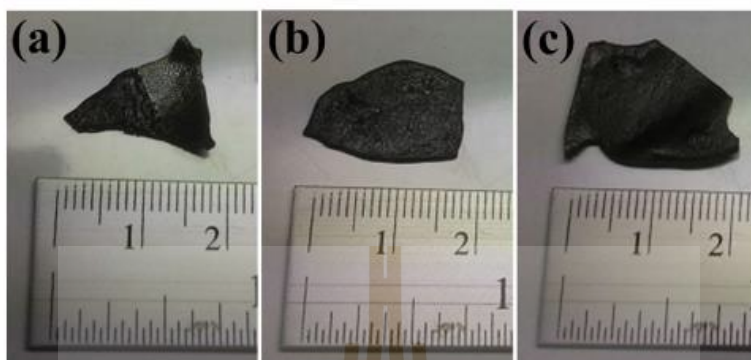


Fig. 1. Feature of  $0.5V_2O_5-0.5(Li_2O-xB_2O_3)$  glass samples: (a)  $x = 1$ , (b)  $x = 2$ , (c)  $x = 3$ .

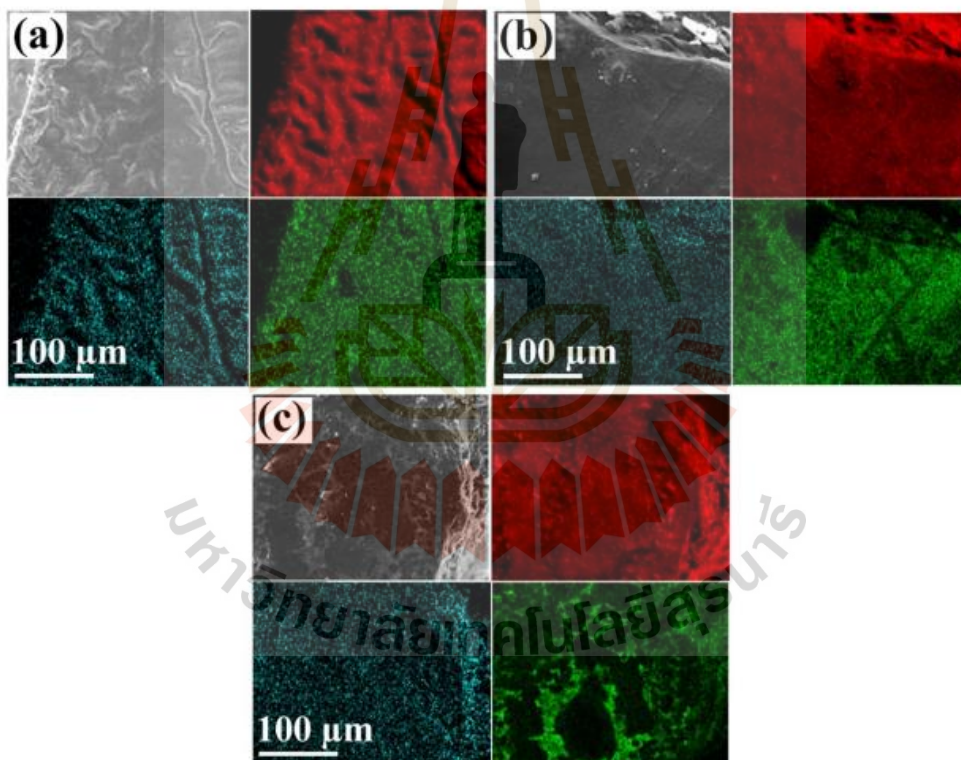


Fig. 2. SEM images and EDS mapping of  $0.5V_2O_5-0.5(Li_2O-xB_2O_3)$  glass samples: (a)  $x = 1$ , (b)  $x = 2$ , (c)  $x = 3$  (samples-grey; O-red; B-blue; and V-green). (For interpretation of the references to color in this figure legend, the reader is referred to the web version of this article.)

**Table 1**  
Density and molar volume of the vanadium-lithium borate glasses.

$0.5V_2O_5-0.5(Li_2O-xB_2O_3)$ Samples	Density ( $g/cm^3$ )	Molar volume ( $cm^3/mol$ )
$x = 1$	$2.72 \pm 0.22$	51.64
$x = 2$	$2.25 \pm 0.35$	78.07
$x = 3$	$2.36 \pm 0.01$	89.12

## 2. Experimental procedures

### 2.1. Sample preparation

The conventional melt-quench method was used to prepare vanadium-lithium borate glass,  $0.5V_2O_5-0.5(Li_2O-xB_2O_3)$  glass with  $x = 1, 2$  and 3 glass, which divided into two steps. The first step is lithium borate preparation. The lithium borate were prepared by mixing of the precursor materials of Lithium carbonate ( $Li_2CO_3$ , 99%, Himedia) and

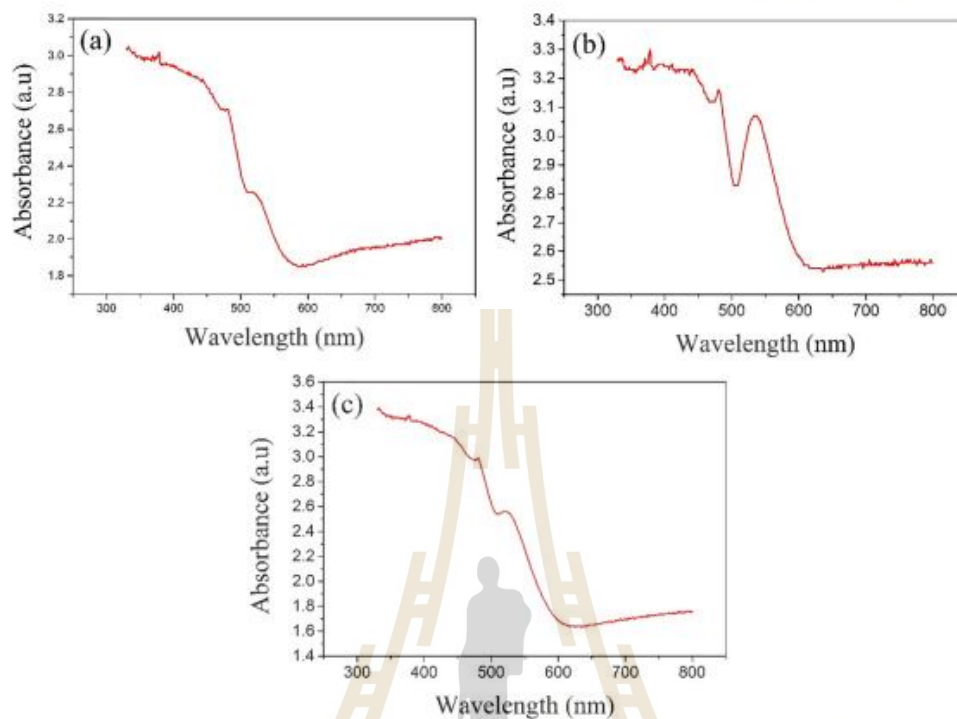


Fig. 3. Optical absorbance spectra of  $0.5V_2O_5-0.5(Li_2O-xB_2O_3)$  glass samples: (a)  $x = 1$ , (b)  $x = 2$ , (c)  $x = 3$ .

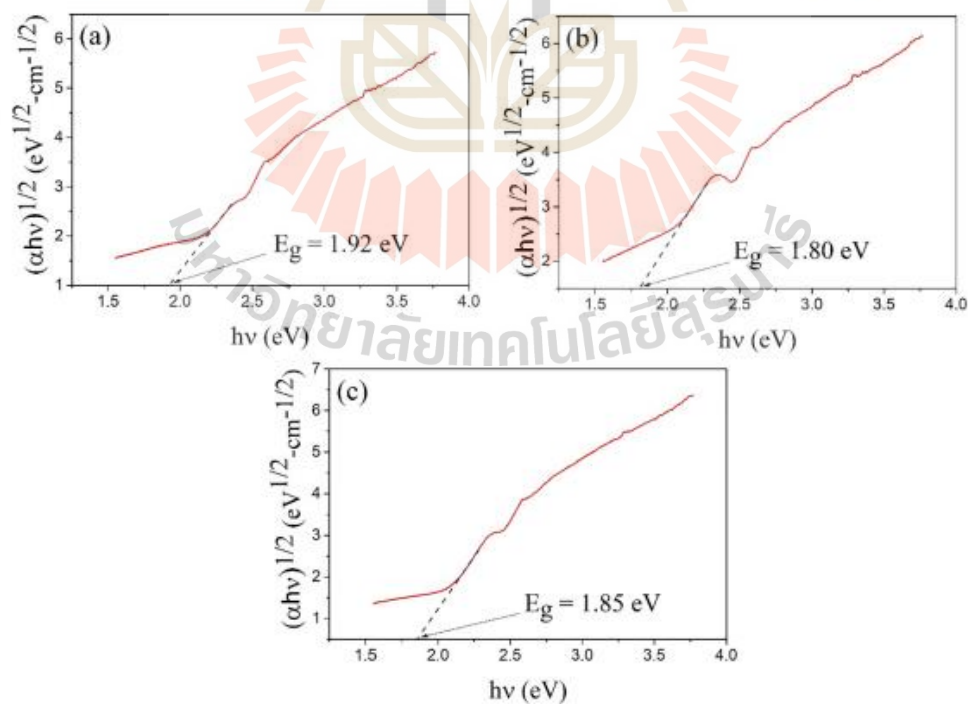


Fig. 4. Plot of  $(\alpha hv)^{1/2}$  as function of photon energy ( $h\nu$ ) of  $0.5V_2O_5-0.5(Li_2O-xB_2O_3)$  glass samples: (a)  $x = 1$ , (b)  $x = 2$ , (c)  $x = 3$ .

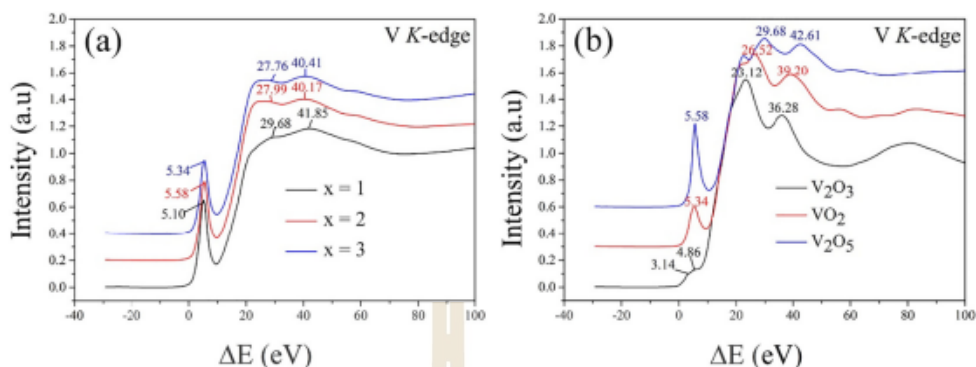


Fig. 5. XANES spectra of (a) V K-edge of  $0.5V_2O_5-0.5(Li_2O-xB_2O_3)$  glass samples (b) V K-edge of the standard materials.

Boric Acid ( $H_3BO_3$ , 99.8%, Himedia) in agate mortar. The mixtures in the platinum crucibles were calcined at  $1100^\circ C$  for 1 h. The liquid melt glass is extremely rapid cooled to room temperature by stainless plates. The second step is vanadium-lithium borate glass preparation. The lithium borate samples were ground into powder form and were mixed with vanadium (V) oxide ( $V_2O_5$ , 99.6%, Sigma-Aldrich) in agate mortar. Then, the mixtures were calcined at  $1150^\circ C$  for 1 h. The melts were poured and pressed on stainless plate and were then cooled to room temperature with extremely rapid quenching.

## 2.2. Characterizations

The Microstructural observation was performed by using a scanning electron microscope (FEI-Quanta 450). The density of all vanadium-lithium borate samples ( $\rho_{sample}$ ) are investigated by comparison of weights of samples in air and in liquid (xylene). The density was obtained by using the relation [13]:

$$\rho_{sample} = \frac{W_{air}}{(W_{air} - W_{xylene})} (\rho_{xylene}) \quad (1)$$

where  $\rho_{sample}$  is the density of the sample,  $\rho_{liquid}$  is the density of xylene,  $W_{air}$  is the weight of glass sample in air, and  $W_{xylene}$  is the weight of glass sample in xylene.

The molar volume of all glass samples ( $V_m$ ) were calculated by using these molecular weights and density, which can be calculated from following Eq. [13]:

$$V_m = \frac{M_w}{\rho_{sample}} \quad (2)$$

where  $V_m$  is molar volume,  $\rho_{sample}$  is the density of the sample and  $M_w$  is the molecular weight of the sample.

Optical absorption spectra of all glass samples were recorded at room temperature in the range 350–800 nm by PerkinElmer-Lambda 950 spectrophotometer. Synchrotron-based XANES and EXAFS spectra were conducted at the SUT-NANOTEC-SLRI XAS Beamline (BL5.2) at the Synchrotron Light Research Institute (Public Organization), Thailand [14,15]. To characterize the valence states and local structural information of V atoms, the XAS including XANES and EXAFS spectra at V K-edge spectra were collected in the transmission modes. The XPS spectra was measured from a PHI 5000 Versa Probe II XPS system (ULVAC-PHI, Japan). The magnetic measurements were studied using a vibrating sample magnetometer (VSM) option in the Quantum Design Versalab instrument. The magnetization were collected in a magnetic field range of  $\pm 10$  kOe at room temperature.

## 3. Results and discussion

### 3.1. Characterizations

Fig. 1 shows the prepared vanadium-lithium borate glass samples with different compositions. All prepared glasses after calcination showed dense and smooth surface structure with black color. The nature of amorphous phase was ensured using X-ray diffraction with observed diffraction peak as seen in S.1. The morphology of the prepared  $0.5V_2O_5-0.5(Li_2O-xB_2O_3)$  glass samples was investigated by SEM. All samples exhibited the platelet structure typically of glass materials. The elemental mapping images of oxygen, boron and vanadium in all samples were measured by SEM-EDS as shown in Fig. 2, which indicated that oxygen, boron and vanadium were uniformly distributed. This implies that the glass composition reaction was occurred in full body of samples.

Glass densities were calculated as shown in Table 1 and found that the density of the vanadium-lithium borate glass ( $0.5V_2O_5-0.5(Li_2O-xB_2O_3)$ ) decrease with increasing of  $B_2O_3$  content from  $2.72 \pm 0.22$  g/cm<sup>3</sup> to  $2.25 \pm 0.35$  g/cm<sup>3</sup> for  $x = 1.0$  and  $x = 2.0$ , respectively. Then, the density slightly increase to  $2.36 \pm 0.01$  g/cm<sup>3</sup> for  $x = 3.0$ . This corresponds to the density of the vanadium borate glass, which increases as  $V_2O_5$  content increase [13]. Moreover, the calculated molar volume of the glass samples is  $51.64$  cm<sup>3</sup>/mol,  $78.07$  cm<sup>3</sup>/mol and  $89.12$  cm<sup>3</sup>/mol for  $x = 1, 2$  and  $3$  sample, respectively. This increasing of molar volume with increasing of  $B_2O_3$  content may due to large borate frameworks as occurring in phosphorus borate glasses [16].

### 3.2. Optical properties

The UV-Vis absorption spectra of the vanadium-lithium borate glass samples recorded in the wavelength region in the range of 330–800 nm are shown in Fig. 3. Generally, for vanadium in glasses, the charge transfer of  $V^{5+}$  and the d-d transition of  $V^{4+}$  are located at the wavelength 200–377 nm [10] and 534 nm [17], respectively. Therefore, the UV bands in this work about 350–370 nm can be related to the presence of  $V^{5+}$  ions in all samples. The extended UV-visible bands attributed to the presence of tetravalent vanadium ( $V^{4+}$ ) in the vanadium containing glass samples [18]. Therefore, the absorption edge observed between 520 and 540 nm in this work indicated presence of valence state  $V^{4+}$  in the glass samples. The absorption bands at 520–540 nm corresponding to  ${}^2B_{2g} \rightarrow {}^2B_{1g}$  transition indicate the possible presence of the tetravalent vanadyl ( $VO^{2+}$ ) ions [17]. With increasing of  $B_2O_3$  content, the absorption bands of  $x = 2$  sample shifted to higher wavelength side than  $x = 3.0$  and  $x = 1.0$ , respectively. This shift of the absorption bands in these related to the presence and amount of  $V^{4+}$  in the samples confirmed by XPS results. Generally, the glass forming anions play an indirect band transition [18–20]. In order to calculate the energy

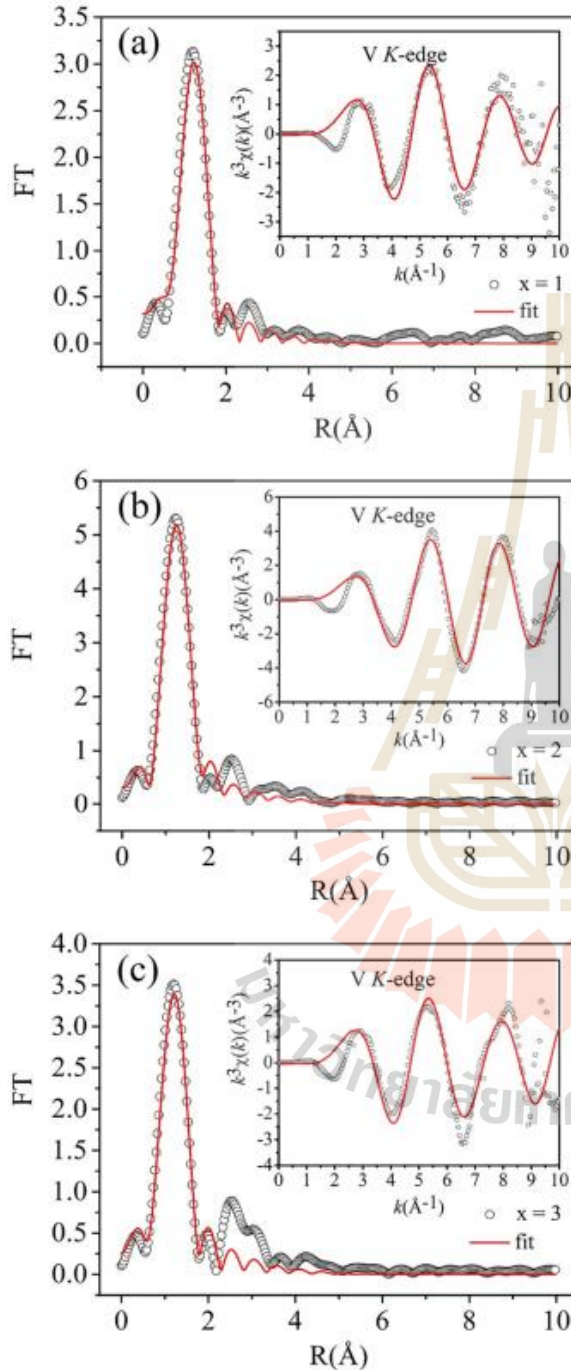


Fig. 6. Fourier transform and  $k^2\chi(k)$  plots at V K-edge from experiment (solid line) and fitting (dot line) of  $0.5V_2O_5-0.5(Li_2O-xB_2O_3)$  glass samples: (a)  $x = 1$ , (b)  $x = 2$ , (c)  $x = 3$ .

band gap, the energy band gap of the glass samples was obtained by using the relation [18]:

$$\alpha h\nu = A(h\nu - E_g)^2 \quad (3)$$

where  $\alpha$  is the absorption coefficient,  $h$  is the Planck constant,  $\nu$  is the wavenumber,  $A$  is a constant and  $E_g$  is the optical band gap energy for indirect band gap.

Fig. 4 illustrates the Urbach plots of all these glasses. The energy gap of the glass samples is 1.92 eV, 1.80 eV, 1.85 eV for  $x = 1.0, 2.0$  and  $3.0$ , respectively. The decreasing of the tendency of energy gap and the shift of toward slightly higher wavelength of absorption bands at 520–540 nm, which attributed to the increasing of vanadyl cations of  $V^{4+}$  content in the glass sample, which cause polaronic development due to excited states of electrons trapped on  $V^{4+}$  begin to overlap with the empty 3d states on the neighboring  $V^{5+}$ . This might have shifted the absorption edge to the lower energy reported by Srilatha et al. [21].

### 3.3. Structural studies using XANES and EXAFS

Fig. 5 shows normalized XANES spectra at the V K-edge of the  $0.5V_2O_5-0.5(Li_2O-xB_2O_3)$  ( $x = 1.0, 2.0, 3.0$ ) glass samples comparing with the  $V_2O_3$  ( $V^{3+}$ ),  $VO_2$  ( $V^{4+}$ ) and  $V_2O_5$  ( $V^{5+}$ ) standard samples. The increasing of  $B_2O_3$  content leads to shift of the pre-edge peaks (5.10, 5.58 and 5.34 eV), white line peaks (29.68, 27.99 and 27.76 eV) and after absorption edge peaks (41.85, 40.17 and 40.41 eV) for  $x = 1.0, 2.0$  and  $3.0$ , respectively. The energy positions of pre-edge, white line and after absorption edge peaks in all samples match with the energy positions of the  $VO_2$  and  $V_2O_5$ . Moreover, for comparison, the XANES spectra in this work is similar to the results presented by Wong et al. [22]. The energy position of pre-edge peaks, white line peaks and after absorption edge peaks of V K-edge XANES spectra are 5.4, 26.2 and 39.8 eV for  $VO_2$  and 5.6, 30.1 and 43.1 eV for  $V_2O_5$ , respectively. Clearly, the oxidation states of V of all samples are between  $4+$  and  $5+$ . In this work, XANES analysis used to confirm the mixing oxidation state of V in the samples. The quantitative analysis of V in the samples was investigated in the latter part of XPS.

Furthermore, in order to understand the environment of V atoms in the glass structure, the EXAFS data were carefully analyzed and fitted. The  $k^2\chi(k)$  EXAFS spectra and their corresponding fourier transform in R space ( $k = 3-9 \text{ \AA}^{-1}$ ) at V K-edge of all samples are shown in Fig. 6. The profiles at V K-edge of all samples are similar. This implies these local environment surrounding vanadium atoms are identical. The EXAFS fitting of this glasses was carefully done using the different V-O bonding distance model (5-fold coordinated network with V-O1, 2[V-O2], V-O3 and V-O4 distances) was used for the first shell fit as seen in Table 2. The parameters of the best fitting such as interatomic distances (R), model coordination numbers (N), Debye-Waller factors ( $\sigma^2$ ) and amplitude reduction ( $S_0^2$ ) were shown in the Table 2. In this study, the existence of oxygen coordination number around vanadium atoms could be obtained by  $N \times S_0^2$ . In more detail, when the Boron content increase, the mean bonding distance between V-O also slightly increase.

### 3.4. X-ray photoelectron spectroscopy

The XPS spectra in the glass samples are shown in Fig. 7. The XPS spectra showed the peaks associated with the presence of  $V^{5+}$  and  $V^{4+}$  in the glass samples. The amount of  $V^{4+}/V^{5+}$  calculated are 12.34/87.66%, 19.47/80.52% and 18.82/81.19% for  $0.5V_2O_5-0.5(Li_2O-xB_2O_3)$  with  $x = 1.0, 2.0$  and  $3.0$ , respectively. The presence of lithium ions moving around the glass structure can influence to oxidation state of the vanadium ion. This suggest that increasing of amount of  $V^{4+}$  attributed to the decreasing ratio of Li (with positive charge) ions content compared with B ions with increasing of the  $x$  values in the glass structure. However, the ratio of the  $V^{4+}/V^{5+}$  at  $x = 0.2$  to  $0.3$  are saturate, which is confirm by the XPS technique. The presence of  $V^{4+}$  in the samples may influence to magnetic properties in the glass samples, which discussed in the part of magnetic properties.

**Table 2**  
EXAFS fitting parameters including interatomic distances (R), coordination numbers (N), Debye–Waller factors ( $\sigma$ ) amplitude reduction ( $S_0^2$ ) and R-factor of  $0.5V_2O_5-0.5(Li_2O-xB_2O_3)$  ( $x = 1, 2, 3$ ) glass.

Samples	Paths	N	$S_0^2$	$\sigma^2$	$E_0$ (eV)	R (Å)	R-factor
1Li-1B	V-O1	1	0.750	0.00300	-8.289	1.61295	0.02302
	V-O2	2	0.750	0.00350	-8.289	1.76182	
	V-O3	1	0.750	0.00380	-8.289	2.04221	
	V-O4	1	0.750	0.00440	-8.289	2.26950	
1Li-2B	V-O1	1	0.700	0.00280	-6.554	1.63371	0.01329
	V-O2	2	0.700	0.00300	-6.554	1.75357	
	V-O3	1	0.700	0.00335	-6.554	2.00923	
	V-O4	1	0.700	0.00380	-6.554	2.26476	
1Li-3B	V-O1	1	0.750	0.00280	-7.021	1.73324	0.03230
	V-O2	2	0.750	0.00320	-7.021	1.70069	
	V-O3	1	0.750	0.00380	-7.021	2.01942	
	V-O4	1	0.750	0.00380	-7.021	2.21965	

### 3.5. Magnetic properties

The room temperature M-H loop of the glass samples are shown in Fig. 8. For the  $0.5V_2O_5-0.5(Li_2O-xB_2O_3)$  with  $x = 1.0$  and  $2.0$  samples, the magnetization depend on linearly on the applied field, which indicated the paramagnetic. The increasing of  $B_2O_3$  content lead to decreasing of the magnetization. Generally, the magnetism of vanadium borate based-glass can exhibit diamagnetic with negative magnetic susceptibility balance from  $V_2O_5$  ( $V^{5+}$ ) [13] and paramagnetic with positive magnetic susceptibility balance from  $V_2O_4$  ( $V^{4+}$ ) and  $V_2O_3$  ( $V^{3+}$ ) [13,23,24]. The Laorodphan et al. [13] reported that the all

vanadium borate glass samples containing 5 to 25% mol  $V_2O_5$  are diamagnetic due to the presence of +5 oxidation state of vanadium in these glasses. Chinkhota et al. [23] reported that the vanadium strontium borate glasses exhibit paramagnetic behavior due to magnetic  $V^{4+}$  ions with increasing  $V_2O_5$  concentrations being present in the samples. Therefore, the paramagnetic behavior of  $x = 1.0$  and  $x = 2.0$  samples attribute to present of +4 oxidation state with high magnetic moment [10] in these samples, which confirmed by the XANES and XPS technique. Although amount of paramagnetic ion  $V^{4+}$  present in  $x = 1.0$  sample more than the  $x = 2.0$  sample but the magnetization at 10 KOe of  $x = 1.0$  sample is higher than  $x = 2.0$  sample. Moreover, the  $x = 3.0$  sample demonstrated the diamagnetic behavior. Therefore, we believe that the decreasing of the magnetization of paramagnetic in  $x = 1.0$  and  $x = 2.0$  samples and the diamagnetic behavior of  $x = 3.0$  sample attribute to decreasing of  $V_2O_5$  concentrations and increasing of diamagnetic  $B_2O_3$  content in these sample.

### 3.6. Applications of these glasses

Interestingly, the  $V_2O_5$  based electrode materials have high specific capacity ( $> 200$  mAh/g) for battery [3,25] and high specific capacitance (635 F/g) for supercapacitor [26], respectively attributed to the redox reaction during the charge and discharge, which correspond to the conversion of  $V^{4+}$  and  $V^{5+}$  [27]. Therefore, from the above reason, the prepared vanadium-lithium-borate glasses in this work with the various oxidation states are probable the good candidate for electrochemical energy storage devices i.e. battery and supercapacitor.

### 4. Conclusions

In this study, the  $0.5V_2O_5-0.5(Li_2O-xB_2O_3)$  with  $x = 1.0, 2.0$  and

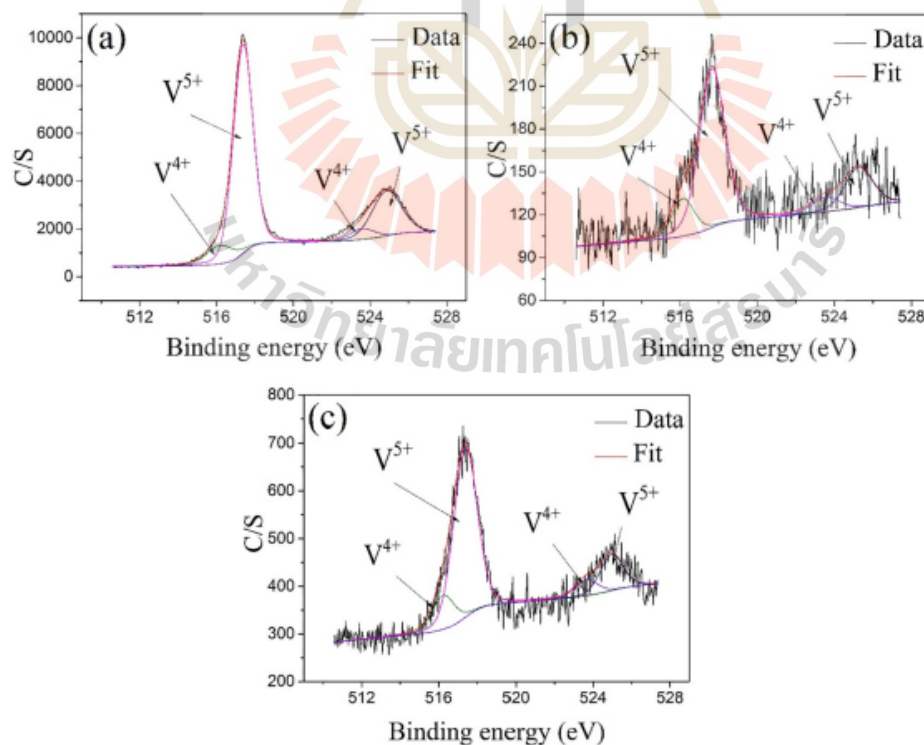


Fig. 7. XPS profiles of glass samples: (a)  $x = 1$ , (b)  $x = 2$ , (c)  $x = 3$ .

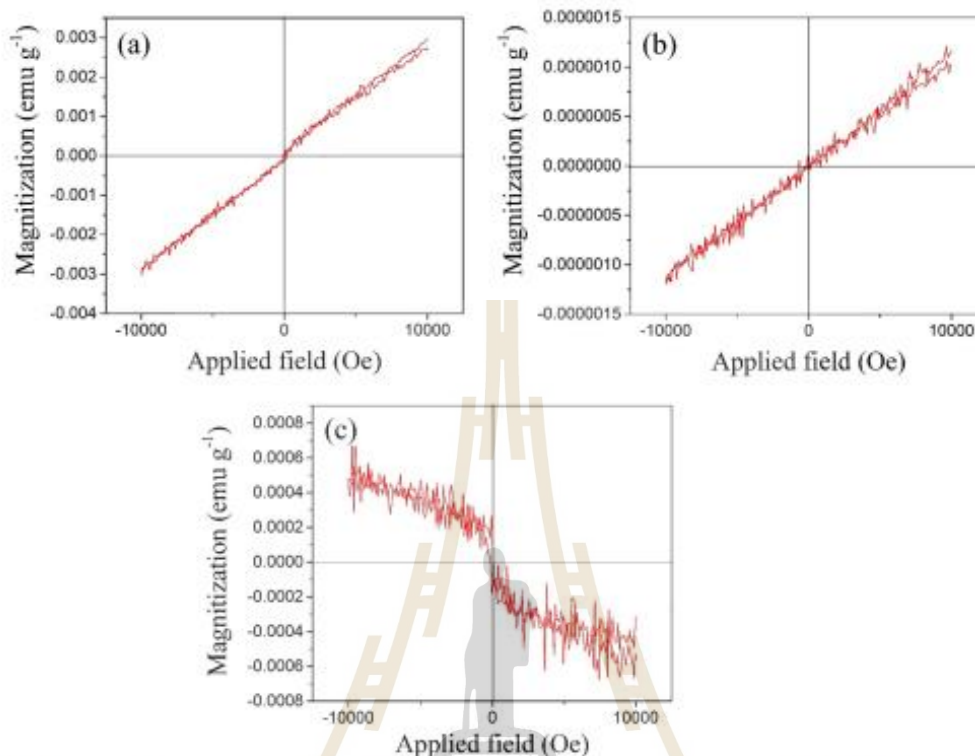


Fig. 8. Room temperature magnetization hysteresis loop of  $0.5V_2O_5-0.5(Li_2O-xB_2O_3)$  glass samples: (a)  $x = 1$ , (b)  $x = 2$ , (c)  $x = 3$ .

$3.0$  glasses were successfully prepared by the conventional melt-quench method. Optical absorption and XANES analysis evidently propose that there is  $V^{4+}$  and  $V^{5+}$  ions in all glass samples. The  $x = 2.0$  sample has the highest  $V^{4+}/V^{5+}$  confirmed by XPS analysis. The  $x = 1.0$  and  $x = 2.0$  samples exhibit paramagnetic behavior due to the presence of magnetic  $V^{4+}$  ions, while the  $x = 3.0$  sample exhibits diamagnetic behavior, which attribute to the presence of overabundantly diamagnetic behavior of  $B_2O_3$ . It is expected that the vanadium-lithium-borate glasses can be considered as a candidate for magnetic and electrochemical applications.

#### Acknowledgments

The authors would like to thank the Synchrotron Light Research Institute (Public Organization) (BL5.2), Thailand for the XAS and XPS facilities. Many thanks to Department of Physics, Khon Kaen University for VSM facilities and Department of Industrial Chemistry and Textile Technology, Maejo University and School of Physics and Center of Excellent on Advanced Functional Materials, Suranaree University of Technology for laboratory facilities.

#### Appendix A. Supplementary data

Supplementary data to this article can be found online at <https://doi.org/10.1016/j.noncrysol.2018.04.045>.

#### References

- [1] L. Rivoalen, A. Revcolevschi, J. Livage, R. Collongues, *J. Non-Cryst. Solids* 21 (1976) 171–179.
- [2] G. Ori, M. Montosi, A. Pedone, C. Siligardi, *J. Non-Cryst. Solids* 357 (2011)

- 2571–2579.
- [3] S. Afyon, F. Krumeich, C. Mensing, A. Borgschulte, R. Nesper, *Sci. Rep.* 4 (2014).
- [4] Y. Sakurai, T. Hirai, S. Okada, T. Okada, J.I. Yamaki, H. Ohtsuka, *United States Patent US 4675260 A*, 1987.
- [5] Y. Sakurai, J. Yamaki, *J. Electrochem. Soc.* 132 (1985) 152–153.
- [6] Y. Sakurai, J.I. Yamaki, *J. Electrochem. Soc.* 135 (1988) 791–796.
- [7] V. Kundu, R. Dhiman, D. Goyal, A. Maan, *Optoelectron. Adv. Mater.* 2 (2008) 428–432.
- [8] K. Padmasree, D. Kanchan, *Mater. Sci. Eng. C* 122 (2005) 24–28.
- [9] S. Khass, V. Seth, S. Gupta, R.M. Krishna, *Phys. Chem. Glasses* 40 (1999) 269–272.
- [10] I. Kishif, A. Sanad, Y. Abo Zeid, *Phys. Chem. Glasses* 31 (1990) 196–198.
- [11] E. Culea, A. Nicula, *Solid State Commun.* 58 (1986) 545–549.
- [12] R. Sharma, D. Dubey, A. Mani Singh, *J. Non-Cryst. Solids* 65 (1984) 39–51.
- [13] N. Laorodphan, P. Paeddee, P. Kidkhunthod, P. Kuntadree, W. Tapala, R. Puntumart, *J. Non-Cryst. Solids* 453 (2016) 118–124.
- [14] P. Kidkhunthod, *Adv. Nat. Sci. Nanosci. Nanotechnol.* 8 (2017) 035007.
- [15] W. Klysubun, P. Kidkhunthod, P. Tanawarakarn, P. Sombunchoo, C. Kongmark, S. Limpjumnong, S. Rujirawat, R. Yimnirun, G. Tumcharern, K. Faungnawakij, *J. Synchrotron, Radiat. Ther.* 24 (2017) 1–10.
- [16] M. Gaafar, H. Afifi, M. Mekawy, *Phys. B Condens. Matter* 404 (2009) 1668–1673.
- [17] R.B. Rao, N. Gopal, N. Veeralah, *J. Alloys Compd.* 368 (2004) 25–37.
- [18] A. Abdelghany, A.H. Hammad, *Spectrochim. Acta A Mol. Biomol. Spectrosc.* 137 (2015) 39–44.
- [19] S.S. Sastry, *Indian. J. Pure. Ap. Phys.* 52 (2015) 491–498.
- [20] C. Dayanand, R. Sarma, G. Bhikshamaiah, M. Salagram, *J. Non-Cryst. Solids* 167 (1994) 122–126.
- [21] K. Srilatha, L. Pavic, A. Mogus-Milankovic, C.S. Rao, G.L. Flower, V.R. Kumar, N. Veeralah, *J. Non-Cryst. Solids* 357 (2011) 3538–3547.
- [22] J. Wong, F. Lytle, R. Messmer, D. Maylotte, *Phys. Rev. B* 30 (1984) 5596.
- [23] M. Chinkhota, P.S. Fodor, G. Khattak, L.E. Wenger, *J. Appl. Phys.* 91 (2002) 8269–8271.
- [24] E. Assem, *Key Eng. Mater.* 224 (2002) 145–150.
- [25] S.H. Ng, S.Y. Chew, J. Wang, D. Wexler, Y. Tourmayre, K. Konstantinov, H.K. Liu, *J. Power Sources* 174 (2007) 1032–1035.
- [26] D.H. Nagaraju, Q. Wang, P. Beaujuge, H.N. Alshareef, *J. Mater. Chem. A* 2 (2014) 17146–17152.
- [27] C. Liu, E.I. Gillette, X. Chen, A.J. Pearse, A.C. Kozem, M.A. Schroeder, K.E. Gregorczyk, S.B. Lee, G.W. Rubloff, *Nat. Nanotechnol.* 9 (2014) 1031–1039.



Contents lists available at ScienceDirect

## Radiation Physics and Chemistry

journal homepage: [www.elsevier.com/locate/radphyschem](http://www.elsevier.com/locate/radphyschem)

## Effect of borate glass network to electrochemical properties: Manganese-doped lithium borate glasses

Amorntep Montreeuppathum<sup>a</sup>, Pinit Kidkhunthod<sup>b,\*</sup>, Saroj Rujirawat<sup>a</sup>, Rattikorn Yimnirun<sup>c</sup>, Supree Pinitsoontorn<sup>d</sup>, Santi Maensiri<sup>a,e</sup><sup>a</sup> School of Physics, Institute of Science, Suranaree University of Technology, Nakhon Ratchasima, 30000, Thailand<sup>b</sup> Synchrotron Light Research Institute (Public Organisation), Nakhon Ratchasima, 30000, Thailand<sup>c</sup> School of Energy Science and Engineering, Vidyasirimedhi Institute of Science and Technology, Rayong, 21210, Thailand<sup>d</sup> Institute of Nanomaterials Research and Innovation for Energy (IN-RIE), Khon Kaen University, Khon Kaen, 40002, Thailand<sup>e</sup> Center of Excellent on Advanced Functional Materials, Suranaree University of Technology, Nakhon Ratchasima, 30000, Thailand

## ARTICLE INFO

## Keywords:

Manganese-lithium-borate glasses

XAS

VSM

Electrochemical

## ABSTRACT

Recent development of manganese-lithium borate glasses for applications as supercapacitor was reported. The glasses were prepared by melt-quench technique and characterized by x-ray diffraction (XRD), scanning electron microscopy (SEM), and Uv-visible spectroscopy (UV-VIS). The paramagnetism of synthesized glasses was observed at room temperature measured by vibrating sample magnetometry (VSM). The electrochemical properties were studied by cyclic voltammetry (CV). The specific capacitance of  $0.2\text{MnO}_2\text{-}0.8(\text{Li}_2\text{O-xB}_2\text{O}_3)$  glasses were increase from  $144\text{ F g}^{-1}$  to  $196\text{ F g}^{-1}$  for  $x = 1$  to  $x = 3$  (mol%) with scanning rate of  $5\text{ mV s}^{-1}$ . However, the specific capacitance was decrease when  $x = 4$ . To understand the structure-function of these glasses, the x-ray absorption spectroscopy (XAS) was also used to study a local structure and oxidation state of Mn content in these glasses. Mixing of  $\text{Mn}^{2+}/\text{Mn}^{3+}$  oxidation state was exhibited with the mean Mn-O bonding distance of approximately  $2.0495\text{ \AA}$ .

## 1. Introduction

Glasses and glasses-ceramic belong to advance function materials. The properties and methodology of these were reported (Karmakar, 2017). Glasses are increasing interested due to their application in field of solid-state batteries, optical detector, optical fiber, etc. Glasses have several advantages over crystal materials such as glasses can be prepared in any size and shape. Among all glasses lithium borate glasses are widely studies because of their potential application (Ramteke and Gedam, 2014; Pye et al., 1978; Berkemeier et al., 2017; Rao et al., 1996).

A development of electrode materials for the supercapacitor is significant topic. The specific capacitance of each material for supercapacitor depend on several part such as the electrode materials, electrolyte, etc. In case of electrode potential materials, the carbon-based materials have a capacitance lower than the pseudo capacitor metal oxide-based materials (Lokhande et al., 2011; Zhao et al., 2013). The manganese oxide materials such as  $\text{Mn}_2\text{O}_4$  and  $\text{MnO}_2$  was interested in application to be supercapacitor electrode materials due to eco-friendly, inexpensive, various oxidation state and high specific capacitance for

$\sim 1400\text{ F g}^{-1}$  and  $\sim 1370\text{ F g}^{-1}$ , respectively (Qi et al., 2016; Toupin et al., 2014). The lithium and manganese have much been interested in future cathode materials for application to rechargeable Li-ion batteries due to these materials has a high energy density for  $\sim 1000\text{ Wh.kg}^{-1}$  and low cost compared to commercialization of  $\text{LiCoO}_2$  (Ozoemena and Chen, 2016; Yu and Zhou, 2013).

Recently, the lithium borate glasses materials have obtained much attention in energy storage resource (Afyon et al., 2014). The metal oxide with crystalline structural form used as electrode materials can performed high capacities. However, the crystalline electrode materials have some issue such as the electrode swelled, and ion penetrated the crystalline lattice. These reasons, the researchers try to replace crystalline electrode materials by using a glass in form amorphous structure. The flexibility of the glass structure is related with the changing in the bonding of angle connecting network-forming polyhedral such as Si-O-Si bond angle can vary in the range  $125^\circ\text{-}165^\circ$ , and the P-O-P bond angle in the phosphate glass can vary in the range  $123^\circ\text{-}180^\circ$ . In the case of borate glass bond angle can greatly change in boroxol ring in borate structure. All these materials process an especially high glass forming ability (Stoch, 1999). From the previous study, the vanadium

\* Corresponding author.

E-mail address: [pinit@slri.or.th](mailto:pinit@slri.or.th) (P. Kidkhunthod).<https://doi.org/10.1016/j.radphyschem.2019.108677>

Received 24 October 2019; Received in revised form 18 December 2019; Accepted 31 December 2019

Available online 31 December 2019

0969-806X/© 2020 Elsevier Ltd. All rights reserved.

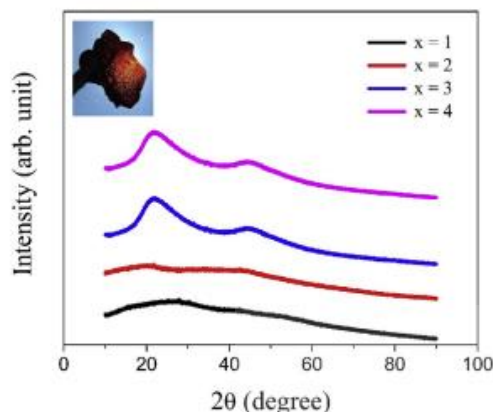


Fig. 1. X-ray diffraction of  $0.2\text{MnO}_2 - 0.8(1\text{Li}_2\text{O} - x\text{B}_2\text{O}_3)$  where  $x = 1, 2, 3$  and  $4$  (mol%) glass samples.

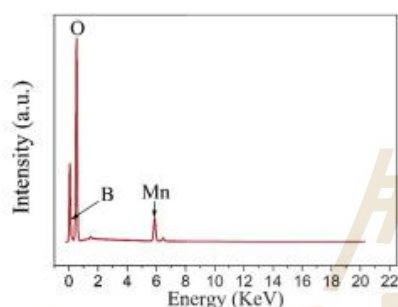


Fig. 2. EDS mapping of  $0.2\text{MnO}_2 - 0.8(1\text{Li}_2\text{O} - 1\text{B}_2\text{O}_3)$  samples.

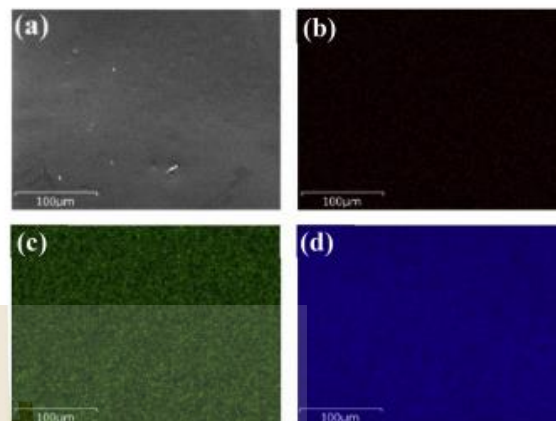


Fig. 3. SEM image of  $0.2\text{MnO}_2 - 0.8(1\text{Li}_2\text{O} - 1\text{B}_2\text{O}_3)$  samples, (a) samples, (b) boron distribution, (c) manganese distribution and (d) oxygen distribution.

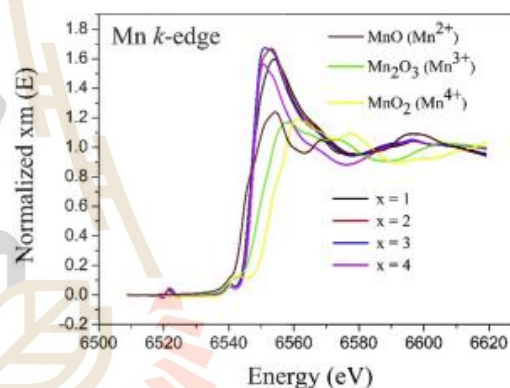


Fig. 4. XANES spectra of Mn  $k$ -edge of  $0.2\text{MnO}_2 - 0.8(1\text{Li}_2\text{O} - x\text{B}_2\text{O}_3)$  where  $x = 1, 2, 3, 4$  (mol%) glass samples and standard samples.

Table 1

The percentage content of the glasses sample with difference composition.

Samples	Element		
	Boron (%)	Manganese (%)	Oxygen (%)
$0.2\text{MnO}_2 - 0.8(1\text{Li}_2\text{O} - 1\text{B}_2\text{O}_3)$	13.8	17.0	69.2
$0.2\text{MnO}_2 - 0.8(1\text{Li}_2\text{O} - 2\text{B}_2\text{O}_3)$	20.7	9.4	69.9
$0.2\text{MnO}_2 - 0.8(1\text{Li}_2\text{O} - 3\text{B}_2\text{O}_3)$	27.7	2.0	70.3
$0.2\text{MnO}_2 - 0.8(1\text{Li}_2\text{O} - 4\text{B}_2\text{O}_3)$	50.4	0.1	49.5

lithium borate-base glasses ( $\text{V}_2\text{O}_5\text{-LiBO}_2$ ) have high specific capacity around  $400 \text{ mAh.g}^{-1}$  and keep going high capacity in range of  $\sim 300 \text{ mAh.g}^{-1}$  at  $50 \text{ mA.g}^{-1}$  rate for 100 cycles.  $\text{V}_2\text{O}_5\text{-LiBO}_2$  glasses are considered as promising cathode materials for rechargeable Li-ion batteries. (Afyon et al., 2014).

In this study, the manganese lithium borate glass systems were synthesized by melt-quench method using electrical furnace. The phase formation and morphology of all samples were characterized by XRD, SEM and XAS. Furthermore, the cyclic voltammetry (CV) was used to perform the electrical properties.

## 2. Experimental work

### 2.1. Preparation of glasses

In this study, the synthesis method was separated into two parts. The first part is preparation of  $\text{Li}_2\text{O-xB}_2\text{O}_3$ ; (LB) with  $x = 1, 2, 3$ , and  $4$  (mol%). The stoichiometric composition of lithium carbonate ( $\text{Li}_2\text{CO}_3$ ,

99.5%) and Boric acid ( $\text{H}_3\text{BO}_3$ , 99.8%) were weight and mixed. Then, the mixed powders were melted at  $1150^\circ\text{C}$  for 1 h in platinum crucible using an electric furnace in air. The molten mixture was taken out of furnace at  $1150^\circ\text{C}$  and quenched between two stainless steel plates at room temperature. The second part is preparation of  $0.2\text{MnO}_2 - 0.8(1\text{Li}_2\text{O} - x\text{B}_2\text{O}_3)$ ; (MLB) with  $x = 1, 2, 3$ , and  $4$  (mol%), the LB samples were ground and mixed with manganese dioxide ( $\text{MnO}_2$ , 99.0%) in agate mortar. The mixtures of LB and MLB powders were melted at  $1200^\circ\text{C}$  for 1 h in platinum crucible and quenched between two stainless steel plates at room temperature. The transparent MLB glasses with brown color were fabricated by this part.

### 2.2. Characterization of the samples

Scanning electron microscopy and energy dispersive X-ray spectroscopy (SEM&EDS; FEI-Quanta450) were performed on all powder samples to studies the morphologies and the element distribution of these glasses. The element mapping of oxygen, boron and manganese were measured using SEM-EDS technique. The phase formation of all samples was measured by X-ray diffractometer (XRD; Rigaku). The electrochemical behavior of all samples was measured by three-electrode test cell consisting of an active material working cathode, platinum wire counter electrode and Ag/AgCl reference electrode, electrolyte of 6 M KOH (Potassium Hydroxide) by potentiostat/galvanostat

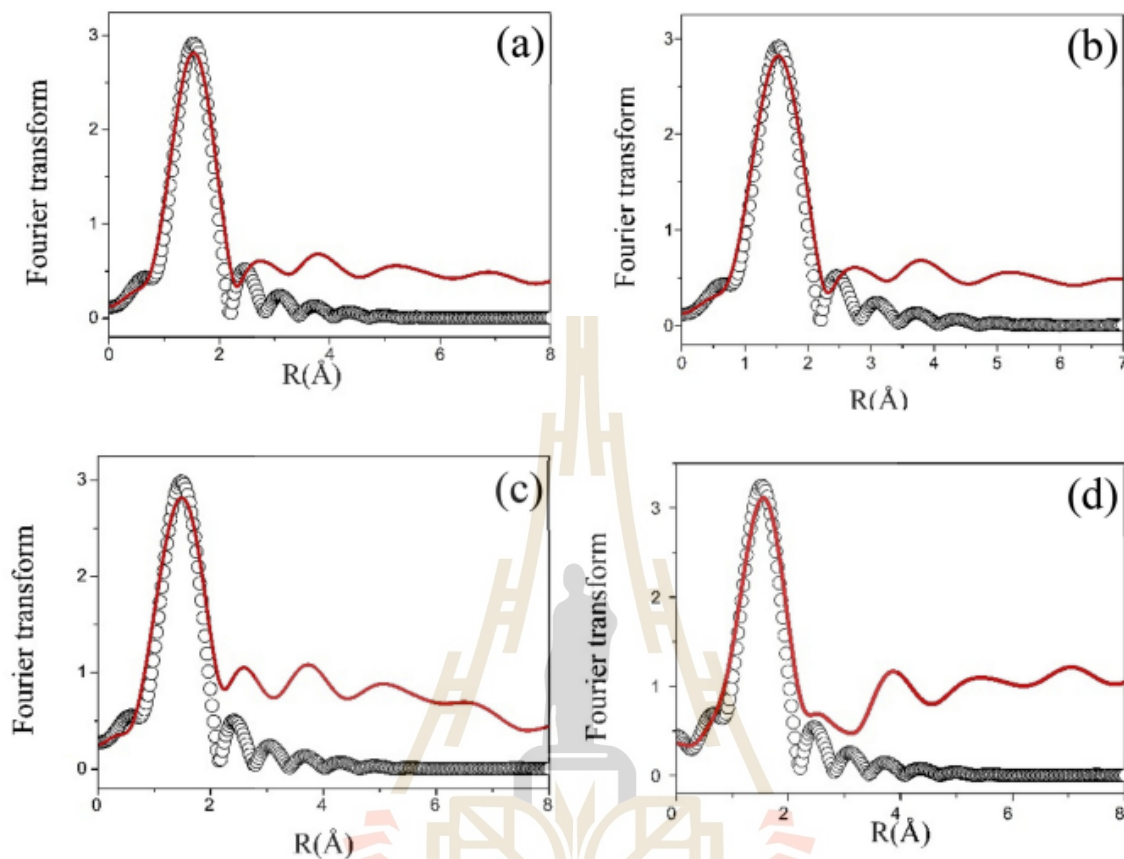


Fig. 5. Fourier transform plot at Mn  $k$ -edge from experiment (dot line) and fitting (solid line) of  $0.2\text{MnO}_2 - 0.8(1\text{Li}_2\text{O} - x\text{B}_2\text{O}_3)$  where  $x = 1, 2, 3,$  and  $4$  (mol%) glass samples.

**Table 2**  
EXAFS fitting parameter of  $0.2\text{MnO}_2 - 0.8(1\text{Li}_2\text{O} - x\text{B}_2\text{O}_3)$  where  $x = 1, 2, 3$  and  $4$  (mol%) glass samples.

Samples	Paths	$S_0^2$	N	$\sigma^2$	$E_0$	$\Delta R(\text{\AA})$	$R(\text{\AA})$
$0.20\text{Mn}-0.80(1\text{Li}_2\text{O}-1\text{B}_2\text{O}_3)$	Mn-O	2.477	1	0.00779	-2.391	-0.05046	2.04954
$0.20\text{Mn}-0.80(1\text{Li}_2\text{O}-2\text{B}_2\text{O}_3)$	Mn-O	2.782	1	0.00595	-5.318	-0.05896	2.04103
$0.20\text{Mn}-0.80(1\text{Li}_2\text{O}-3\text{B}_2\text{O}_3)$	Mn-O	2.782	1	0.00794	-7.454	-0.06650	2.03350
$0.20\text{Mn}-0.80(1\text{Li}_2\text{O}-4\text{B}_2\text{O}_3)$	Mn-O	3.057	1	0.00776	-6.168	-0.02271	2.07729

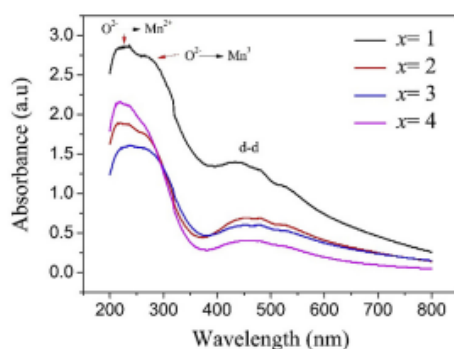


Fig. 6. Optical absorbance spectra of  $0.2\text{MnO}_2 - 0.8(1\text{Li}_2\text{O} - x\text{B}_2\text{O}_3)$  glasses samples: where  $x = 1, 2, 3$  and  $4$  (mol%).

(Metrohm autolab). The local structure and valence stats of Mn atoms was studied by Synchrotron-based XANES and EXAFS spectra at the SUT-NANOTEC-SLRI XAS Beamline (BL5.2) (Kidkhunthod, 2017; Klysubun et al., 2017) under the Synchrotron Light Research Institute (Public Organization), Thailand. XANES and EXAFS spectra at Mn  $k$ -edge were measured by transmission mode.

### 3. Result and discussion

All prepared manganese lithium borate glasses showed dense and smooth surface in transparent dark brown color. The XRD technique was chosen to confirm the amorphous phase of each samples. The samples were measured in powder form and the diffractograms was calibrated to operate in step of  $0.05^\circ$  in range of two theta form  $10^\circ-90^\circ$ . The XRD patterns of all glass present broad and no detectable any sharp peak as seen in Fig. 1. The broad band appeared at two theta confirm the amorphous phase of samples. Moreover, the increasing of intensity

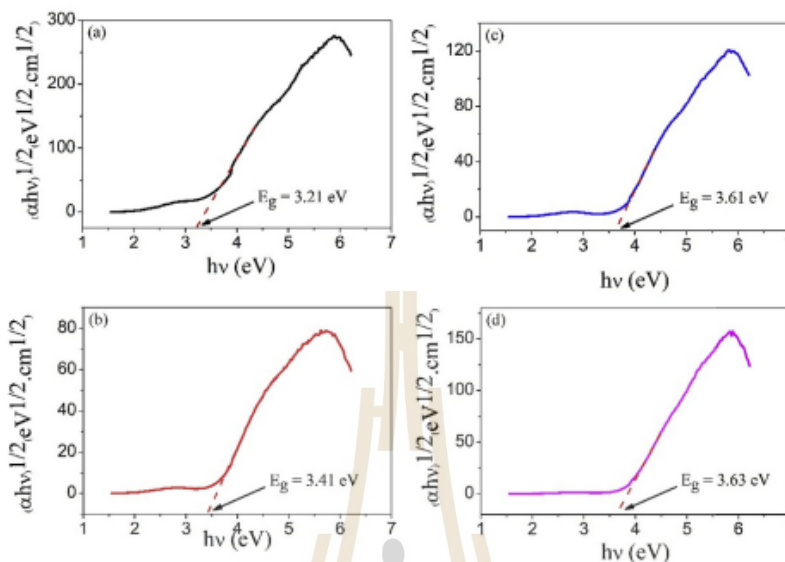


Fig. 7. Plot of  $(\alpha h\nu)^{1/2}$  as function of photon energy ( $h\nu$ ) of  $0.2\text{MnO}_2 - 0.8(1\text{Li}_2\text{O} - x\text{B}_2\text{O}_3)$  glass samples: where (a)  $x = 1$ , (b)  $x = 2$ , (c)  $x = 3$  and (d)  $x = 4$  (mol %).

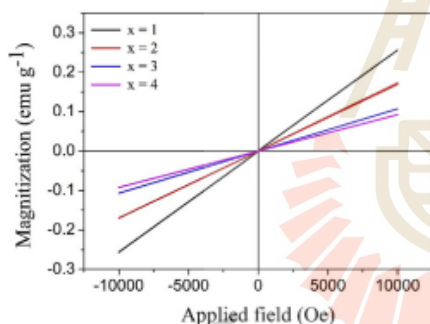


Fig. 8. Magnetization hysteresis loop of  $0.2\text{MnO}_2 - 0.8(1\text{Li}_2\text{O} - x\text{B}_2\text{O}_3)$  where  $x = 1, 2, 3, 4$  (mol%) samples measured at room temperature.

peak confirms the increasing of glassy state when increased amount boron content.

The SEM-EDS were used to observation the compositional information of the samples:  $0.2\text{MnO}_2 - 0.8(1\text{Li}_2\text{O} - x\text{B}_2\text{O}_3)$  where  $x = 1, 2, 3$  and  $4$  (mol%). The EDS spectrum confirmed the presence elemental composition of manganese, boron and oxygen in glasses samples were shown in Fig. 2 with the percentage of elemental distribution as seen in Table 1. However, no detection of lithium trace element because this technique cannot identify the low energy element. Moreover, the EDS maps used indicated the distribution of each element in selected areas which present in amount values of color dot in EDS mapping as seen in Fig. 3. The amount dot of boron increases with increasing boron content which confirmed the variation of boron content in glass systems. The high value of the oxygen content comparing with other element indicates the glass samples are oxide-based compound.

Normalized XANES spectra at the Mn  $k$ -edge of all samples compared with standard samples of  $\text{MnO}$  ( $\text{Mn}^{2+}$ ),  $\text{Mn}_2\text{O}_3$  ( $\text{Mn}^{3+}$ ) and  $\text{MnO}_2$  ( $\text{Mn}^{4+}$ ) are shown in Fig. 4. The position of the adsorption edge at Mn  $k$ -edge of all samples appeared between the adsorption edge of  $\text{MnO}$  and  $\text{Mn}_2\text{O}_3$  standard. This indicates the mixing oxidation state of  $\text{Mn}^{2+}$  and  $\text{Mn}^{3+}$  in all glass samples. To understand the environment of

Mn atom in glasses, EXAFS data were analyzed and fitted as shown in Fig. 5(a–d). The position of main peak at  $\sim 1.70 \text{ \AA}$  (no phase shift correction, approximately  $0.3 \text{ \AA}$  should be added) correspond to the Mn–O bonding distance and this peak was also used for first shell model fitting. The distance of Mn–O bonding was characterized at Mn  $k$ -edge, the bonding distance are between  $2.033 - 2.077 \text{ \AA}$ . With increasing the boron contents or in the other term the decreasing of manganese concentration in glass structure, the mean number of oxygen atoms around Mn ions trends to be increased. The importance parameters of the EXAFS fitting are amplitude reduction ( $S_0^2$ ), model coordination number ( $N$ ), Debye-Waller factors ( $\sigma^2$ ), edge energy ( $E_0$ ), Shift of bonding distance between atom ( $\Delta R$ ) and interatomic distances ( $R$ ) as seen in Table 2.

The study of optical absorption, the spectra of glass samples observed in the wavelength region in range of  $200 - 800 \text{ nm}$  at room temperature as shown in Fig. 6. The features of spectra are similar trend. The continuous absorption of all samples appeared at  $200 - 280 \text{ nm}$  and  $400 - 550 \text{ nm}$ . The study of charge transfer of  $\text{Mn}_3\text{O}_4$  was reported that the  $\text{O}^{2-} \rightarrow \text{Mn}^{2+}$  and  $\text{O}^{2-} \rightarrow \text{Mn}^{3+}$  charge transfer transition at  $261 \text{ nm}$  and  $332 \text{ nm}$  (Bose and Biju, 2015; Raj et al., 2010; Boyero Macstre et al., 2001), d-d transition on octahedral  $\text{Mn}^{3+}$  type at  $43 \text{ nm}$  (Baldi et al., 1998; Valigi and Cimino, 2015). Furthermore, energy band gap of all glass samples was calculated using equation (1) (Abdelghany and Hammad, 2015).

$$\alpha h\nu = A(h\nu - E_g)^2 \quad (1)$$

where  $\alpha$  is the absorption coefficient,  $h\nu$  is the incident photon energy,  $A$  is a constant and  $E_g$  is the optical band gap energy. The band gap was measured from the intercept on energy axis obtained by extrapolating the linear portion of the Tauc plot of  $(\alpha h\nu)^2$  vs  $(h\nu)$  as shown in Fig. 7(a–d). The energy band gap of all samples is  $3.21, 3.41, 3.61$  and  $3.63 \text{ eV}$  for  $x = 1, 2, 3$  and  $4$  (mol%), respectively. The energy band gaps are slightly increase with higher boron content in the glass samples. The energy band gap studies by Laorodphan et al. (2016) of vanadate-borate-based glasses trended to be decreased with increasing the boron contents while present study of manganate-borate-based glasses showed the increasing of band gap with increasing the boron contents. This difference in trends of energy band gap might come from the effect

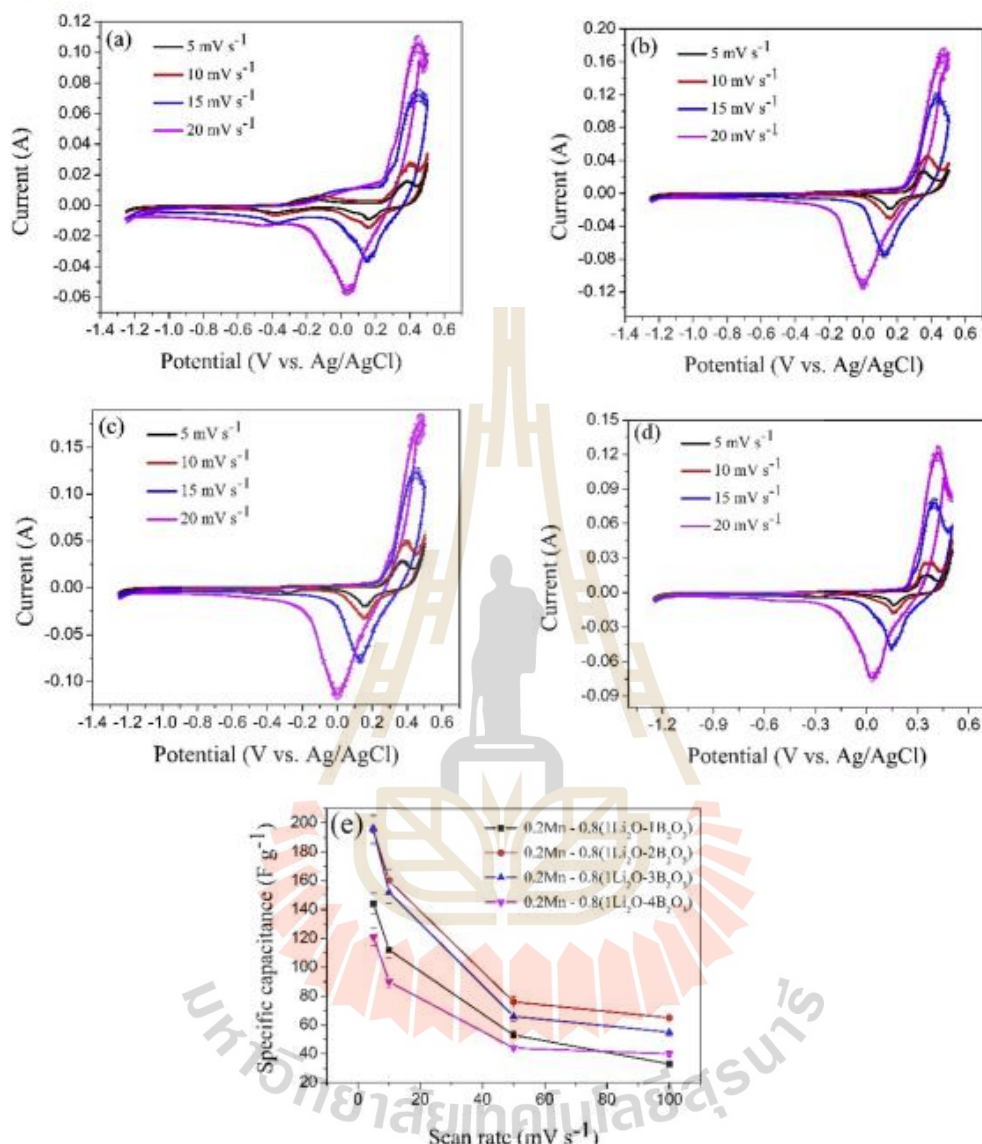


Fig. 9. Cycle voltammograms of (a) 0.2MnO<sub>2</sub> - 0.8(1Li<sub>2</sub>O-1B<sub>2</sub>O<sub>3</sub>), (b) 0.2MnO<sub>2</sub> - 0.8(1Li<sub>2</sub>O-2B<sub>2</sub>O<sub>3</sub>), (c) 0.2MnO<sub>2</sub> - 0.8(1Li<sub>2</sub>O-3B<sub>2</sub>O<sub>3</sub>) and (d) 0.2MnO<sub>2</sub> - 0.8(1Li<sub>2</sub>O-4B<sub>2</sub>O<sub>3</sub>) glasses electrode at different scan rate (e) plot of specific capacitance versus scan rate.

of manganese ions with mix manganese oxidation states of Mn<sup>2+</sup>/Mn<sup>3+</sup>. The shift of band gap energy can be due to the formation of non-bridging oxygens. The change in band gap energy is attributed to the structural change due to occupancy of difference site by cation (Kaur et al., 2014).

The magnetization behavior of the manganese-lithium borate glass samples was shown in Fig. 8. The glass samples exhibited the paramagnetic at room temperature, which is consistent with previous study of Mn-doped ZnO (Phan et al., 2011). The highest magnetism at 10,000 Oe is 0.256 emu g<sup>-1</sup> for x = 1 sample, the magnetization decreases with the increasing of boron content in glasses samples due to borate-based glass exhibits the diamagnetic behavior (Laorodphan et al., 2016). These effects are corresponded to the increasing glassy as observed in XRD result. In this study, we focus on the effect of boron content on magnetic properties of glasses. The decreasing of paramagnetism with increasing the boron contents were clearly observed

suggesting the increase of specific capacitance of prepared glasses. These observed magnetism and electrochemical properties of these glasses can imply the possibility of the use of these glasses as cathode for energy storage application e.g. battery or supercapacitor cathodes.

The CV curve of all samples (as seen in the Fig. 9), the pseudo capacitive behavior with anodic peak (charging) and cathodic peak (discharging) were reported in range of potential 0.40–0.45 V and 0.02–0.18 V, respectively indicating that the reduction state and oxidation state during the reaction is electrochemically reversible. The area of CV curve with different scan rate (5, 10, 15 and 20 mV s<sup>-1</sup> in 2 M KOH electrolyte) were used to calculate the specific capacitance. The relation of specific capacitance can be obtained by using the following equation:

$$C_{cv} = \frac{1}{vm\Delta V} \int IdV \quad (2)$$

where  $v$  is the scan rate ( $\text{mV s}^{-1}$ ),  $m$  is the mass of active materials(g),  $\Delta V$  is the potential window(V) and  $I$  is the response current(A) (Khanjonrit et al., 2018; Yan et al., 2012).

The specific capacitance of the glass electrode materials was calculated from the area of CV curve at various scan rate as showed in Fig. 9(e). The specific capacitance of  $0.2\text{MnO}_2 - 0.8(1\text{Li}_2\text{O} - x\text{B}_2\text{O}_3)$  are increase from  $144 \text{ F g}^{-1}$  ( $x = 1$ ) to  $196 \text{ F g}^{-1}$  ( $x = 3$ ) measured at scan rate of  $5 \text{ mV s}^{-1}$  and after that decrease with increasing boron content,  $121.54 \text{ F g}^{-1}$ , ( $x = 4$ ) suggesting the effect boron content in glass sample. Moreover, the highest specific capacitance is slightly higher than the previous manganese lithium borate glass has been reported ( $187.05 \text{ F g}^{-1}$ ) (Khanjonrit et al., 2018). However, the specific capacitance values of the glass electrode are decrease with increasing scan rate because at higher scan rate electrolyte ion do not get enough time to diffuse deep in to the pores of the materials (Mondal et al., 2016). This trend is observed for all systems. It can be noted that the higher redox reaction of Mn oxidation state present high specific capacitance. However, the low scan rate may get enough time of electrolyte ions to arrive the electrode surface pores which may cause improvement of ion transfer (Gupta et al., 2015).

#### 4. Conclusion

In this study, the  $0.2\text{MnO}_2 - 0.8(1\text{Li}_2\text{O} - x\text{B}_2\text{O}_3)$  glasses where  $x = 1, 2, 3$  and  $4$  (mol%) were successfully prepared by conventional melt-quench technique. The XANES result indicated that Mn in glasses samples are mixing oxidation state between  $\text{Mn}^{2+}$  and  $\text{Mn}^{3+}$ . The optical properties confirmed the Mn oxidation state as absorption at 200–280 nm and 400–550 nm is charge transfer of  $\text{Mn}^{2+}$  and  $\text{Mn}^{3+}$ , respectively. The increasing of energy band gap related to increasing of boron content in glasses samples. The magnetic behavior of the glasses sample exhibited the paramagnetic, the highest magnetism at 10,000 Oe is  $0.256 \text{ emu g}^{-1}$  for the  $0.2\text{MnO}_2 - 0.8(1\text{Li}_2\text{O} - 1\text{B}_2\text{O}_3)$  sample. The specific capacitance of the electrode materials is 144.42, 195.37, 196.48 and  $121.54 \text{ F g}^{-1}$  for  $x = 1, 2, 3$  and  $4$  (mol%) sample, respectively. Consequently, the manganese lithium borate glass is a promising energy storage electrode material such as supercapacitor or lithium battery application.

#### Declaration of competing interest

The authors declare that they have no known competing financial interests or personal relationships that could have appeared to influence the work reported in this paper.

#### Acknowledgments

The authors would like to thank the Synchrotron Light Research Institute (Public organization), the SUT-NANOTEC-SLRI XAS beamline (BL5.2), Thailand for XAS facilities. Many thank you for financial support by the NANOTECH, NSTDA, Ministry of Science and Technology, Thailand, through its program of Research Network NANOTECH and Center of Excellent Suranaree University of Technology on Advanced Functional Materials (CoE-SUT AFM).

#### References

- Abdelghany, A., Hammad, A.H., 2015. Impact of vanadium ions in barium borate glass. *Spectrochim. Acta A Mol. Biomol. Spectrosc.* 137, 39–44.
- Alyon, S., Krumeich, F., Mensing, C., Borgschulte, A., Nesper, R., 2014. New high capacity cathode materials for rechargeable Li-ion batteries: vanadate-borate glasses. *Sci. Rep.* 4, 7113.
- Baldi, M., Milella, F., Gallardo-Amore, J.M., 1998. A study of Mn-Ti oxide powders and their behaviour in propane oxidation catalysis. *J. Mater. Chem.* 8, 2525–2531.
- Berkemeier, F., Shoar Abouzari, M., Schmitz, G., 2017. Thickness dependent ion conductivity of lithium borate network glasses. *J. Appl. Phys. Lett.* 90, 113110.
- Bose, V.C., Biju, V., 2015. Optical, electrical and magnetic properties of nanostructured  $\text{Mn}_3\text{O}_4$  synthesized through a facile chemical route. *Phys. E Low-dimens. Syst. Nanostruct.* 66, 24–32.
- Boyer Macstre, J., Fernandez Lopez, E., Gallardo-Amores, J.M., Ruano Casero, R., 2001. Influence of the synthesis parameters on the structural and textural properties of precipitated manganese oxide. *Int. J. Inorg. Mater.* 3, 889–899.
- Gupta, R.K., Candler, J., Palchoudhury, S., Ramasamy, K., Gupta, B.K., 2015. Flexible and high-performance supercapacitors based on  $\text{NiCo}_2\text{O}_4$  for wide temperature range applications. *Sci. Rep.* 5, 15265.
- Karmakar, B., 2017. Functional Glasses and Glass-Ceramics: Processing, Properties and Applications. Butterworth-Heinemann.
- Kaur, M., Saini, M.S., Singh, D., Mudahar, G.S., 2014. Synthesis and characterization of lithium borate glasses containing bismuth. *Int. J. Adv. Res. Phys. Sci.* 1, 1–8.
- Khanjonrit, J., Wongpratat, U., Kidkhunthod, P., Pinitsoontorn, S., Maensiri, S., 2018. Effects of Co doping on magnetic and electrochemical properties of  $\text{BiFeO}_3$  nanoparticles. *J. Magn. Mater.* 449, 423–434.
- Kidkhunthod, P., 2017. Structural studies of advanced functional materials by synchrotron-based x-ray absorption spectroscopy: BL5.2 at SLRI, Thailand. *Adv. Nat. Sci. Nanosci. Nanotechnol.* 8, 035007.
- Klysubun, W., Kidkhunthod, P., Tarawaraakrn, P., Sombunchoo, P., Kongmark, C., Limpjumnong, S., Rujirawat, S., Yimnirun, R., Tumcharern, G., Faungnawakij, K., 2017. SUT-NANOTEC-SLRI beamline for X-ray absorption spectroscopy. *J. Synchrotron Radiat.* 24, 707–716.
- Laorodphan, N., Pooddee, P., Kidkhunthod, P., Kunthadee, P., Tapala, W., Puntharod, R., 2016. Boron and pentavalent vanadium local environments in binary vanadium borate glasses. *J. Non-Cryst. Solids* 453, 118–124.
- Lokhande, C., Dubal, D., Loo, O.S., 2011. Metal oxide thin film-based supercapacitors. *Curr. Appl. Phys.* 11, 255–270.
- Mondal, R., Sahoo, S., Rout, C.S., 2016. Mixed nickel cobalt manganese oxide nanorods for supercapacitor application. *Am. J. Eng. Appl. Sci.* 9 (3), 540–546.
- Ozoemena, K.I., Chen, S., 2016. Nanomaterials in Advanced Batteries and Supercapacitors. Springer.
- Phan, T.L., Zhang, P., Yang, D., Nghia, N., Yu, S., 2011. Local structure and paramagnetic properties of  $\text{Zn}_1-x\text{Mn}_x\text{O}$ . *J. Appl. Phys.* 110, 063912.
- Pye, L.D., Frechette, V.D., Kreidl, N.J., 1978. Borate Glasses: Structure, Properties and Application. Plenum Press, New York.
- Qi, Z., Younis, A., Chu, D., Li, S., 2016. Facile and template-free on e-pot synthesis  $\text{Mn}_3\text{O}_4$  nanostructures as electrochemical supercapacitors. *Nano-Micro Lett.* 8, 165–173 2016.
- Raj, A.M.E., Vaictoria, S.G., Jothy, V.B., Ravidha, C., Wollschlager, J., Suen dorf, M., Neumann, M., Jayachandran, M., Sanjeeviraja, C., 2010. XRD and XPS characterization of mixed valence  $\text{Mn}_3\text{O}_4$  hausmannite thin films prepared by chemical spray pyrolysis technique. *Appl. Surf. Sci.* 256, 2920–2926.
- Ramiecke, D.D., Grédem, B.S., 2014. Study of  $\text{Li}_2\text{O}-\text{B}_2\text{O}_3-\text{Dy}_2\text{O}_3$  glasses by impedance spectroscopy. *Solid State Ion.* 258, 82–87.
- Rao, V.M., Gopalskrishnan, R., Rao, V.V.R.N., Reddy, K.R., Buddhudu, S., 1996. Physical investigation on lithium borate glasses for solid state battery applications. *Mater. Sci. Forum* 113, 223–224.
- Stoch, S., 1999. Flexibility of structure and glass-forming ability: a chemical approach. *J. Glass Phys. And Chem.* 27 (2), 167–174.
- Toupin, M., Brousse, T., Belanger, D., 2014. Charge storage mechanism of  $\text{MnO}_2$  electrode used in aqueous electrochemical capacitor. *Chem. Mater.* 16, 3184–3190.
- Valigi, M., Cimino, A., 2015. The system  $\text{TiO}_2\text{MnO}_x$ : a structural, the thermogravimetric, and magnetic study. *J. Solid State Chem.* 12, 135–143.
- Yan, J., Liu, J., Fan, Z., Wei, T., Zhang, L., 2012. High-performance supercapacitor electrodes based on highly corrugated graphene sheets. *Carbon* 50, 2179–2188 2012.
- Yu, H., Zhou, H., 2013. High-energy cathode materials ( $\text{Li}_2\text{MnO}_3-\text{LiMO}_2$ ) for lithium-ion batteries. *J. Phys. Chem. Lett.* 4, 1268–1280.
- Zhao, G., Zhang, N., Sun, K., 2013. Porous  $\text{MoO}_3$  films with ultra-short relaxation time used for supercapacitors. *Mater. Res. Bull.* 48, 1328–1332.



Contents lists available at ScienceDirect

Journal of Alloys and Compounds

journal homepage: <http://www.elsevier.com/locate/jalcom>

## New transparent materials for applications as supercapacitors: Manganese-lithium-borate glasses

Jessada Khajonrit<sup>a</sup>, Amornthep Montreeuppathum<sup>a</sup>, Pinit Kidkhunthod<sup>a,\*</sup>, Narong Chanlek<sup>a</sup>, Yingyot Poo-arporn<sup>a</sup>, Supree Pinitsoontorn<sup>b</sup>, Santi Maensiri<sup>c,d</sup>

<sup>a</sup> Synchrotron Light Research Institute (Public Organisation), Nakhon Ratchasima, 30000, Thailand

<sup>b</sup> Integrated Nanotechnology Research Center, Department of Physics, Faculty of Science, Khon Kaen University, Khon Kaen, 40002, Thailand

<sup>c</sup> School of Physics, Institute of Science, Suranaree University of Technology, Nakhon Ratchasima, 30000, Thailand

<sup>d</sup> Center of Excellence on Advanced Functional Materials, Suranaree University of Technology, Nakhon Ratchasima, 30000, Thailand

### ARTICLE INFO

#### Article history:

Received 23 March 2018

Received in revised form

24 May 2018

Accepted 25 May 2018

Available online 26 May 2018

#### Keywords:

Manganese-lithium-borate glasses

New electrode material

X-ray absorption spectroscopy

X-ray photoelectron spectroscopy

Electrochemical properties

Supercapacitor

### ABSTRACT

The transparent manganese-lithium borate glasses were successfully prepared by melt-quench technique. The effect of the Mn content in the glasses on structure-function was characterized by conventional techniques e.g. XRD, SEM, TEM, XPS, UV-Vis and VSM. The vitreous samples exhibit pseudo capacitive behavior with the redox couple of the  $Mn^{2+}/Mn^{3+}$  proofed by advanced synchrotron-based X-ray absorption spectroscopy (XAS) technique. The cyclic voltammetry (CV), galvanostatic charge-discharge (GCD) and electrochemical impedance spectroscopy (EIS) were used to study the electrochemical properties of the prepared electrodes in 6 MKOH electrolyte. Interestingly, the increasing of Mn content from 20 mol% to 30 mol% can improve (~2 time) their specific capacitance, energy density and capacity retention. The  $0.3MnO_2-0.7(Li_2O-2B_2O_3)$  electrode exhibits the highest values of the specific capacitance ( $187.05\text{ F g}^{-1}$  for CV and  $169.66\text{ F g}^{-1}$  for GCD), specific energy density ( $19.34\text{ Wh kg}^{-1}$ ) and capacity retention (76.05%) after 1000 cycles. This attributed to decreasing of electrolyte resistance and increasing of  $Mn^{2+}$  on the glass surface. Therefore, the results assured that manganese-lithium borate glasses have a great potential for development as electrode materials in supercapacitor applications.

© 2018 Elsevier B.V. All rights reserved.

### 1. Introduction

In the recent years the electrochemical supercapacitors have attracted increasing interest for energy storage system due to fast-growing market and increasing demand of high power energy storage resources for electronic devices and power applications [1–13]. Moreover, their power density and longer life is higher than secondary batteries and energy density is higher than conventional dielectric capacitors [14]. The improvement of novel electrode materials for the supercapacitors is important topic. The key requirements in the development of the electrode materials are energy and power density, cost, environment friendly and lifetime. In recently, high surface area carbon, polymer and transition metal oxides have been used as active materials for the electrochemical supercapacitor [15]. Among the electrode potential materials, pseudocapacitors of the inexpensive metal oxides-based materials

(charges are stored through faradic reactions originated from variable oxidation states) have higher capacitance than the normal electrical double-layer capacitors of carbon-based materials (charges are stored through an adsorption/desorption process) [16,17]. The most of energy density of the available commercial carbon-based supercapacitors ( $\sim 5\text{ Wh Kg}^{-1}$ ) is lower than in batteries ( $\sim 35\text{--}200\text{ Wh Kg}^{-1}$ ) [14,18]. Therefore, the various forms of metal oxides such as  $RuO_2$ ,  $Mn_3O_4$ ,  $MnO_2$ ,  $NiO$ ,  $Co_3O_4$ , and  $V_2O_5$ , etc., have been developed to improve the energy densities of the supercapacitors [16,19]. Example,  $RuO_2$  exhibits highly reversible redox reactions in a wide potential range, high specific capacitance ( $1580\text{ F g}^{-1}$ ) and long cycling life [20]. However, it has limitations for practical application such as high cost, toxic nature and scarce in nature [15,16].

Manganese oxide materials such as  $Mn_3O_4$  and  $MnO_2$  is considered as one of the promising electrode materials due to its abundant, inexpensive, and eco-friendly, various oxidation states and high theoretical specific capacitance of  $\sim 1400\text{ F g}^{-1}$  [21] and  $\sim 1370\text{ F g}^{-1}$  [22], respectively. In recent years, several works have

\* Corresponding author.

E-mail address: [pinit@slri.or.th](mailto:pinit@slri.or.th) (P. Kidkhunthod).

been synthesized and used  $\text{Mn}_3\text{O}_4$  [23,24] and  $\text{MnO}_2$  [25] as the active material of supercapacitor which exhibited high specific capacitance with redox behavior. Shinde et al. [26] reported electrochemical features of  $\alpha\text{-MnO}_2$ ,  $\beta\text{-MnO}_2$  and  $\text{Mn}_3\text{O}_4$  electrodes, which the  $\text{Mn}_3\text{O}_4$  electrodes exhibits excellent performances with the highest values of specific capacitance ( $1064 \text{ F g}^{-1}$ ), energy density ( $94.56 \text{ Wh kg}^{-1}$ ) and cycling stability (95% over 1000 of CV cycles), respectively. Moreover, lithium and manganese rich layered cathode materials have attention as next generation cathode material for rechargeable lithium-ion battery due to high specific energy densities ( $>1000 \text{ Wh kg}^{-1}$ ) and lower cost compared to the commercialisation of  $\text{LiCoO}_2$  [19,27].

Recently, the study of novel glass materials has gained much attention in energy storage resource. The metal oxides with crystalline form used as electrode material can exhibit high capacities. However, the crystalline electrode have some limits such as the lithium ions penetrate the crystalline lattice, the lattice expands and the electrode swells. This may lead to instabilities of structural changes during charge/discharge. Thus, researchers try to retain the structure of the electrode material using in a glass form of amorphous material rather than in the crystalline form [28]. The lithium-borate-based glasses were used as next generation electrode materials for Li-ion batteries which demonstrated high capacity values through redox reaction behaviors [28]. Electrical behavior is a factor that may effect to the electrochemical properties of the glasses. Lithium borate glass can improve electrical properties such as addition of the  $\text{LiBO}_2$  glass can enhance the ionic conductivity  $\text{Li}_{3.6}\text{Si}_{0.6}\text{V}_{0.4}\text{O}_4$  system for Li ion battery application [29]. Moreover, addition of rare earths into the lithium borate glasses influenced to the electrical behavior such as  $\text{Pr}^{3+}$  [30] and  $\text{Nd}^{3+}$  [31] ions partially prevented movement of the  $\text{Li}^+$  ions in the glass matrix and decreased the conductivity of the glass. To the best of our knowledge, the advantages of incorporation of the glass materials ( $\text{Li}_2\text{O}-2\text{B}_2\text{O}_3$ ) into  $\text{MnO}_2$  are clearly explain in S.1. The boron oxide ( $\text{B}_2\text{O}_3$ ) based-glass former was been reported varieties both physical and electrical and electrochemical properties [32–37]. Various oxides such as  $\text{Fe}_2\text{O}_3$  [32], and  $\text{V}_2\text{O}_5$  [32,38] were used as network modifiers to synthesize the glass-forming oxide system. Moreover, manganese borate based-glasses containing  $\text{MnO}_2\text{-ZnO}$  [39] and  $\text{MnO}$  [40] were reported the synthesis and structural characterizations. However, the information related to the novel electrochemical properties especially valence states of Mn ions and local structure information around manganese ions of manganese-lithium-borate-based glass has not been clearly understood.

To precisely address the structure-function of these glass system, this work reported the synthesis, characterizations and electrochemical performance of the a novel active material of manganese-lithium borate glasses with formula of  $x\text{MnO}_2\text{-(1-x)}(\text{Li}_2\text{O}-2\text{B}_2\text{O}_3)$  where  $x = 0.2, 0.25$  and  $0.3$ . The structure characterizations of the prepared glass samples were investigated using various techniques such as X-ray diffraction (XRD), scanning electron microscopy (SEM), transmission electron microscopy images (TEM) and X-ray photoelectron spectroscopy (XPS). The novelty advanced technique, X-ray absorption spectroscopy (XAS) was used to understand the oxidation state and local structure information of the glass samples. The optical, magnetic and electrochemical properties of the samples were studied using UV-VIS spectrophotometer, vibrating sample magnetometry (VSM) and potentiostat/galvanostat connected with a three-electrode configuration, respectively. Moreover, the effects of Mn addition on the structure and properties were investigated in deep detail especially by synchrotron-based XAS technique.

## 2. Experimental procedures

### 2.1. Sample preparation

The manganese-lithium-borate glasses were prepared by the melt-quench technique consisting of two process of lithium borate and manganese-lithium borate glass preparation. Initially, the lithium borate preparation, the starting materials of Lithium carbonate ( $\text{Li}_2\text{CO}_3$ , 99%) and Boric acid ( $\text{H}_3\text{BO}_3$ , 99.8%) were mixed and heated in an electrical furnace at  $1100^\circ\text{C}$  for 1 h. The melts were poured on stainless plate and pressed quickly and then cooled to room temperature. For the manganese-lithium borate glass preparation, the obtained lithium borate glass sample and manganese dioxide ( $\text{MnO}_2$ , 99%) were grounded thoroughly and mixed together to get fine powder and a homogenous mixture. Finally, the homogenized powder were heated at  $1150^\circ\text{C}$  for 1 h and the melts were pressed quickly with the stainless plate.

### 2.2. Characterizations

The structure analysis of the prepared glass samples was carried out using X-ray diffraction (XRD; Rigaku). The scanning electron microscopy (SEM) and energy dispersive spectroscopy (EDS) (SEM; FEI quanta 450) were used to characterize morphology of all samples including the elemental distribution of samples. Moreover, the morphology of the prepared glass samples was observed by transmission electron microscopy (TEM) with a Tecnai G<sup>2</sup> 20 S-TWIN (FEI; field emission gun). The sample preparation for the TEM measurement, the samples were ground in an agate mortar, dispersed in ethanol and dropped on a copper grind. The observed absorption spectra were measured in the wavelength region of 200–800 nm by PerkinElmer-Lambda 950 spectrophotometer to study of optical properties of the prepared samples.

Synchrotron-based X-ray absorption spectroscopy (XAS) technique was employed to determine the valence state and local structure information of Mn in the glass samples. The experiment was measured at the SUT-NANOTEC-SLRI XAS Beamline (BL5.2) at the Synchrotron Light Research Institute (Public Organization), Thailand [41,42]. The XAS spectra including X-ray absorption near-edge structure (XANES) and X-ray absorption fine structure (EXAFS) spectra was recorded at the Mn K-edge in transmission modes. To derive the surface chemical composition of the glass samples, the X-ray photoelectron spectroscopy (XPS) spectra was carried out using a PHI 5000 Versa Probe II XPS system (ULVAC-PHI, Japan). The magnetic properties were measured using a vibrating sample magnetometer (VSM) option in the Quantum Design Versalab instrument with the field range of  $\pm 30 \text{ kOe}$  at room temperature.

### 2.3. Measurements of electrochemical properties

The electrochemical properties of all the glasses were studied in 6M KOH electrolyte by potentiostat/galvanostat (Metrohm autolab) connected with a three-electrode configuration, which consist of platinum (Pt) wire, Ag/AgCl and the prepared glass samples as counter, reference and active electrode. Moreover, NOVA software is used to control the accessories and analyze the data. For the electrode preparations, the electrodes was prepared by mixing of the glass samples with polyvinylidene fluoride (PVDF) and carbon black in the ratio 80:10:10. The mixture were mixed with the N-methyl-2-pyrrolidinone. The slurry was then pasted on a nickel foam substrate (area  $\sim 1 \text{ cm}^2$ ). The cyclic voltammogram (CV) was tested in a voltage window between  $-0.5 \text{ V}$  and  $0.5 \text{ V}$ , and the galvanostatic charge-discharge (CD) was measured between  $-0.5 \text{ V}$  and  $0.4 \text{ V}$ . Electrochemical impedance spectroscopy (EIS) was

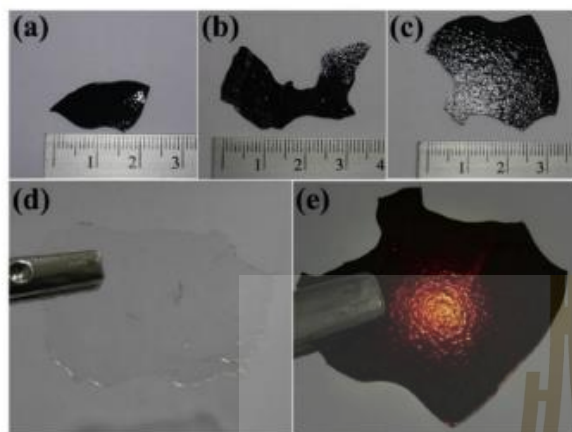


**Fig. 1.** Figures of the prepared manganese-lithium borate glass samples: (a)  $0.2\text{MnO}_2\text{-}0.8(\text{Li}_2\text{O-}2\text{B}_2\text{O}_3)$ , (b)  $0.25\text{MnO}_2\text{-}0.75(\text{Li}_2\text{O-}2\text{B}_2\text{O}_3)$  and (c)  $0.3\text{MnO}_2\text{-}0.7(\text{Li}_2\text{O-}2\text{B}_2\text{O}_3)$  and transparency of (d) prepared lithium borate and (e) manganese lithium borate glasses.

performed in the frequency range from 0.1 Hz to 100 kHz.

### 3. Results and discussion

#### 3.1. Morphological and structural characterizations

Fig. 1 shows the physical property of the prepared plate glass samples. All prepared manganese-lithium borate glass samples showed smooth, dense and black color surface as shown in Fig. 1a–c. Moreover, the prepared lithium borate and manganese-lithium borate glass samples is transparent to the visible light as shown in Fig. 1d and e.

The XRD patterns of the  $0.2\text{MnO}_2\text{-}0.8(\text{Li}_2\text{O-}2\text{B}_2\text{O}_3)$ ,  $0.25\text{MnO}_2\text{-}0.75(\text{Li}_2\text{O-}2\text{B}_2\text{O}_3)$ , and  $0.3\text{MnO}_2\text{-}0.7(\text{Li}_2\text{O-}2\text{B}_2\text{O}_3)$  samples were shown in S.2. Clearly, the patterns in all samples revealed poor crystallization with broad and weak  $\text{MnO}_2$  diffraction peaks which indicated the characteristic of the amorphous phase of the material. This confirmed the glass material is successfully prepared in all samples. The morphology and compositional information of the prepared glass samples:  $x\text{MnO}_2\text{-(}1\text{-}x)(\text{Li}_2\text{O-}2\text{B}_2\text{O}_3)$  glasses where  $x = 0.2, 0.25$  and  $0.3$  was obtained by SEM images combined with EDS mapping as shown in S.3. The SEM images revealed the smooth

surface in all samples. The elemental mapping using EDS indicated elemental composition of oxygen, manganese and boron in the samples. This indicated the increasing of Mn content in the glass samples. The tendency of O content (67.8, 65.5 and 64.4 wt%) and B content (24.1, 23.5 and 21.6 wt%) are decrease but Mn content (8.7, 9.4 and 14.0 wt%) are increase when adjusted concentration of Mn for  $x = 0.2, 0.25$  and  $0.3$  samples, respectively. The SEM images including EDS mapping were shown in the supplementary section S.3. The TEM images demonstrated the detail microstructure of the glass samples. The TEM bright field images demonstrated that the large glass pieces of the glass samples were ground to micron and sub-micron size as shown in Fig. 2. Moreover, the electron diffraction patterns of all glass samples with lack of any reflections as were shown in the inset of Fig. 2. This indicated the nature of amorphous material in all glass samples.

#### 3.2. Evidence of manganese existence by X-ray photoelectron spectroscopy (XPS)

XPS measurement is performed to determine the both composition and quantitative analysis the oxidation state in surface constituents of the glass samples. The XPS spectra correspond to the presence of  $\text{Mn}^{2+}$  and  $\text{Mn}^{3+}$  in the surface glass samples as presented in Fig. 3. The obtained energy levels of Mn 2p in this work are in agreement with the energy locations as reported earlier [43,44]. The binding energy values of the glasses of  $\text{Mn}^{2+}$  and  $\text{Mn}^{3+}$  are  $-641$  and  $-643$  eV in the Mn  $2p_{3/2}$  peak and  $-653$  eV and  $-655$  eV in the Mn  $2p_{1/2}$  peak. The calculated Mn  $2p_{3/2}$  of  $\text{Mn}^{2+}$  ( $-641$  eV)/ $\text{Mn}^{3+}$  ( $-643$  eV) ratio of  $0.2\text{MnO}_2\text{-}0.8$  (LB),  $0.25\text{MnO}_2\text{-}0.75$  (LB) and  $0.3\text{MnO}_2\text{-}0.7$  (LB) samples are (42.14/24.87%, 54.27/12.23%, 56.4/8.34%, respectively). This indicated that  $\text{Mn}^{2+}$  increase with higher Mn content in the glass samples. Moreover, the variation of  $\text{Mn}^{2+}$  have influence to the magnetic and electrochemical properties, as will be discussed later section.

#### 3.3. Optical properties

The study of optical absorption is useful technique which used to understand optical transition and electronic structure of the glasses. The optical absorption spectra of all amorphous glass samples was showed in Fig. 4a. The absorption pattern shows peaks of all samples is in same position. The intensity of absorbance peak is observed to increase with increasing the Mn concentration. Clearly, this indicates the increasing of Mn content in the samples. In general, absorption over the UV and visible regions of the  $\text{Mn}_3\text{O}_4$

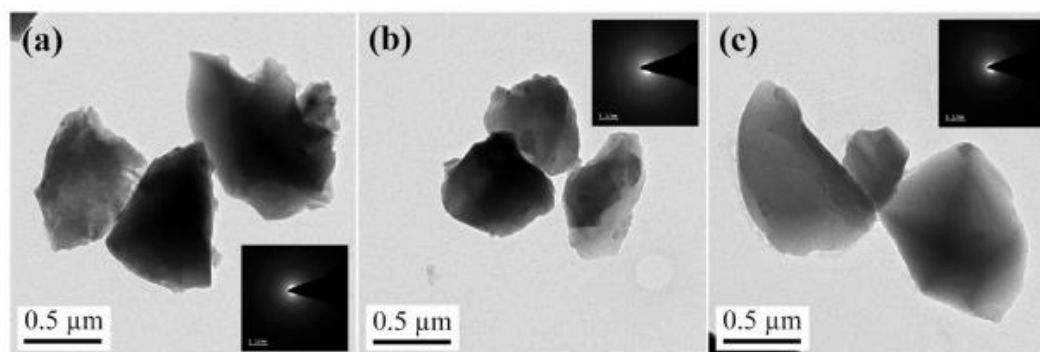


**Fig. 2.** Bright field TEM images and corresponding selected areas electron diffraction (SAED) patterns (inset) of the glass samples: (a)  $0.2\text{MnO}_2\text{-}0.8(\text{Li}_2\text{O-}2\text{B}_2\text{O}_3)$ , (b)  $0.25\text{MnO}_2\text{-}0.75(\text{Li}_2\text{O-}2\text{B}_2\text{O}_3)$ , (c)  $0.3\text{MnO}_2\text{-}0.7(\text{Li}_2\text{O-}2\text{B}_2\text{O}_3)$ .

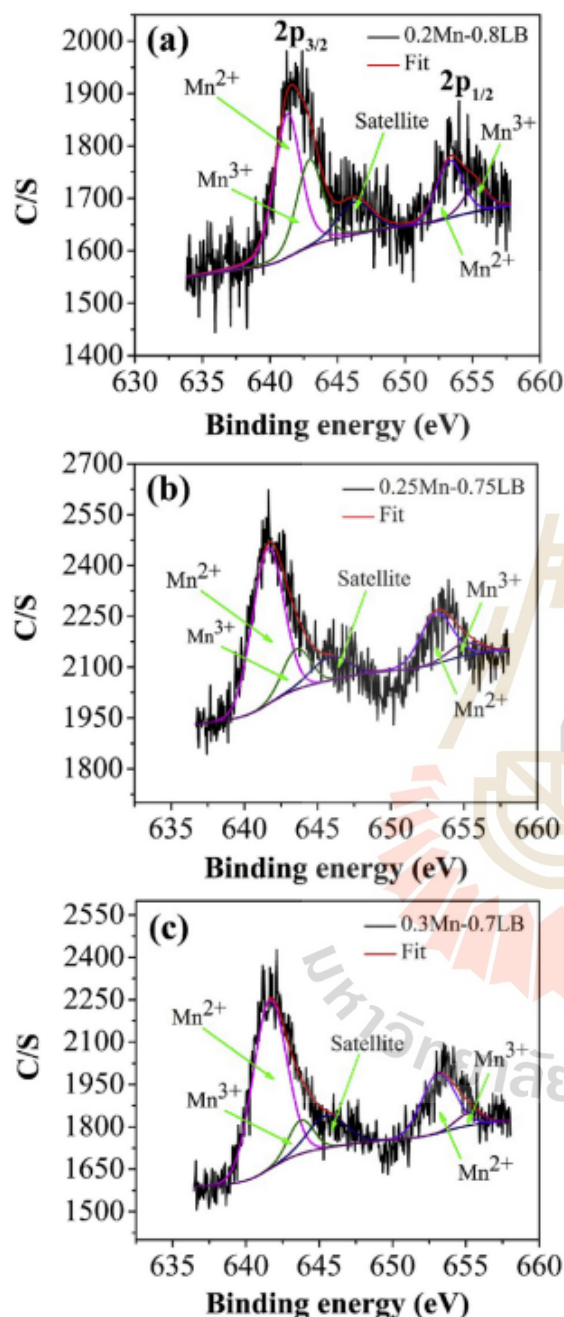


Fig. 3. XPS profiles of glass samples: (a) 0.2MnO<sub>2</sub>-0.8(Li<sub>2</sub>O-2B<sub>2</sub>O<sub>3</sub>), (b) 0.25MnO<sub>2</sub>-0.75(Li<sub>2</sub>O-2B<sub>2</sub>O<sub>3</sub>), (c) 0.3MnO<sub>2</sub>-0.7(Li<sub>2</sub>O-2B<sub>2</sub>O<sub>3</sub>).

reported that the observed optical transitions are identified as the O<sup>2-</sup> → Mn<sup>2+</sup> and O<sup>2-</sup> → Mn<sup>3+</sup> charge transfer transitions at 261 nm and 332 nm [43,45,46], d–d crystal field transition on octahedral Mn<sup>3+</sup> species at 437 nm [43,45]. Moreover, the presence characteristic of Mn<sup>4+</sup> species lead to an electronic transition occur in the region of 440–460 nm [46] in Mn<sub>3</sub>O<sub>4</sub> and 400–450 nm, 575 nm and 705 nm in MnO<sub>2</sub> [47,48]. Therefore, the observed continuous absorptions of manganese-lithium borate glasses at wavelengths

between 200–300 nm and 400–600 nm attributed to charge transfer of Mn<sup>2+</sup> and Mn<sup>3+</sup> and the d–d transition, respectively. This related to the presence of Mn<sup>2+</sup> and Mn<sup>3+</sup> ions in all glass samples, which confirmed by XANES and XPS results. In the glass systems, the glass forming anions effect on the conduction band cations play an indirect band transition [49–51]. The calculated optical transitions of the glass samples are calculated using the transition equation [49–51]:

$$\alpha h\nu = A(h\nu - E_g)^2 \quad (1)$$

where  $\alpha$  is the absorption coefficient,  $h\nu$  is the incident photon energy,  $A$  is constant related to the extent of the band tailing and  $E_g$  is the optical band gap energy for indirect band gap.

The  $E_g$  values are obtained by extrapolating the linear region of the curve to the  $h\nu$  axis of the plot of the  $(\alpha h\nu)^{1/2}$  versus photon energy ( $h\nu$ ) as shown in Fig. 4b–d. The calculated  $E_g$  of the glass samples are slight decrease with increasing of the Mn content.

#### 3.4. Structural analysis using XANES and EXAFS

Fig. 5 reveals normalized XANES spectra of all samples at the Mn K-edges, which compared with those of the standard materials with different Mn oxidation states such as MnO (Mn<sup>2+</sup>), MnO<sub>2</sub> (Mn<sup>4+</sup>), and Mn<sub>2</sub>O<sub>3</sub> (Mn<sup>2+</sup>/Mn<sup>3+</sup>). It was found that the position of the absorption edge at the Mn K-edge of all the samples is similar to Mn<sub>2</sub>O<sub>3</sub> standard samples. Therefore, this indicates that the oxidation state of Mn in the glass samples is mixing between 2+ and 3+.

In order to study the local environment around Mn atoms in glass samples, the EXAFS data of the glass structure were analyzed and fitted. EXAFS spectra of the corresponding fourier transform in R space of are revealed in S.4. The features at Mn K-edge of all samples are similar. The peak position (–1.5 Å) of the main peak corresponds to Mn–O bonding. The parameters of the EXAFS fitting such as interatomic distances (R), model coordination numbers (N), Debye–Waller factors ( $\sigma^2$ ) and amplitude reduction ( $S_0^2$ ) obtained through the different Mn–O bonding distance model, which was used for the first shell fit are shown in Table 1. The slight increasing of interatomic distance of Mn–O with higher Mn content attributed to the smaller atomic radius of Mn<sup>2+</sup> (83 pm) compared to Mn<sup>3+</sup> (64 pm).

#### 3.5. Magnetic properties

Fig. 6 shows the magnetization hysteresis (M – H) loops of the manganese-lithium borate glass samples. The magnetization of all samples depend on linearly on the applied field, which imply that the samples exhibits paramagnetic behaviors. The maximum magnetization at 10000 Oe are 0.175 emu g<sup>-1</sup>, 0.228 emu g<sup>-1</sup> and 0.276 emu g<sup>-1</sup> for 0.2MnO<sub>2</sub>-0.8(Li<sub>2</sub>O-2B<sub>2</sub>O<sub>3</sub>), 0.25MnO<sub>2</sub>-0.75(Li<sub>2</sub>O-2B<sub>2</sub>O<sub>3</sub>) and 0.3MnO<sub>2</sub>-0.7(Li<sub>2</sub>O-2B<sub>2</sub>O<sub>3</sub>) samples, respectively. Generally, the borate-based glasses exhibits the diamagnetic behavior as studied for vanadium borate glasses [38]. In this work, a coexistence of Mn<sup>2+</sup> and Mn<sup>3+</sup> in the glass samples leads to paramagnetism at room-temperature, which similar to in the case of Mn-doped ZnO [52]. Moreover, the increasing of Mn<sup>2+</sup> (high bohr magneton of –5.9 μ<sub>B</sub>) with enhanced Mn content in the surface glass samples confirmed by XPS results may lead to increasing of the magnetization in the glass samples.

#### 3.6. Electrochemical properties

Fig. 7a–c shows the CV curves for the 0.2MnO<sub>2</sub>-0.8(Li<sub>2</sub>O-2B<sub>2</sub>O<sub>3</sub>), 0.25MnO<sub>2</sub>-0.75(Li<sub>2</sub>O-2B<sub>2</sub>O<sub>3</sub>), 0.3MnO<sub>2</sub>-0.7(Li<sub>2</sub>O-2B<sub>2</sub>O<sub>3</sub>) glass

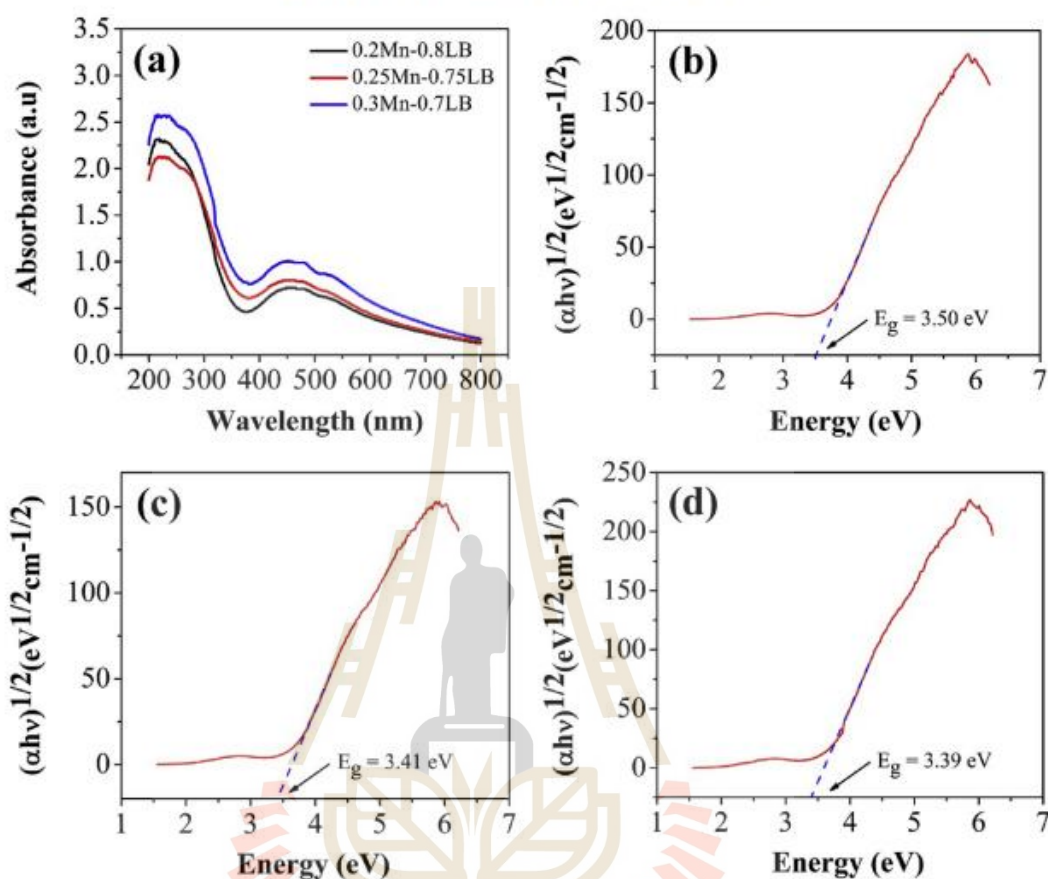


Fig. 4. (a) Optical absorbance spectra of glass samples and Plot of  $(\alpha hv)^{1/2}$  as function of photon energy ( $h\nu$ ) of glass samples: (b)  $0.2\text{MnO}_2\text{-}0.8(\text{Li}_2\text{O-}2\text{B}_2\text{O}_3)$ , (c)  $0.25\text{MnO}_2\text{-}0.75(\text{Li}_2\text{O-}2\text{B}_2\text{O}_3)$ , (d)  $0.3\text{MnO}_2\text{-}0.7(\text{Li}_2\text{O-}2\text{B}_2\text{O}_3)$ .

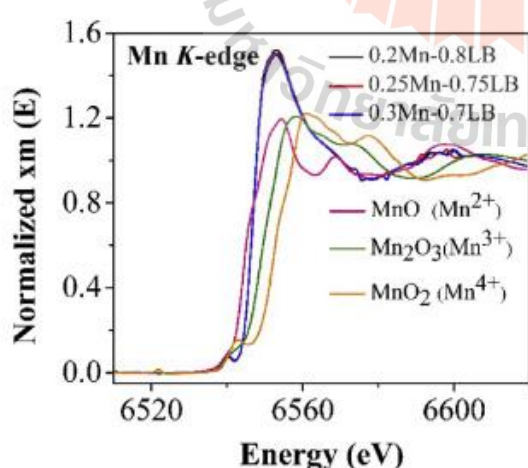


Fig. 5. XANES spectra of Mn K-edge of  $0.2\text{MnO}_2\text{-}0.8(\text{Li}_2\text{O-}2\text{B}_2\text{O}_3)$ ,  $0.25\text{MnO}_2\text{-}0.75(\text{Li}_2\text{O-}2\text{B}_2\text{O}_3)$  and  $0.3\text{MnO}_2\text{-}0.7(\text{Li}_2\text{O-}2\text{B}_2\text{O}_3)$  glass samples and standard samples.

samples at difference scan rates from  $5\text{ mV s}^{-1}$  to  $200\text{ mV s}^{-1}$  in  $6\text{ M KOH}$  electrolyte. The CV curves of all samples reveal the pseudo capacitive behavior with a pair of redox peak which consist of the anodic peak of oxidation process (charging) around  $0.35\text{--}0.45\text{ V}$  and the cathodic peak of reduction process (discharging) around  $0.08\text{--}0.14\text{ V}$ . The shape and redox potentials of the CV curves in our work are comparable to those manganese oxide ( $\text{Mn}_3\text{O}_4$ ) in  $\text{KOH}$  electrolyte which reported by Shah et al. [53]. Therefore, the redox peaks of the material attributed to the redox transitions of various Mn oxidation states (i.e.,  $\text{Mn}^{2+}$  and  $\text{Mn}^{3+}$ ). The peak current shifted with enhanced scan rates which attributed to the resistance of the electrode [54]. Moreover, the current response of the glass electrodes enhanced with increasing of scan rates. The specific capacitance of the cyclic voltammetry measurement ( $C_{CV}$ ) of the electrodes are calculated by using the relation [55,56]:

$$C_{CV} = \frac{1}{vm\Delta V} \int IdV \quad (2)$$

where  $I$  is the response current (A),  $v$  is the scan rate ( $\text{mV s}^{-1}$ ),  $m$  is the mass of the active materials (g), and  $\Delta V$  is the potential window (V).

The calculated specific capacitances of the  $x\text{MnO}_2\text{-(}1-x\text{)(Li}_2\text{O-}2\text{B}_2\text{O}_3)$  glass sample calculated from the area of CV curve at scan

**Table 1**

EXAFS fitting parameters including interatomic distances (R), coordination numbers (N), Debye–Waller factors ( $\sigma^2$ ) and amplitude reduction ( $S_0^2$ ) of 0.2MnO<sub>2</sub>-0.8(Li<sub>2</sub>O-2B<sub>2</sub>O<sub>3</sub>), 0.25MnO<sub>2</sub>-0.75(Li<sub>2</sub>O-2B<sub>2</sub>O<sub>3</sub>) and 0.3MnO<sub>2</sub>-0.7(Li<sub>2</sub>O-2B<sub>2</sub>O<sub>3</sub>) glass samples.

Samples	Paths	$S_0^2$	N	$\sigma^2$	$E_0$	$\Delta R$	$R_{\text{eff}}$	R
0.20Mn-0.8LB	Mn-O	1	3.019	0.01169	-1.251	-0.01476	2.10000	2.08524
0.25Mn-0.75LB	Mn-O	1	2.989	0.01169	-1.251	-0.01377	2.10000	2.08623
0.30Mn-0.7LB	Mn-O	1	2.911	0.01169	-1.251	-0.01155	2.10000	2.08845

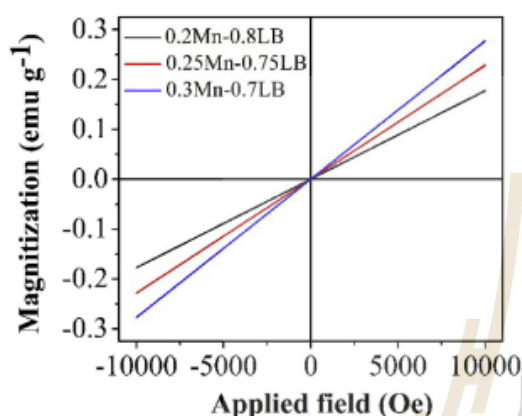


**Fig. 6.** Magnetization hysteresis (M–H) loops of 0.2MnO<sub>2</sub>-0.8(Li<sub>2</sub>O-2B<sub>2</sub>O<sub>3</sub>), 0.25MnO<sub>2</sub>-0.75(Li<sub>2</sub>O-2B<sub>2</sub>O<sub>3</sub>) and 0.3MnO<sub>2</sub>-0.7(Li<sub>2</sub>O-2B<sub>2</sub>O<sub>3</sub>) glass samples.

rate 200–5 mV s<sup>-1</sup> are increase (32.40–99.36 F g<sup>-1</sup>, 41.85–181.82 F g<sup>-1</sup> and 48.55–187.50 F g<sup>-1</sup>) with increasing of Mn content for  $x = 0.2, 0.25$  and  $0.3$  samples, respectively. Interestingly, the specific capacitance of  $x = 0.25$  and  $x = 0.3$  samples is higher than  $x = 0.2$  sample about 2 time. Clearly, the improving of the specific capacitance attribute to the higher redox reaction of Mn oxidation state. This correspond to increasing of the Mn<sup>2+</sup> with higher Mn content, which confirmed from XPS. This results demonstrated that the electrochemical reaction may occur at the surface of the glass samples. The specific capacitance values of all the electrodes at low scan rates are higher than these at high scan rates as shown in Fig. 7d. This attributed to the glass samples exhibited good pseudocapacitive behavior and sufficient time of ions to arrive the electrode surface for electrochemical reactions at lower scan rate and diffusion limitations at higher scan rates [55,57,58].

The specific capacitance of the galvanostatic charge-discharge measurements ( $C_{\text{GCD}}$ ) of the electrodes was calculated using the equation [55,57,59]:

$$C_{\text{GCD}} = \frac{I \Delta t}{m \Delta V} \quad (3)$$

where  $I$  is the discharge current (A),  $\Delta t$  is the discharge time,  $m$  is the mass of the active materials (g) and  $\Delta V$  is the potential window (V).

Moreover, the energy density ( $E$ ) and the power density ( $P$ ) for the electrodes was calculated by the following equations [57,60]:

$$E(\text{Wh Kg}^{-1}) = \frac{C_{\text{GCD}} \Delta V^2}{7.2} \quad (4)$$

$$P(\text{W Kg}^{-1}) = \frac{E \times 3600}{t} \quad (5)$$

where  $C_{\text{GCD}}$  is the specific capacitance calculated from charge-discharge measurement (F g<sup>-1</sup>),  $\Delta V$  is the potential window (V) and  $t$  is the discharge time (s).

Galvanostatic charge-discharge curves of the glass electrodes at different current densities are shown in Fig. 8a–c. The curves of all samples are not ideal straight lines which indicate a redox reaction process of the electrodes. The calculated specific capacitance is 12.55–85.10 F g<sup>-1</sup> for 0.2Mn-0.8LB, 24.36–162.35 F g<sup>-1</sup> for 0.25Mn-0.75LB and 32.68–169.66 F g<sup>-1</sup> for 0.3Mn-0.7LB at current densities of 20–1 A g<sup>-1</sup>, respectively. The increasing of Mn content and decreasing of current densities exhibited the increasing of the specific capacitance as shown in Fig. 8d. Moreover, the enhanced capacitive performance of the electrodes was attributed to high theoretical specific capacitance of manganese oxide materials (-1370–1400 F g<sup>-1</sup>) [21,22].

Fig. 9a shows the ragone plot with respect to specific energy and specific power density of the electrodes at various current densities. The 0.2MnO<sub>2</sub>-0.8(Li<sub>2</sub>O-2B<sub>2</sub>O<sub>3</sub>), 0.25MnO<sub>2</sub>-0.75(Li<sub>2</sub>O-2B<sub>2</sub>O<sub>3</sub>) and 0.3MnO<sub>2</sub>-0.7(Li<sub>2</sub>O-2B<sub>2</sub>O<sub>3</sub>) glass electrodes exhibits the power density of 455.92–18325, 452.75–17240, 452.95–16523 W K g<sup>-1</sup> at 20–1 A g<sup>-1</sup>, respectively, which decrease when enhanced the current density. Moreover, the power density is slightly decrease with increasing of the Mn content at the same current density. Interestingly, with increasing of the current density and Mn content, the energy density can improve about 2 time from 5.73 to 9.83 for 0.2 M to 9.97–18.49 for 0.25 M and slightly increase to 11.02–19.34 Wh K g<sup>-1</sup> for 0.3 M at 1–20 A g<sup>-1</sup>, respectively. This results suggest that the manganese-lithium-borate glass electrodes with high power and energy density can be capable supercapacitor in promising energy storage application.

The long cyclic stability of the active materials is an important requirement for the supercapacitor applications. The capacity retention plots of the manganese-lithium-borate glass electrodes at a current density of 2 A g<sup>-1</sup> is shown in Fig. 8b. After 1000 continuous charge-discharge cycles, the capacity retention of 0.2MnO<sub>2</sub>-0.8(Li<sub>2</sub>O-2B<sub>2</sub>O<sub>3</sub>), 0.25MnO<sub>2</sub>-0.75(Li<sub>2</sub>O-2B<sub>2</sub>O<sub>3</sub>) and 0.3MnO<sub>2</sub>-0.7(Li<sub>2</sub>O-2B<sub>2</sub>O<sub>3</sub>) glass samples maintains 40.46, 70.59 and 76.05%, respectively of the initial capacitance. Interestingly, the increasing of the Mn content at 0.25 M and 0.3 M enhanced the capacity retention about 2 time that of the 0.2 M. The enhanced capacity retention of glass electrodes was attributed to the good stability nature of manganese oxide-based material [26,61].

In comparison with the previously reported carbon or manganese oxide-based electrodes, the maximum specific capacitances of the 0.3MnO<sub>2</sub>-0.7(Li<sub>2</sub>O-2B<sub>2</sub>O<sub>3</sub>) glass in this work (187 F g<sup>-1</sup>) are in the range of activated carbon (210 F g<sup>-1</sup>) [62], graphene-activated carbon composite (205 F g<sup>-1</sup>) [63], carbon nanotube (180 F g<sup>-1</sup>) [64], Mn<sub>3</sub>O<sub>4</sub> (190 F g<sup>-1</sup>) [65], graphene/Mn<sub>3</sub>O<sub>4</sub> composites (140 F g<sup>-1</sup>) [65] in KOH electrolyte, graphene/MnO<sub>2</sub> composite (328 F g<sup>-1</sup>) [66] in KCl electrolyte and activated carbons/Mn<sub>3</sub>O<sub>4</sub>-carbon black (154 F g<sup>-1</sup>) in Na<sub>2</sub>SO<sub>4</sub> electrolyte [67]. However, the maximum energy density of the 0.3MnO<sub>2</sub>-0.7(Li<sub>2</sub>O-2B<sub>2</sub>O<sub>3</sub>) glass

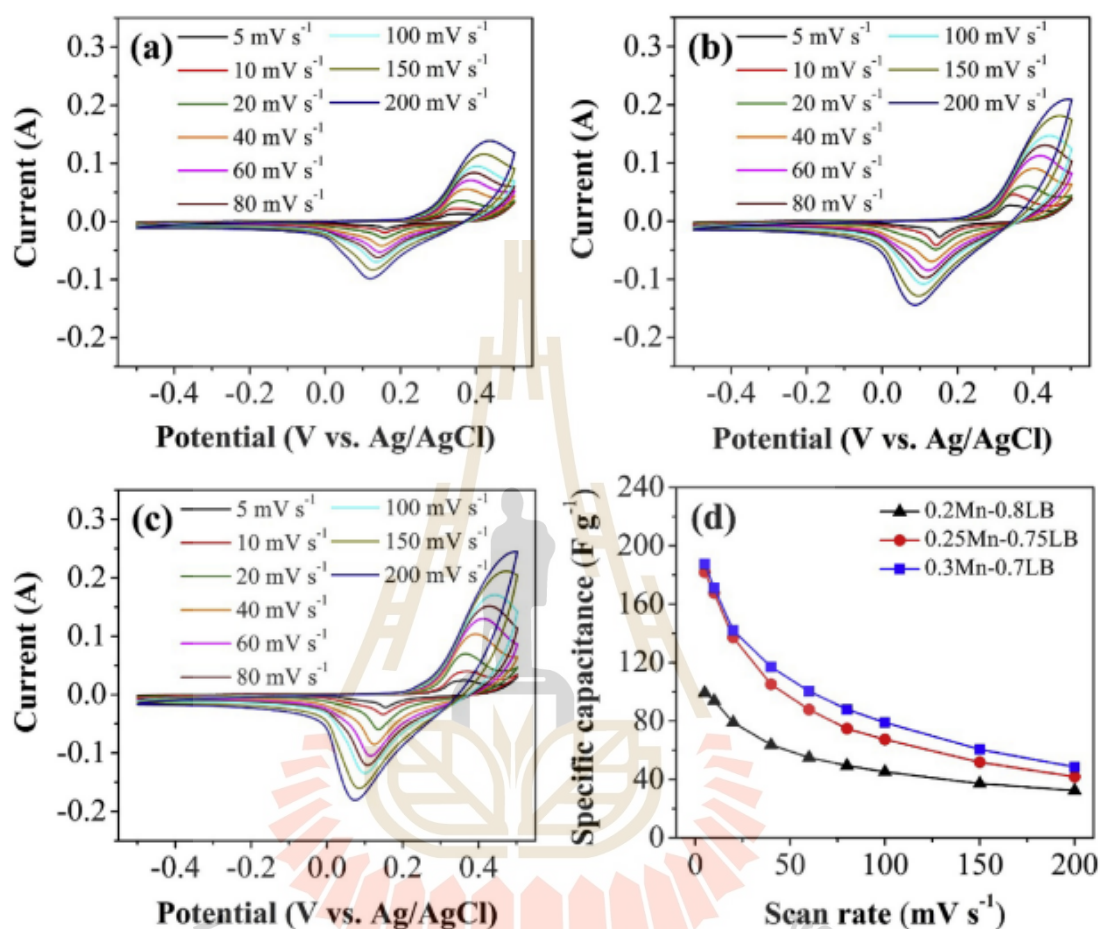


Fig. 7. Cyclic voltammograms of (a)  $0.2\text{MnO}_2\text{-}0.8(\text{Li}_2\text{O-}2\text{B}_2\text{O}_3)$ , (b)  $0.25\text{MnO}_2\text{-}0.75(\text{Li}_2\text{O-}2\text{B}_2\text{O}_3)$ , (c)  $0.3\text{MnO}_2\text{-}0.7(\text{Li}_2\text{O-}2\text{B}_2\text{O}_3)$  glass electrodes s at different scan rates (d) plots of specific capacitance versus scan rates.

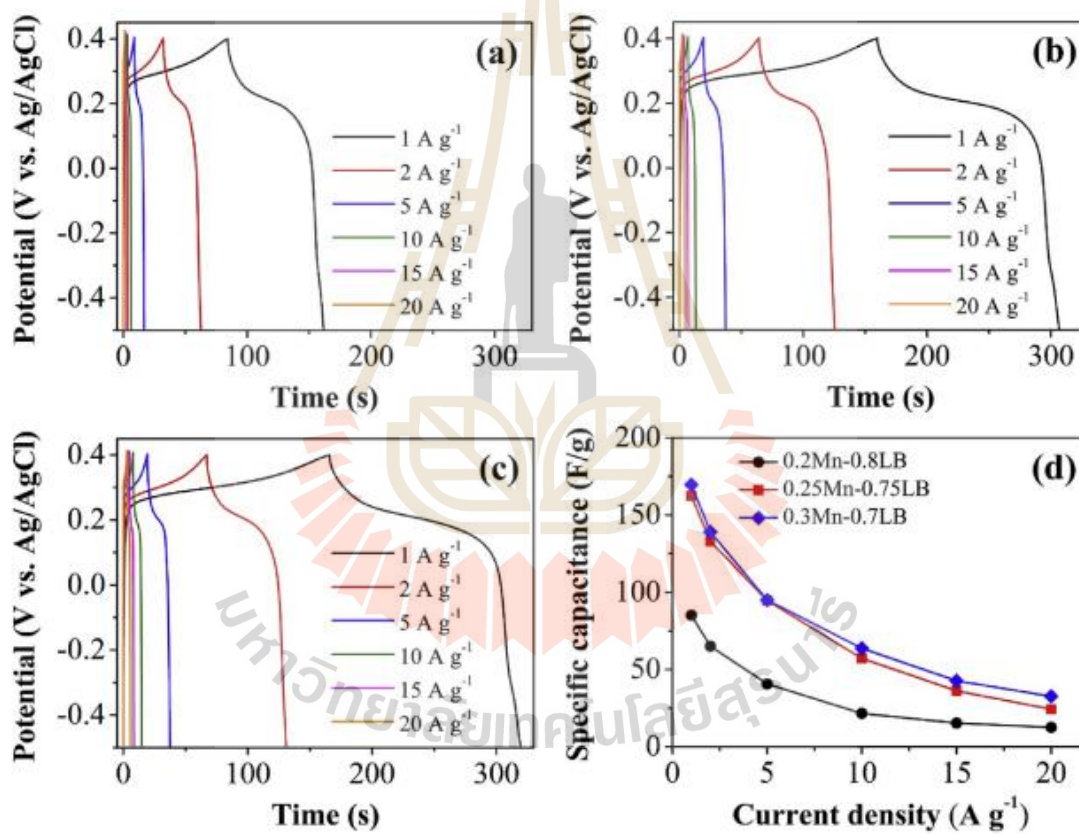
( $\sim 19 \text{ Wh Kg}^{-1}$ ) is higher than the graphene-activated carbon composite [63], carbon nanotube [64] ( $\sim 6 \text{ Wh Kg}^{-1}$ ) and graphene/ $\text{MnO}_2$  composite ( $\sim 11 \text{ Wh Kg}^{-1}$ ) [66]. Therefore, this imply that the manganese-lithium borate glass can be good candidate as potential composite material with carbon for hybrid supercapacitor and their applications.

Fig. 9c shows the Nyquist plots of the glass electrodes in 6M KOH. All samples shows almost similar profiles. The electrolyte resistance ( $R_s$ ) can be obtained from the intercept at the real axis ( $Z'$ ) at a high frequency. The  $R_s$  values are  $1.05\Omega$ ,  $0.67\Omega$  and  $0.56\Omega$  for  $0.2\text{MnO}_2\text{-}0.8(\text{Li}_2\text{O-}2\text{B}_2\text{O}_3)$ ,  $0.25\text{MnO}_2\text{-}0.75(\text{Li}_2\text{O-}2\text{B}_2\text{O}_3)$  and  $0.3\text{MnO}_2\text{-}0.7(\text{Li}_2\text{O-}2\text{B}_2\text{O}_3)$  electrodes, respectively. The slight decreasing of  $R_s$  cause reduction of a combination of ion resistance of electrolyte, intrinsic resistance of substrate and contact resistance at the active material/current collector [68]. Moreover, the curves at low frequency tend to the imaginary axis ( $Z''$ ) indicate the improving perfectly capacitive of an ideal capacitor with low diffusion resistance of ions in the structure of the electrodes [55,69,70]. Therefore, the decreasing of  $R_s$  values and the tendency of the curves with increasing Mn content slightly closed to ideal

capacitor may cause the improving of the specific capacitance of the glass samples.

#### 4. Conclusions

In this study, the  $x\text{MnO}_2\text{-(}1-x\text{)(Li}_2\text{O-}2\text{B}_2\text{O}_3)$  glasses where  $x = 0.2, 0.25$  and  $0.3$  were successfully prepared by conventional melt-quench technique. The structures and morphologies of all the samples were characterized by XRD, SEM, TEM, XAS and XPS techniques. The XANES results confirmed that Mn oxidation states in the glass samples is mixing between  $2+$  and  $3+$ . The XPS analysis found that the tendency of  $\text{Mn}^{2+}$  at surface of the samples slightly increases with an increase of Mn content. The magnetic properties of the samples were observed. All samples exhibits the paramagnetic behavior. The enhancement of magnetization attributed to the increasing of Mn content. The electrochemical properties of the electrode material was studied in the 6M KOH electrolyte. All glass samples exhibits the pseudo capacitive behavior with redox reaction of  $\text{Mn}^{2+}$  and  $\text{Mn}^{3+}$ . The effects of increasing of the Mn content can improve of the electrochemical



**Fig. 8.** Galvanostatic charge-discharge curves of (a)  $0.2\text{MnO}_2\text{-}0.8(\text{Li}_2\text{O}\cdot 2\text{B}_2\text{O}_3)$ , (b)  $0.25\text{MnO}_2\text{-}0.75(\text{Li}_2\text{O}\cdot 2\text{B}_2\text{O}_3)$ , (c)  $0.3\text{MnO}_2\text{-}0.7(\text{Li}_2\text{O}\cdot 2\text{B}_2\text{O}_3)$  glass electrodes at different scan rates, (d) plots of specific capacitance versus the current density.

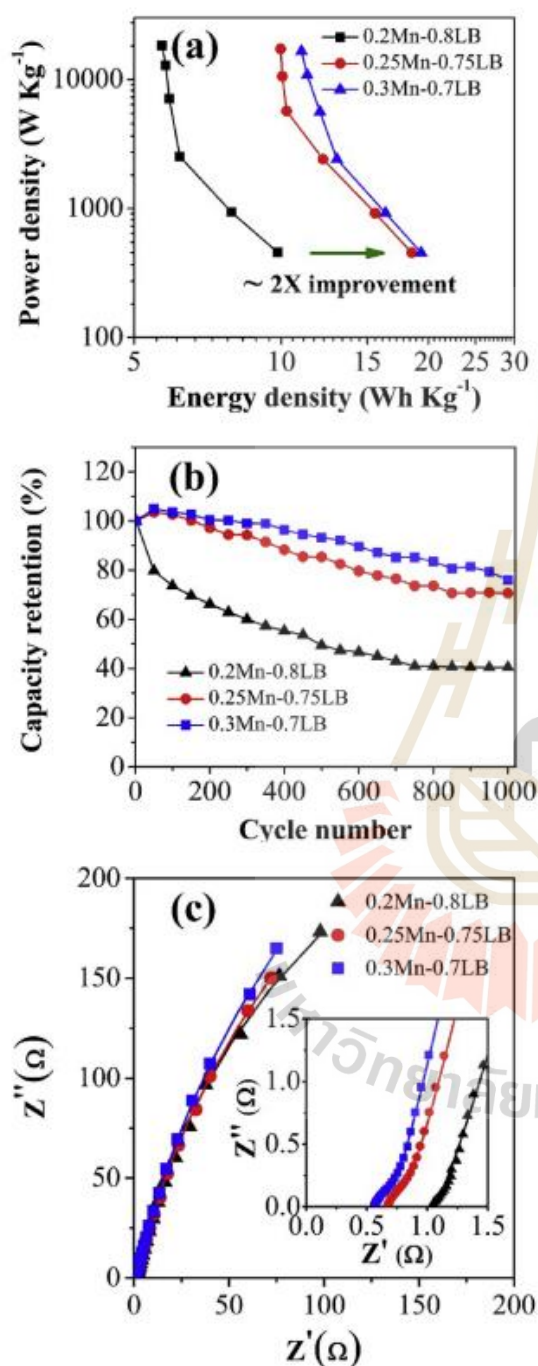


**Fig. 9.** (a) Ragone plot, (b) the capacity retention (%) during long-term cycling and (c) the Nyquist plots of the  $0.2\text{MnO}_2\text{-}0.8(\text{Li}_2\text{O-}2\text{B}_2\text{O}_3)$ ,  $0.25\text{MnO}_2\text{-}0.75(\text{Li}_2\text{O-}2\text{B}_2\text{O}_3)$  and  $0.3\text{MnO}_2\text{-}0.7(\text{Li}_2\text{O-}2\text{B}_2\text{O}_3)$  glass electrodes.

performances. The highest specific capacitance ( $187.05\text{ F g}^{-1}$  for CV and  $169.66\text{ F g}^{-1}$  for GCD), specific energy density ( $19.34\text{ Wh kg}^{-1}$ ) and capacity retention (76.05%) after 1000 cycles is observed for the

$0.3\text{MnO}_2\text{-}0.7(\text{Li}_2\text{O-}2\text{B}_2\text{O}_3)$  electrode. Clearly, the EIS results confirmed that a combination of ion resistance of electrolyte, intrinsic resistance of substrate and contact resistance at the active material/current collector are decrease with the increasing of Mn content. This cause the improving of perfectly capacitive of an ideal capacitor, the specific capacitance and the capacity retention of the glass samples. Therefore, the manganese-lithium borate glasses is a promising electrode material for supercapacitor applications.

#### Acknowledgments

The authors gratefully acknowledge the Synchrotron Light Research Institute (Public Organization) (BL5.2 and BL5.3), Thailand for the XAS and XPS facilities. Many thanks to Department of Physics, Khon Kaen University for VSM facilities and School of Physics and Center of Excellent on Advanced Functional Materials (CoE-AFM), Suranaree University of Technology for laboratory facilities.

#### Appendix A. Supplementary data

Supplementary data related to this article can be found at <https://doi.org/10.1016/j.jallcom.2018.05.300>.

#### References

- [1] C. Xiong, T. Li, T. Zhao, A. Dang, H. Li, X. Ji, W. Jin, S. Jiao, Y. Shang, Y. Zhang, Reduced graphene oxide-carbon nanotube grown on carbon fiber as binder-free electrode for flexible high-performance fiber supercapacitors, *Compos. B Eng.* 116 (2017) 7–15.
- [2] C. Xiong, T. Li, A. Dang, T. Zhao, H. Li, H. Lv, Two-step approach of fabrication of three-dimensional  $\text{MnO}_2$ -graphene-carbon nanotube hybrid as a binder-free supercapacitor electrode, *J. Power Sources* 306 (2016) 602–610.
- [3] C. Xiong, T. Li, M. Khan, H. Li, T. Zhao, A three-dimensional  $\text{MnO}_2$ /graphene hybrid as a binder-free supercapacitor electrode, *RSC Adv.* 5 (2015) 85613–85619.
- [4] C. Xiong, T. Li, T. Zhao, A. Dang, X. Ji, H. Li, M. Etesami, Three-dimensional graphene/ $\text{MnO}_2$  nanowalls hybrid for high-efficiency electrochemical supercapacitors, *Nano* 13 (2018), 1850013.
- [5] C. Xiong, T. Li, T. Zhao, Y. Shang, A. Dang, X. Ji, H. Li, J. Wang, Two-step approach of fabrication of three-dimensional reduced graphene oxide-carbon nanotubes-nickel foams hybrid as a binder-free supercapacitor electrode, *Electrochim. Acta* 217 (2016) 9–15.
- [6] C. Xiong, T. Li, Y. Zhu, T. Zhao, A. Dang, H. Li, X. Ji, Y. Shang, M. Khan, Two-step approach of fabrication of interconnected nanoporous 3D reduced graphene oxide-carbon nanotube-polyaniline hybrid as a binder-free supercapacitor electrode, *J. Alloys Compd.* 695 (2017) 1248–1259.
- [7] T. Zhao, X. Ji, P. Bi, W. Jin, C. Xiong, A. Dang, H. Li, T. Li, S. Shang, Z. Zhou, In situ synthesis of interconnected three-dimensional graphene foam/polyaniline nanorod supercapacitor, *Electrochim. Acta* 230 (2017) 342–349.
- [8] D. Yan, Z. Guo, G. Zhu, Z. Yu, H. Xu, A. Yu,  $\text{MnO}_2$  film with three-dimensional structure prepared by hydrothermal process for supercapacitor, *J. Power Sources* 199 (2012) 409–412.
- [9] D. Yan, H. Zhang, L. Chen, G. Zhu, S. Li, H. Xu, A. Yu, Biomorphic synthesis of mesoporous  $\text{Co}_3\text{O}_4$  microtubules and their pseudocapacitive performance, *ACS Appl. Mater. Interfaces* 6 (2014) 15632–15637.
- [10] D. Yan, H. Zhang, S. Li, G. Zhu, Z. Wang, H. Xu, A. Yu, Formation of ultrafine three-dimensional hierarchical birnessite-type  $\text{MnO}_2$  nanoflowers for supercapacitor, *J. Alloys Compd.* 607 (2014) 245–250.
- [11] S. Lu, D. Yan, L. Chen, G. Zhu, H. Xu, A. Yu, One-pot fabrication of hierarchical  $\text{Ag}/\text{MnO}_2$  nanoflowers for electrochemical capacitor electrodes, *Mater. Lett.* 168 (2016) 40–43.
- [12] J. Zhou, J. Lian, L. Hou, J. Zhang, H. Gou, M. Xia, Y. Zhao, T.A. Strobel, L. Tao, F. Gao, Ultrahigh volumetric capacitance and cyclic stability of fluorine and nitrogen co-doped carbon microspheres, *Nat. Commun.* 6 (2015) 8503.
- [13] Y. Qiao, H. Wang, X. Zhang, P. Jia, T. Shen, X. Hao, Y. Tang, X. Wang, W. Gao, L. Kong, Ultrahigh volumetric capacitance biomorphic porous carbon material derived from mold, *Mater. Lett.* 184 (2016) 252–256.
- [14] B. Conway, *Electrochemical Supercapacitors: Scientific Fundamentals and Technological Applications*, Kluwer-Plenum, New York, 1999.
- [15] P. Simon, Y. Gogotsi, Materials for electrochemical capacitors, *Nat. Mater.* 7 (2008) 845–854.
- [16] C. Lokhande, D. Dubal, O.S. Joo, Metal oxide thin film based supercapacitors, *Curr. Appl. Phys.* 11 (2011) 255–270.
- [17] G. Zhao, N. Zhang, K. Sun, Porous  $\text{MoO}_3$  films with ultra-short relaxation time used for supercapacitors, *Mater. Res. Bull.* 48 (2013) 1328–1332.
- [18] V.V. Obreja, A. Dinescu, A.C. Obreja, Activated carbon based electrodes in

- commercial supercapacitors and their performance, *Int. Rev. Electr. Eng.* 5 (2010) 272–282.
- [19] K.I. Ozoemena, S. Chen, *Nanomaterials in Advanced Batteries and Supercapacitors*, Springer, 2016.
- [20] C.C. Hu, W.C. Chen, Effects of substrates on the capacitive performance of  $\text{RuO}_2 \cdot n\text{H}_2\text{O}$  and activated carbon-RuO<sub>2</sub> electrodes for supercapacitors, *Electrochim. Acta* 49 (2004) 3469–3477.
- [21] Z. Qi, A. Younis, D. Chu, S. Li, A facile and template-free one-pot synthesis of  $\text{Mn}_3\text{O}_4$  nanostructures as electrochemical supercapacitors, *Nano-Micro Lett.* 8 (2016) 165–173.
- [22] M. Toupin, T. Brousse, D. Belanger, Charge storage mechanism of  $\text{MnO}_2$  electrode used in aqueous electrochemical capacitor, *Chem. Mater.* 16 (2004) 3184–3190.
- [23] S. Kulkarni, D. Puthusseri, S. Thakur, A. Banpurkar, S. Patil, Hausmannite manganese oxide cathodes for supercapacitors: surface wettability and electrochemical properties, *Electrochim. Acta* 231 (2017) 460–467.
- [24] H. Jiang, T. Zhao, C. Yan, J. Ma, C. Li, Hydrothermal synthesis of novel  $\text{Mn}_3\text{O}_4$  nano-octahedrons with enhanced supercapacitors performances, *Nanoscale* 2 (2010) 2195–2198.
- [25] Z. Hu, L. Zu, Y. Jiang, H. Lian, Y. Liu, Z. Li, F. Chen, X. Wang, X. Cui, High specific capacitance of polyaniline/mesoporous manganese dioxide composite using  $\text{KH}_2\text{SO}_4$  electrolyte, *Polymers* 7 (2015) 1939–1953.
- [26] P.A. Shinde, V.C. Lokhande, A.M. Patil, A.A. Yadav, C.D. Lokhande, Hydrothermal synthesis of manganese oxide thin films using different oxidizing agents for supercapacitor application, *Int. J. Eng.* 10 (2017) 532–537.
- [27] H. Yu, H. Zhou, High-energy cathode materials ( $\text{Li}_2\text{MnO}_3$ – $\text{LiMO}_2$ ) for lithium-ion batteries, *J. Phys. Chem. Lett.* 4 (2013) 1268–1280.
- [28] S. Afyon, F. Krumeich, C. Mensing, A. Borgschulte, R. Nesper, New high capacity cathode materials for rechargeable Li-ion batteries: vanadate-borate glasses, *Sci. Rep.* 4 (2014) 7113.
- [29] S.S. Gundale, A. Deshpande, Improvement of ionic conductivity in  $\text{Li}_3\text{S}_2\text{O}_6\text{V}_x\text{O}_4$  ceramic inorganic electrolyte by addition of  $\text{LiBO}_2$  glass for Li ion battery application, *Electrochim. Acta* 265 (2018) 65–70.
- [30] D. Ramteke, H. Swart, R. Gedam, Electrical characterization of  $\text{Pr}^{3+}$  containing lithium borate glasses by impedance spectroscopy, *Adv. Mater.* 7 (2016) 436–440.
- [31] D. Ramteke, H. Swart, R. Gedam, Electrochemical response of  $\text{Nd}^{3+}$  ions containing lithium borate glasses, *J. Rare Earths* 35 (2017) 480–484.
- [32] V. Kundu, R. Dhiman, D. Goyal, A. Maan, Physical and electrical properties of semiconducting  $\text{Fe}_2\text{O}_3$ – $\text{V}_2\text{O}_5$ – $\text{B}_2\text{O}_3$  glasses, *Optoelectron. Adv. Mat.* 2 (2008), 428432.
- [33] K. Padmasree, D. Kanchan, Modulus studies of  $\text{CdI}_2$ – $\text{Ag}_2\text{O}$ – $\text{V}_2\text{O}_5$ – $\text{B}_2\text{O}_3$  system, *Mater. Sci. Eng. B* 122 (2005) 24–28.
- [34] S. Khasa, V. Seth, S. Gupta, R.M. Krishna, EPR and DSC study of  $\text{M}_2\text{O} \cdot \text{V}_2\text{O}_5 \cdot \text{B}_2\text{O}_3$  (M = Li, Na or K) glasses, *Phys. Chem. Glasses* 40 (1999) 269–272.
- [35] I. Kashif, A. Sanad, Y. Abo-Zeid, Study of some physical properties of the  $\text{V}_2\text{O}_5$ – $\text{B}_2\text{O}_3$ – $\text{P}_2\text{O}_5$ – $\text{Fe}_2\text{O}_3$  glass system, *Phys. Chem. Glasses* 31 (1990) 196–198.
- [36] E. Culea, A. Nicula, Electrical properties of  $\text{V}_2\text{O}_5$ – $\text{B}_2\text{O}_3$  glasses, *Solid State Commun.* 58 (1986) 545–549.
- [37] B. Sharma, D. Dube, A. Mansingh, Preparation and characterisation of  $\text{V}_2\text{O}_5$ – $\text{B}_2\text{O}_3$  glasses, *J. Non-Cryst. Solids* 65 (1984) 39–51.
- [38] N. Laorodphan, P. Pooddee, P. Kidkhunthod, P. Kunthadee, W. Tapala, R. Puntharod, Boron and pentavalent vanadium local environments in binary vanadium borate glasses, *J. Non-Cryst. Solids* 433 (2016) 118–124.
- [39] M. Pal, B. Roy, M. Pal, Structural characterization of borate glasses containing zinc and manganese oxides, *J. Mod. Phys.* 2 (2011) 1062–1066.
- [40] A. Kajinami, T. Kotake, S. Deki, S. Kohara, The structural analysis of manganese borate glass by high-energy X-ray diffraction measurement, *Nucl. Instrum. Meth. Phys. Res. B* 199 (2003) 34–37.
- [41] P. Kidkhunthod, Structural studies of advanced functional materials by synchrotron-based x-ray absorption spectroscopy: BL5.2 at SLRI, Thailand, *Adv. Nat. Sci.: Nanosci. Nanotech.* 8 (2017), 035007.
- [42] W. Klysubun, P. Kidkhunthod, P. Tarawarakarn, P. Sombunchoo, C. Kongmark, S. Limpjumnong, S. Rujirawat, R. Yimnirun, G. Tumcharern, K. Faungnawakij, SUT-NANOTEC-SLRI beamline for X-ray absorption spectroscopy, *J. Synchrotron. Rad.* 24 (2017) 707–716.
- [43] V.C. Bose, V. Biju, Optical, electrical and magnetic properties of nanostructured  $\text{Mn}_3\text{O}_4$  synthesized through a facile chemical route, *Physica. E Low. Dimens. Syst. Nanostruct.* 66 (2015) 24–32.
- [44] A.M.E. Raj, S.G. Victoria, V.B. Jothy, C. Ravidhas, J. Wollschlager, M. Suendorf, M. Neumann, M. Jayachandran, C. Sanjeeviraja, XRD and XPS characterization of mixed valence  $\text{Mn}_3\text{O}_4$  hausmannite thin films prepared by chemical spray pyrolysis technique, *Appl. Surf. Sci.* 256 (2010) 2920–2926.
- [45] J.B. Macstre, E.F. López, J. Gallardo-Amores, R.R. Casero, V.S. Escribano, E.P. Bernal, Influence of tile synthesis parameters on the structural and textural properties of precipitated manganese oxides, *Int. J. Inorg. Mater.* 3 (2001) 889–899.
- [46] X. Hao, J. Zhao, Y. Li, Y. Zhao, D. Ma, L. Li, Mild aqueous synthesis of octahedral  $\text{Mn}_3\text{O}_4$  nanocrystals with varied oxidation states, *Colloids. Surf. A Physicochem. Eng. Asp.* 374 (2011) 42–47.
- [47] M. Baldi, F. Milella, J.M. Gallardo-Amores, A study of Mn-Ti oxide powders and their behaviour in propane oxidation catalysis, *J. Mater. Chem.* 8 (1998) 2525–2531.
- [48] M. Valigi, A. Cimino, The system  $\text{TiO}_2$ – $\text{Mn}_2\text{O}_3$ : a structural, the thermogravimetric, and magnetic study, *J. Solid State Chem.* 12 (1975) 135–143.
- [49] S.S. Sastry, Structural and optical properties of vanadium doped alkaline earth lead zinc phosphate glasses, *Indian. J. Pure. Ap. Phys.* 52 (2015) 491–498.
- [50] C. Dayanand, R. Sarma, G. Bhikshamaiah, M. Salagram, Optical properties of lead phosphate glasses, *J. Non-Cryst. Solids* 167 (1994) 122–126.
- [51] A. Abdelghany, A.H. Hammad, Spectrochim. Impact of vanadium ions in barium borate glass, *Acta. A Mol. Biomol. Spectrosc.* 137 (2015) 39–44.
- [52] T.L. Phan, P. Zhang, D. Yang, N. Nghia, S. Yu, Local structure and paramagnetic properties of  $\text{Zn}_{1-x}\text{Mn}_x\text{O}$ , *J. Appl. Phys.* 110 (2011), 063912.
- [53] H.U. Shah, F. Wang, A.M. Toufiq, A.M. Khattak, A. Iqbal, Z.A. Ghazi, S. Ali, X. Li, Z. Wang, Electrochemical properties of single-crystalline  $\text{Mn}_3\text{O}_4$  nanostructures and their capacitive performance in basic electrolyte, *Int. J. Electrochem. Sci.* 11 (2016) 8155–8162.
- [54] Y.G. Wang, H.Q. Li, Y.Y. Xia, Ordered whisker like polyaniline grown on the surface of mesoporous carbon and its electrochemical capacitance performance, *Adv. Mater.* 18 (2006) 2619–2623.
- [55] J. Khajonrit, U. Wongpratat, P. Kidkhunthod, S. Pinitsoontorn, S. Maensiri, Effects of Co doping on magnetic and electrochemical properties of  $\text{BiFeO}_3$  nanoparticles, *J. Magn. Magn. Mater.* 449 (2018) 423–434.
- [56] J. Yan, J. Liu, Z. Fan, T. Wei, L. Zhang, High-performance supercapacitor electrodes based on highly corrugated graphene sheets, *Carbon* 50 (2012) 2179–2188.
- [57] R.K. Gupta, J. Candler, S. Palchoudhury, K. Ramasamy, B.K. Gupta, Flexible and high performance supercapacitors based on  $\text{NiCo}_2\text{O}_4$  for wide temperature range applications, *Sci. Rep.* 5 (2015) 15265.
- [58] B. Sarma, A.L. Jurovitzki, Y.R. Smith, S.K. Mohanty, M. Misra, Redox-induced enhancement in interfacial capacitance of the titania nanotube/bismuth oxide composite electrode, *ACS Appl. Mater. Interfaces* 5 (2013) 1688–1697.
- [59] J. Gomez, E.E. Kalu, High-performance binder-free Co-Mn composite oxide supercapacitor electrode, *J. Power Sources* 230 (2013) 218–224.
- [60] C. Xiang, M. Li, M. Zhi, A. Manivannan, N. Wu, A reduced graphene oxide/ $\text{Co}_3\text{O}_4$  composite for supercapacitor electrode, *J. Power Sources* 226 (2013) 65–70.
- [61] P. Suktha, N. Phattarasupakun, P. Dittanet, M. Sawangphruk, Charge storage mechanisms of electrospun  $\text{Mn}_3\text{O}_4$  nanofibres for high-performance supercapacitors, *RSC Adv.* 7 (2017) 9958–9963.
- [62] H. Shen, E. Liu, X. Xiang, Z. Huang, Y. Tian, Y. Wu, Z. Wu, H. Xie, A novel activated carbon for supercapacitors, *Mater. Res. Bull.* 47 (2012) 662–666.
- [63] S. Yu, Y. Li, N. Pan, KOH activated carbon/graphene nanosheets composites as high performance electrode materials in supercapacitors, *RSC Adv.* 4 (2014) 48758–48764.
- [64] K.H. An, W.S. Kim, Y.S. Park, J.M. Moon, D.J. Bae, S.C. Lim, Y.S. Lee, Y.H. Lee, Electrochemical properties of high-power supercapacitors using single-walled carbon nanotube electrodes, *Adv. Funct. Mater.* 11 (2001) 387–392.
- [65] Y. Liu, D. He, H. Wu, J. Duan, Graphene and nanostructured  $\text{Mn}_3\text{O}_4$  composites for supercapacitors, *Integr. Ferroelectr.* 144 (2013) 118–126.
- [66] Q. Cheng, J. Tang, J. Ma, H. Zhang, N. Shinya, L.C. Qin, Graphene and nanostructured  $\text{MnO}_2$  composite electrodes for supercapacitors, *Carbon* 49 (2011) 2917–2925.
- [67] K.-S. Kim, S.J. Park, Electrochemical performance of activated carbons/ $\text{Mn}_3\text{O}_4$ -carbon blacks for supercapacitor electrodes, *Bull. Korean. Chem. Soc.* 34 (2013) 2343–2347.
- [68] D.P. Dubal, G.S. Gund, R. Holze, C.D. Lokhande, Mild chemical strategy to grow micro-roses and micro-woolen like arranged CuO nanosheets for high performance supercapacitors, *J. Power Sources* 242 (2013) 687–698.
- [69] W. Yang, Z. Gao, J. Wang, B. Wang, Q. Liu, Z. Li, T. Mann, P. Yang, M. Zhang, L. Liu, Synthesis of reduced graphene nanosheet/urchin-like manganese dioxide composite and high performance as supercapacitor electrode, *Electrochim. Acta* 69 (2012) 112–119.
- [70] J. Wang, Z. Gao, Z. Li, B. Wang, Y. Yan, Q. Liu, T. Mann, M. Zhang, Z. Jiang, Green synthesis of graphene nanosheets/ $\text{ZnO}$  composites and electrochemical properties, *J. Solid State Chem.* 184 (2011) 1421–1427.

## CURRICULUM VITAE

Name: Amorntep montreeuppathum

Date of birth: 9 July 1993

Place of birth: Angthong, Thailand

Nationality: Thai

### Education

Academic year

2012 - 2015 Maejo University, Chiangmai, Thailand  
Bachelor of Science (Industrial Chemistry and Textile  
Technology)

2018 - present Suranaree University of Technology, Nakhon  
Ratchasima, Thailand.

Master of Science (Applied Physics)